THESIS

THE DEVELOPMENT AND VALIDATION OF AN X-BAND DUAL POLARIZATION DOPPLER WEATHER RADAR TEST NODE FOR A TROPICAL NETWORK

Submitted by

Miguel Bustamante Gálvez

Department of Electrical and Computer Engineering

In partial fulfillment of the requirements

For the degree of Master of Science

Colorado State University

Fort Collins, Colorado

Fall 2012

Master's Committee:

Advisor: V. Chandrasekar

V. N. Bringi

Paul W. Mielke

ABSTRACT

THE DEVELOPMENT AND VALIDATION OF AN X-BAND DUAL POLARIZATION DOPPLER WEATHER RADAR TEST NODE FOR A TROPICAL NETWORK

An automated network of three X-band dual polarization Doppler weather radars is in process of being deployed and operational on the western coast of Puerto Rico. Colorado State University and the University of Puerto Rico at Mayaguez have collaborated to install the first polarimetric weather radar network in a tropical environment, known as TropiNet, to observe the lowest 2 km of the troposphere where the National Weather Service NEXRAD radar in Cayey, PR (TJUA) has obstructed views of the west coast, below 1.5 km due to terrain blockage and the Earth curvature problem. The CSU-X25P radar test node was developed, validated, and deployed to Mayaguez, PR in early 2011 to make first observations of this tropical region, and served as a pilot project to verify the infrastructure of the TropiNet network.

This research describes the CSU-X25P radar test node, presenting the radar system specifications and an overview of the data acquisition and signal processing sub-systems, and the antenna positioner and control sub-system. The development and validation process included integration, sub-system calibration and test, and a final evaluation by conducting end-to-end calibration of the radar system. Validation of the calculated data moments, include Doppler velocity, reflectivity, differential reflectivity, differential propagation phase, and specific differential phase. The validation was accomplished by comparative analysis of data from coordinated scans between CSU-X25P and the well-established CSU-CHILL S-band polarimetric Doppler weather radar, in Greeley, CO.

Upon validation, CSU-X25P was disassembled, packaged, and shipped to Puerto Rico to be fully deployed for operation in a tropical seaside environment. This research presents select observations of severe weather events, such as tropical storms and hurricanes, which attest to the robustness of the radar test node, and the TropiNet network infrastructure.

ACKNOWLEDGMENTS

Firstly, I would like to thank God for giving me strength and patience during this process. I am grateful to my advisor Dr. V. Chandrasekar for presenting me with challenging, yet fulfilling projects that led to the work presented here. I would like to thank Dr. V.N. Bringi for serving on my committee, and for working with me on an undergraduate project which took me on my first of many trips to Puerto Rico. Without their support, guidance, and trust, none of this would be possible. A special thanks to Dr. Paul W. Mielke for serving on my committee.

I want to thank Dr. Francesc Junyent who shared his invaluable RF and Radar systems expertise. The staff at the CSU-CHILL Radar Facility were instrumental in facilitating the space for the assembly, testing, calibrating, and shipping of this radar. Many thanks to Dave Brunkow, Patrick Kennedy, Jim George, and especially Bob Bowie.

To the UPRM faculty, staff, and students who collaborated in the successful deployment of CSU-X25P to Puerto Rico, I owe a debt of gratitude. In particular, Dr. Jose G. Colom, Dr. Sandra Cruz-Pol, Dr. Rafael A. Rodriguez Solis, Don Carlos Mercado, Jose Rosario, Benjamin De Jesus, Jose Cordero, and Jose Kotshie Ortiz to name a few.

I would like to recognize Dr. Omnia El-Hakim who first believed that I could become a professor, and recommended me for the NSF-funded AMP Bridge to Doctorate Fellowship. I want to thank all my colleagues in the Radar Lab for their continued support over the years. Thank you Henry Obermeyer for donating engineering resources and materials to fabricate the transceiver mounting plate. To the girls I had the honor of coaching in soccer while working on my Masters, thanks for bringing me balance.

Lastly, *Mil Gracias* to my lovely wife Araceli, and my cousin Fernando Gálvez who kept me on track to finish this chapter of my life. It is done.

DEDICATION

To my wife Araceli, and my children Gemma del Rocio and Diego Miguel who were my support system throughout this process. You are the reason I do this. For the example of my father Miguel who was a man with the resolve and work ethic of ten. And for my mother Dora who selflessly sacrificed herself to always ensure that I could follow my dreams.

TABLE OF CONTENTS

1 Introduction **1**

2 System Description **4**

2.1 Overview 4

2.2 Transceiver 8

2.3 Data Acquisition System 10

2.4 Pedestal, Motors/Drives, and Control 11

2.5 Calibration 13

2.5.1 Transmitter Calibration 14

2.5.2 Receiver Calibration 15

2.5.3 Metallic Sphere Calibration 19

3 Signal Processing **23**

3.1 Overview 23

3.2 Digital I & Q Detection 24

3.3 Reflectivity (Z) 29

3.4 Doppler Velocity (v_d) 30

3.5 Differential Relectivity (Z_{dr}) 32

3.6 Differential Propagation Phase (ϕ_{DP}) and Specific Differential Phase (K_{DP}) 34

3.7 Clutter Suppression 35

4 System Validation with the CSU-CHILL Radar and Deployment on the Western Coast of Puerto Rico **37**

4.1 Description of Validation with CSU-CHILL Radar 37

4.2 Coordinated Observations 38
4.3 Selected Observations 41
4.4 Deployment of CSU-X25P Radar to the Western Coast of Puerto Rico . . . 45
4.5 First Observations in a Tropical Environment 51
4.5.1 Tropical Storm Emily 53
4.5.2 Hurricane Irene 55

5 Summary and Conclusions 67

References 69

A Antenna Positioner Assemblies 71

LIST OF TABLES

2.1 CSU-X25P Radar Specifications 6

2.2 CSU-X25P Transmitter Calibration Results 15

2.3 Metal sphere theoretical backscatter power calculation 20

LIST OF FIGURES

1.1 CSU-X25P radar node mounted atop R&D Center, UPRM campus 2

2.1 CSU-X25P validation at CSU-CHILL Radar Facility 4

2.2 CSU-X25P Radar System Block Diagram 5

2.3 CSU-X25P Transceiver Block Diagram 7

2.4 SCR-584 pedestal with EL motor and Transceiver mounting plate, shown without antenna and mounted on work stand 12

2.5 SCR-584 pedestal Azimuth motor mounted on adapter plate 13

2.6 SCR-584 Slip Ring Assembly 14

2.7 Gigabit Ethernet 15

2.8 Gigabit Ethernet rotary joint, mounting plate and conduit assembly 16

2.9 Transmit pulse time sample 17

2.10 Transmit pulse frequency spectrum 18

2.11 Receiver dynamic range at $f = 9.41GHz$ 19

2.12 Launching balloon and tethered metal sphere using electric winch 21

2.13 Balloon and metal sphere target down-range, 1 km from CSU-X25P 22

3.1 In-phase (I) and Quadrature phase (Q) components of the received signal. Note the Gaussian shape with zero mean. 26

3.2 Scatter plot of I & Q components of the received signal. Note that I & Q are uncorrelated. 27

3.3 Log histogram of (I^2+Q^2). The linear decrease indicates I^2+Q^2 is exponentially distributed. 28

3.4 CSU-X25P Z_{dr} Calibration 33

4.1 CSU-X25P vs. CHILL range profiles of 1° beamwidth. X25P centered at EL=2°, with starting height of 2 m. CHILL centered at EL=0.8° with starting height of about 10 m above ground level (AGL). 39

4.2 X25P ($EL = 2°$) and CHILL ($EL = 0.8°$) PPI scans on 2010-08-09 40

4.3 X25P Measured vs. DROPS-Corrected Z_h and Zdr Range Profiles 42

4.4 CSU-X25P Corrected Reflectivity vs. (a) CZdr and (b) K_{DP}. 43

4.5 CSU-X25P and CHILL RHI scans at AZ=217° on 2010-08-09 (UTC). Images created using CSU VCHILL. 44

4.6 Tropical rain event observed by X25P. RHI scan on June 8, 2011 06:25:37 (UTC), AZ= 288°. Images created using CSU VCHILL. 46

4.7 CSU-X25P 40 km range ring, centered at (18.2112, -67.1368). Image created using Google Earth and [1] 47

4.8 20 ft. Tower Structure atop R&D Building, UPRM campus 48

4.9 (a) 8 ft. antenna ready for shipment; (b) Loaded shipping container 49

4.10 Raising and mounting the pedestal, antenna, equipment onto building 50

4.11 UPRM graduate students: radar installation training 51

4.12 CSU-X25P Radar Control and Visualization Tools 52

4.13 Circulation off coast of Rincon, PR on 26 April 2011 18:42:45 UTC. Images created using CSU VCHILL and Google Earth 54

4.14 Waterspout off coast of Mayaguez, PR in September 2005 (photo courtesy of UPRM CLiMMATE Lab) 55

4.15 Tropical Storm Emily on 3 August 2011: (a) Infrared satellite storm track, and (b) TJUA reflectivity with relative storm tracking enabled (images created using Weather Underground's WunderMap web application) 56

4.16 CSU-X25P PPI images (15:21 UTC) of Tropical Storm Emily. Note storm approach from SE to NW due to CCW rotation of Emily from south. Images created using CSU VCHILL and Google Earth 57

4.17 Tropical Storm Emily, RHI scans through Inbound and Outbound rain band on 2011-08-03 at 15:57 UTC (a & c) and 15:28 UTC (b & d). For reference, cloud tops at 8-10 km; melting layer at 4.5-5 km. Images created using CSU VCHILL and Google Earth 58

4.18 Hurricane Irene storm track (using Weather Underground) 59

4.19 MODIS, TJUA, & CSU-X25P CdBZ & v_D PPI images of Hurricane Irene. Note shift from northeasterly to northwesterly direction in rain bands. MODIS image source: NASA/GSFC, MODIS Rapid Response. TJUA image source: Weather Underground. CSU-X25P images created with CSU VCHILL. 62

4.20 CSU-X25P CdBZ & v_D PPI images of Hurricane Irene (created with CSU VCHILL). Note shift from northwesterly to southwesterly direction in rain bands. 63

4.21 TJUA (dBZ) & CSU-X25P (CdBZ & v_D) images of Hurricane Irene. Note eye located NW of island, the southwesterly direction in rain bands and the significant increase in velocities to 18-25 m/s. TJUA image source: Weather Underground. CSU-X25P images created with CSU VCHILL 64

4.22 CSU-X25P CdBZ & v_D PPI images of Hurricane Irene (created with CSU VCHILL). Note the southwesterly to southerly shift in direction, and sustained velocities in the 18-22 m/s range. 65

4.23 CSU-X25P CdBZ & v_D PPI images of Hurricane Irene (created with CSU VCHILL). Note the southerly to southeasterly shift in direction, and sustained velocities in the 15-18 m/s range. 66

A.1 SCR-584 Pedestal Riser Dimensions 80

CHAPTER 1

Introduction

Meteorological radars have become an integral part of our lives with continuous demand from users for up-to-the-minute forecasts and severe weather warnings. The National Weather Service (NWS) has been providing the general public with periodic updates for many years via radio and television broadcasts, and now over the internet and even on portable devices, such as smart phones. There is an increasing demand for current, reliable, and higher resolution weather forecasts from NWS, which requires a complementary short-ranged, low-scanning, higher resolution, networked radar approach like that of CASA IP-1 [2, 3].

In 2006, the Collaborative Adaptive Sensing of the Atmosphere (CASA) Engineering Research Center deployed the first generation network of four low-power, short-range, X-band, polarimetric Doppler weather radars in Oklahoma's "tornado alley," near Norman, OK. CASA is a collaboration of several universities that includes Colorado State University (CSU), University of Massachusetts Amherst, University of Oklahoma, and University of Puerto Rico at Mayaguez (UPRM). It was soon apparent that such a networked strategy could improve observations in tropical environments, where a single high-powered, long-range NEXRAD radar had obstructed views of the lowest 2 km of the troposphere. A major advantage of going to an operating frequency in the X-band is the radar nodes are a much smaller and more cost-effective solution relative to the currently employed NEXRAD WSR-88D radars, operating at S-band. This prompted UPRM and CSU to begin investigating the feasibility of deploying a network of dual-polarized X-band Doppler weather radars in the tropical environment of Puerto Rico.

An automated network of three X-band polarimetric Doppler weather radars (TropiNET) is in process of being deployed on the western coast of Puerto Rico, as proposed in [4]. UPRM and CSU have collaborated to identify potential site locations and prepared the infrastructure for this network. Prior to the development of the TropiNET radar network, a single X-band

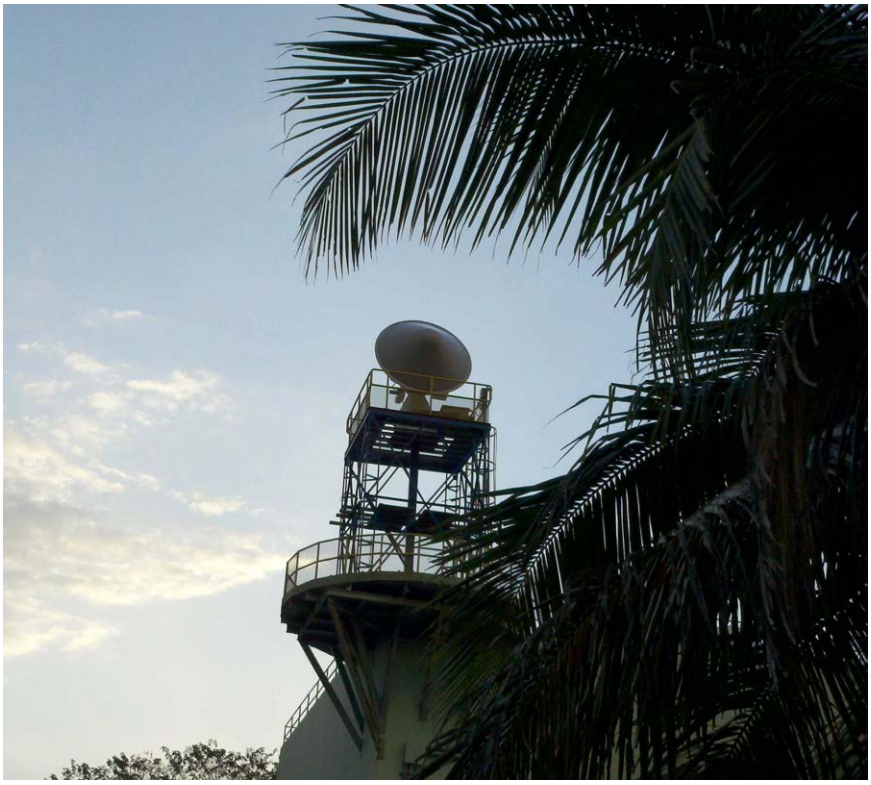

Figure 1.1: CSU-X25P radar node mounted atop R&D Center, UPRM campus

polarimetric Doppler weather radar, CSU-X25P was deployed in January 2011 to make observations in the tropical environment around Mayaguez, Puerto Rico as a pilot project. This radar is mounted on a tower atop the R&D Center building on the UPRM campus, in Figure 1.1, and is maintained and operated locally and remotely by staff from both UPRM and CSU. The CSU-X25P radar node is the first dual polarization Doppler weather radar to be deployed in Puerto Rico, and made first observations of the lower troposphere of the islands west coast, where the region has a lack of coverage at low altitudes by the WSR-88D radar (TJUA) in Cayey, PR, due to the Earth's curvature and terrain blockage.

The CSU-X25P radar node description, development, validation, and select first observations by a polarimetric X-band Doppler weather Radar of the western coast of Puerto Rico will be presented herein. This Thesis will provide detail of the system presented here in the following chapters.

Chapter 2 will present a detailed system description of the CSU-X25P radar node. Details

of the transceiver analog hardware are given, including system specifications, RF section, and system level block diagrams. An overview of the data acquisition system gives background information on the analog-to-digital conversion of the intermediate frequency, to later be digitally down converted to provide the in-phase and quadrature-phase components. Another section will present the pedestal, motors, and antenna control. Finally, calibration results of the transmitter and receiver are given.

Chapter 3 discusses signal processing of the digital I&Q complex components used to calculate the data moments. It is from these moments that reflectivity, Doppler velocity, differential reflectivity, differential propagation phase, and specific differential phase are obtained. Rain rates and clutter suppression algorithms are also presented. Significant statistical requirements of the I&Q data, to ensure estimation errors are minimized, are discussed and validation with actual data are presented.

Chapter 4 presents weather events used to validate the system with the CSU-CHILL Radar in Greeley, CO. A brief discussion will explain how the data is presented and how the radar meteorologist interprets it. This chapter will also show select observations of tropical rain events during deployment of the CSU-X25P on the western coast of Puerto Rico.

Chapter 5 will be a summary and conclusion of this Thesis. A further discussion of lessons learned from this deployment, and how they can be applied to ensure the success of the TropiNet network will be presented.

CHAPTER 2

System Description

2.1 Overview

The CSU-X25P radar was built at the CSU-CHILL Radar facility in Greeley, CO where it was tested and validated in 2010 (Figure 2.1). The radar is composed of a transceiver, data acquisition unit (DAQ), signal processor, antenna, antenna positioner, and associated computers and disk space for control, data storage and processing. Figure 2.2 shows the major components of the CSU-X25P Radar system.

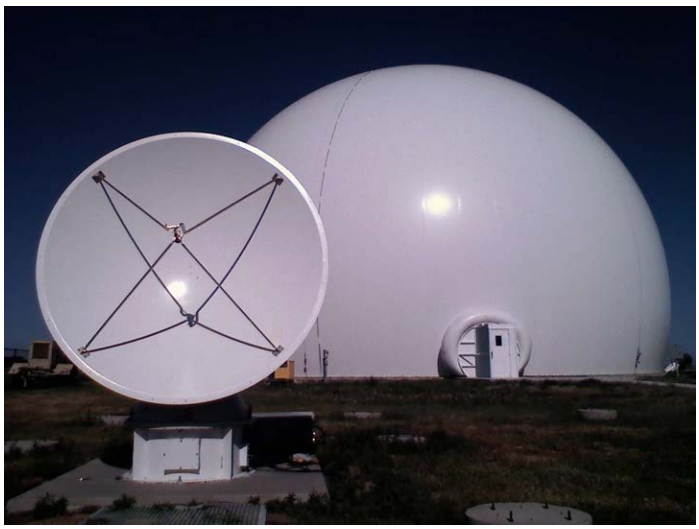

Figure 2.1: CSU-X25P validation at CSU-CHILL Radar Facility

The magnetron-based transmitter, operating in the 9.41 GHz ± 30 MHz frequency range, with a maximum 25 kW peak output power, is jointly housed, in an enclosure, with the receiver, eDAQ, and processor near the antenna, above the azimuth axis of rotation. In order to accommodate the higher dual PRF bursts of pulses needed for high Doppler velocity resolution and clutter filtering, the transmitter was tuned below its maximum peak power

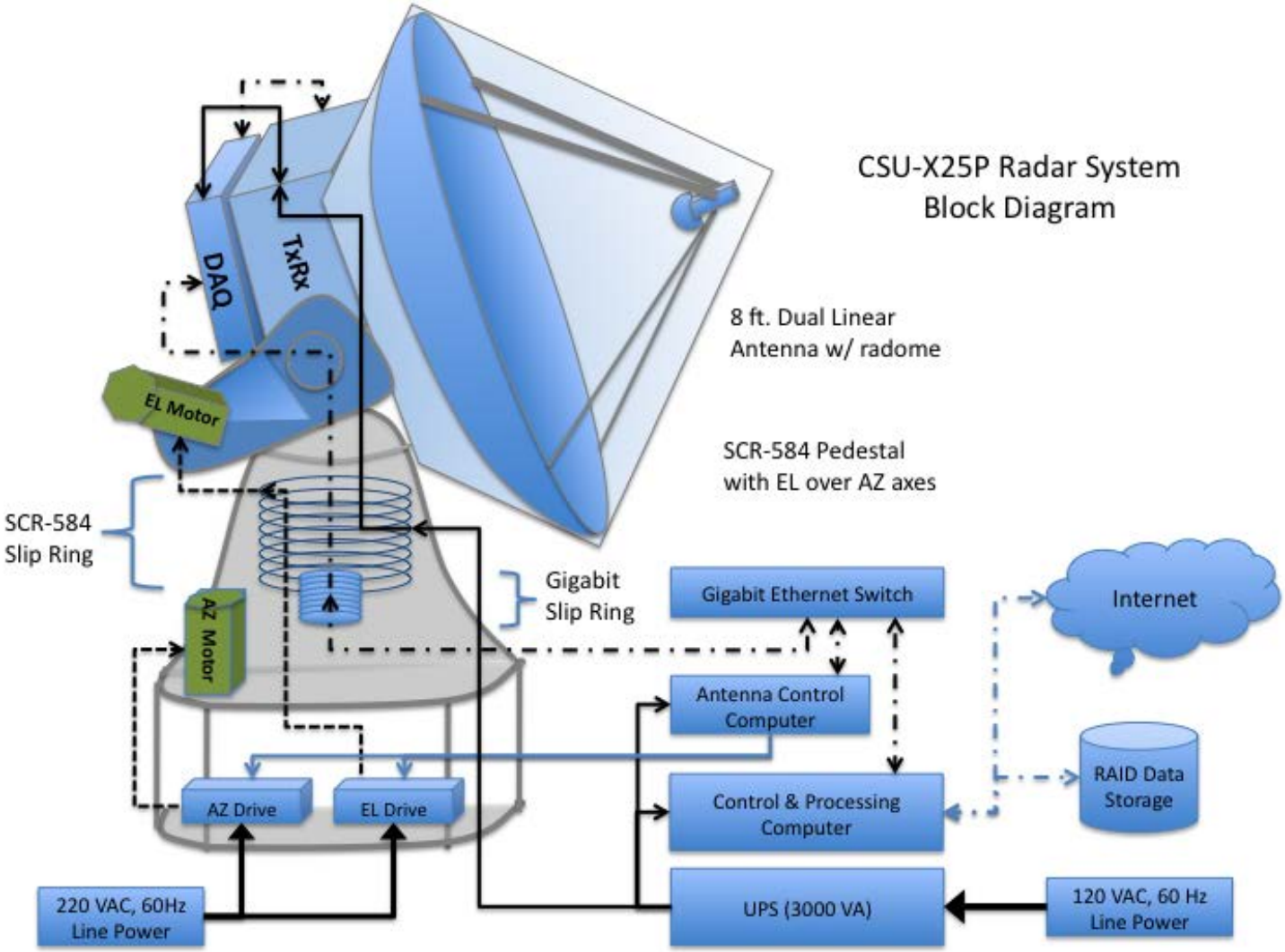

Figure 2.2: CSU-X25P Radar System Block Diagram

allowing for increased duty cycle. All radar signals and control commands between the transceiver and the signal processor are made via a Gigabit Ethernet rotary joint installed through the azimuth axis [5].

The center-fed, dual linearly polarized parabolic antenna provides a minimum gain of 44 dB with a beamwidth of 1.03 degrees (in azimuth and elevation) for both channels. The antenna comes equipped with an antenna-mounted radome to help protect it from the environment. Arbitrary scanning patterns are achieved by 360 degrees of rotation in azimuth, and up to 90 degrees in elevation by the antenna positioner. The radar specifications are listed in Table 2.1.

Table 2.1: CSU-X25P Radar Specifications

TRANSMITTER	
Type	Magnetron
Center Frequency	9410 ± 30 MHz
Peak Power output	8.0 kW (per channel)
Average Power output	12 W (per channel)
Pulse Width	660-1000 ns
Polarization	Dual linear, H and V
Max. Duty Cycle	0.16%
ANTENNA AND PEDESTAL	
Type (diameter)	Dual-polarized parabolic reflector (2.4m)
3-dB Beam width	1.03°
Gain	44 dB
Maximum Scan Rate	30°/ s
RECEIVER	
Type	Parallel, dual channel, linear output I/Q
Dynamic Range	103 dB (BW = 1.5 MHz)
Noise Figure	5.5 dB
DATA ACQUISITION SYSTEM	
Sampling Rate	100 Msps
Dynamic Range	113 dB (BW= 500 kHz)

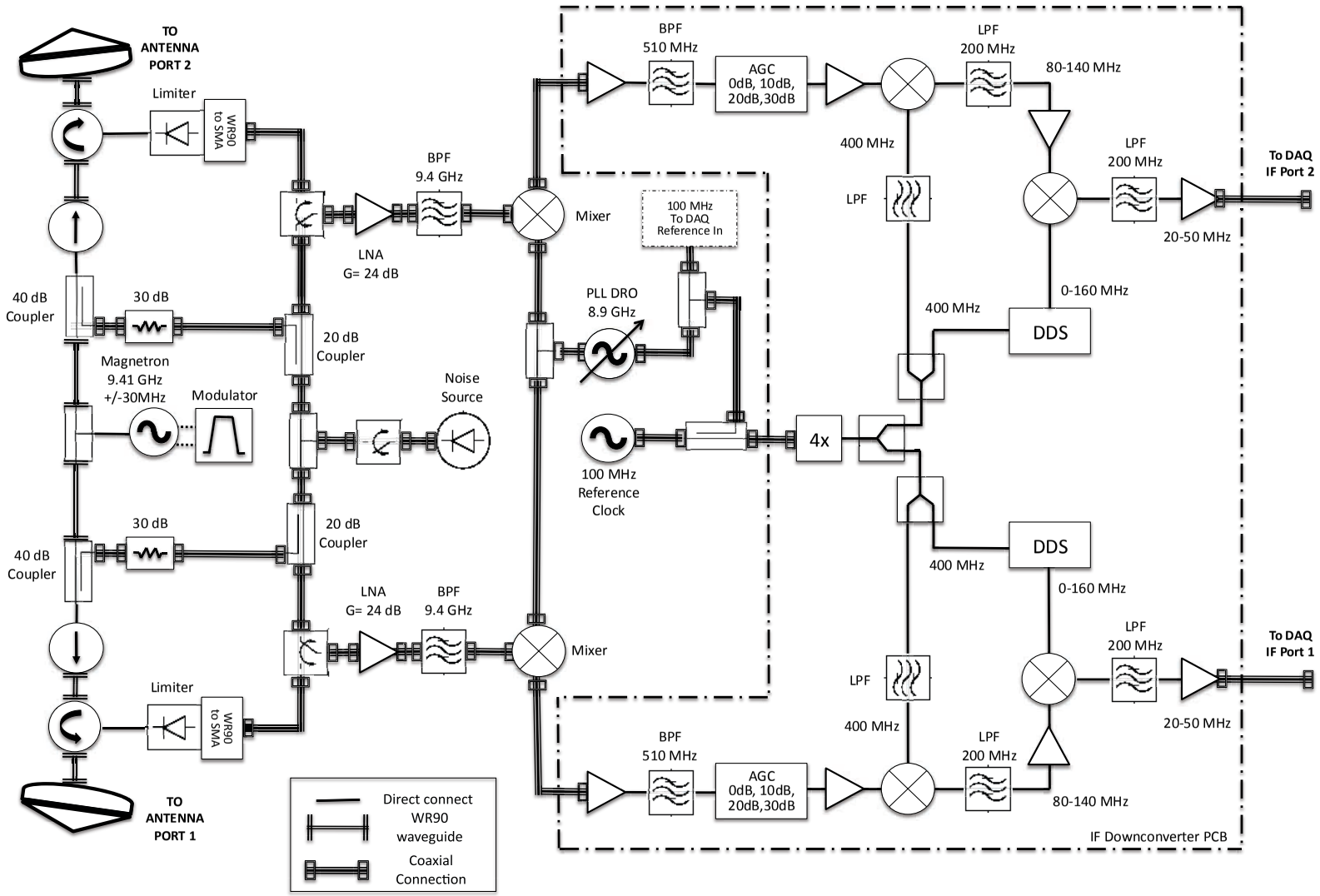

Figure 2.3: CSU-X25P Transceiver Block Diagram

2.2 Transceiver

At the heart of the radar is the transceiver which is composed of a high power transmitter, a duplexer, and a receiver as seen in the block diagram of Figure 2.3. It is here that a sub-microsecond pulse is generated by the Raytheon Mark 2 high power modulator board and transmitted by a magnetron with up to 25 kW (25 W average) output power, and an operating center frequency of 9.41 GHz. The transmitter output power level is reduced by 2 dB, from it's default maximum of 74 dB at 1 μs pulse width, to a maximum pulse length of 660 ns which allows for an increased duty cycle. Higher pulse repetition frequencies (PRF) result in transmitter waveforms that set the ability of the system to unambiguously resolve higher Doppler velocities, suppress second trip echoes, and filter unwanted ground clutter. Doppler velocity for a uniform PRF pulsed radar is found as,

$$v_{max} = \pm \frac{\lambda PRF}{4}, \tag{2.1}$$

and in the case for a wavelength (λ) of 3 cm, at 1 kHz PRF, the maximum unambiguous Doppler velocity is $\pm$ 7.5 m/s. The transmitter waveform is modified to allow blocks of pulses at two higher PRFs, like 2.4 kHz and 1.6 kHz, thereby extending the achievable unambiguous Doppler velocity. Most meteorologically significant phenomena occur with velocities above the $\pm$ 20 m/s interval, therefore operating in a dual PRF mode allows the unambiguous Doppler velocity to be resolved to the interval $\pm$ 38 m/s. The maximum unambiguous velocity, v_{max}, for this scheme can be found as,

$$v_{max} = \pm \frac{\lambda}{4(PRF_2^{-1} - PRF_1^{-1})}. \tag{2.2}$$

The duplexer, constructed of WR90 waveguide components, equally divides the power from the magnetron into two RF channels that connect to the Horizontal and Vertical ports of the center-fed parabolic antenna. The duplexer also provides protection to the magnetron against damaging reflections from each channel, with an isolator and circulator in the path to the antenna ports. The duplexer includes, per channel, a 40 dB coupler that provides

dedicated sample paths of the transmit pulse (via an additional 30 dB pad and 20 dB coupler) which is used to estimate the transmitted frequency, amplitude, and starting phase. The duplexer also directs the received echoes from the antenna to the receiver front end, while also providing protection to the Low Noise Amplifiers (LNAs) via limiters.

The dual-channel receiver front end is composed of connectorized components, followed by a mixed signal IF-PC board that together down-convert the RF signal to a final analog intermediate frequency (IF). The receiver has three analog down-conversion stages, the first IF at 510 MHz is accomplished by mixing the received echo with a disciplined local oscillator (PLL DRO) at 8.9 GHz. The first IF is then mixed with the IFPCB 400 MHz LO, to obtain the second IF at 110 MHz. The final analog IF is obtained by down-converting the second IF with the output from a programmable Direct Digital Synthesizer (DDS) to yield an IF in the 9.75-21.25 MHz band, to then be sampled and digitized by the data acquisition system A/D converters. The digital receiver in the data acquisition unit (eDAQ) will down-convert this digitized signal to baseband by setting the numerically controlled oscillator (NCO) to the appropriate frequency. At baseband we are only left with the weather echo return, which can then be further processed to remove ground clutter and estimate meteorological moments for radial velocity (v_d), reflectivity (Z), differential reflectivity(Z_{dr}), differential propagation phase (ϕ_{dp}), and specific differential phase (K_{DP}). These products will be discussed in more detail in Chapter 3.

The DDS output frequency is set by a software-controlled Automatic Frequency Control (AFC) loop in the eDAQ, determining the analog receiver's final down-conversion frequency by tracking the transmitted frequency. The naturally occurring random phase of the magnetron can also be estimated, and the DDS allows for the setting of any arbitrary phase difference between the two receive channels. This can be used to mitigate second-trip echoes. The analog receiver also includes a four level phase matched fast-switching Automatic Gain Control (AGC) which allows extension of the dynamic range, thus preventing saturation of the LNAs in strong clutter environments.

2.3 Data Acquisition System

The data acquisition system of the CSU-X25P is based on the proven FPGA-based board set from Dynamic Sensing Technologies (eDAQ), designed for networked weather radar nodes [6]. The dual-channel eDAQ serves to digitize the intermediate frequency, is a digital receiver, AFC and AGC controller, real time data manager, and is also responsible for generating the triggering scheme for the transmitter. At the eDAQ front end, the two impedance matched channels include programmable gain of the H and V signals prior to each being digitized by 14-bit ADCs, at a 100 MHz sampling frequency. The sampled data signal is processed in real-time and a digital I & Q (in-phase and quadrature) detection is implemented, along with band limiting and decimation to achieve the final bandwidth. As previously mentioned, a numerically controlled oscillator (NCO), with a better than 150 dB spurious-free dynamic range (SFDR), is digitally implemented in the processor core, within the FPGA, to down-convert the incoming IF to baseband. The NCO frequency is selected based on the magnetron frequency estimate obtained from samples of the transmit pulse, collected at the beginning of each data ray. The estimated magnetron frequency is used to set the DDS output in the range of 75 MHz to 125 MHz, at steps of 12.5 MHz, to keep the incoming analog IF near 10 MHz thus ensuring sampling above Nyquist and allowing the NCO to effectively digitally down-convert to baseband.

The digital AFC loop monitors the sampled transmit frequency to guarantee the received signal is in band and not affected by frequency shifts of the magnetron output due to thermal variations and/or instantaneous changes in duty cycle, resulting from dual PRF operation. The eDAQ board also performs the critical function of making this a coherent-on-receive radar by subtracting the estimated transmit pulse phase from the received echoes. Finally, User Datagram Protocol or UDP-formatted data packages containing the filtered, decimated, coherent, baseband I & Q samples are streamed in real time over a gigabit link to a post-processing computer on the local network. UDP is a protocol used to transport data across an IP based network, and skips handshaking, which makes it faster than most other protocols during data transmission.

2.4 Pedestal, Motors/Drives, and Control

In selecting the antenna positioner for the CSU-X25P, the key requirements were that it must achieve 360 ° azimuthal (AZ) rotation at a minimum of 30 °/ s and 90 ° tilt in the elevation (EL) axis. Aside from meeting these requirements, the SCR-584 pedestal was selected because of its robust design, ability to operate in most adverse environments, and its modest cost and availability. The Signal Corps Radio (SCR) ♯584 was an S-band radar (operating frequency ≈ 3000 MHz) developed by the Radiation Laboratory at MIT during World War II [7]. These pedestals are sought after by many researchers designing both mobile and stationary weather radar systems for their proven deployability in the harshest of environments.

To improve the rotational resolution of the SCR-584, the original motors were replaced by two high power rotary brushless servo motors, for high inertia (Parker-Hannifin model MPJ0922D41KPSV), as seen in Figures 2.4 and 2.5. The servo motors are driven by Advanced Motion Controls digital servo drives (model DPRANIR03A400, for data sheet see http://www.a-m-c.com/products/dpr.html), which can be controlled using AMC DriveWare or custom position control software, via standard RS-485/232 communication protocol. AMC DriveWare is used to initialize the drives with current-loop, acceleration, and digital I/O configurations for proper operation of the motors. A custom position control moment daemon, residing on the antenna control computer is used to specify start/stop angles, scan speeds, incremental steps, and select axis of motion to achieve volume coverage patterns (VCP) for weather feature identification.

SICK-Stegmann ARS-25 SSI encoders were used as replacements to the original SCR-584 synchros, to provide feedback of the angular position of both azimuth and elevation axes. The servo drives selected did not include incremental encoder inputs, and therefore a custom circuit board (Appendix A) was designed by a CHILL staff member to interpret the encoder input before interfacing to the antenna control computer via an RS-485 port. It is important to note that the servo amp power wires, for Motor A, B, and C, must be wrapped through toroid ferrites (see Advanced Motion Controls Ferrite Recommendations, under

Figure 2.4: SCR-584 pedestal with EL motor and Transceiver mounting plate, shown without antenna and mounted on work stand

'Downloads & Support,' at http://www.a-m-c.com/products/dpr.html), near the source, in order to eliminate transient electromagnetic interference onto adjacent encoder, gigabit ethernet, and other control signals. Not doing so results in intermittent and/or incorrect I & Q data packet and antenna position transmissions. This was one of the key problems solved in the development stage of this radar.

Adapter plates (Figure 2.5), machined from aluminum stock, were necessary to mate both Parker motors to the original motor mounting holes, while the motor shaft was lengthened to allow proper engagement of the planetary gears. The incremental encoders also required custom machined adapter plates for mounting into the original synchro mounts, and proper engagement of position feedback gears in the elevation and azimuth axes. It was necessary to modify the slip-ring wiring (Figure 2.6) and the terminal blocks above and below the axis of rotation, to separate the elevation axis motor power wiring from the EL encoder wiring. The pedestal was acquired as a refurbished unit and based on two units received, both arrived

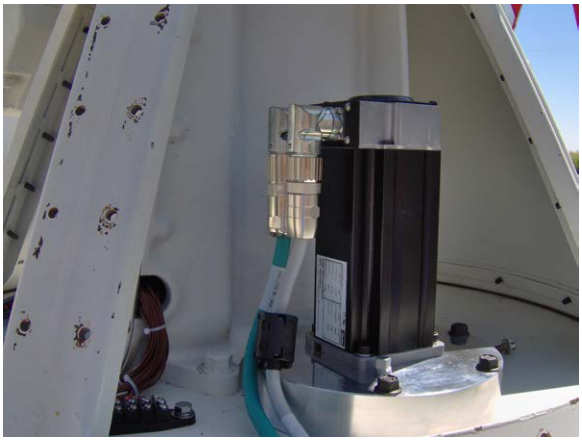

Figure 2.5: SCR-584 pedestal Azimuth motor mounted on adapter plate

with unique wiring order through the slip-ring.

A gigabit ethernet rotary joint assembly (MOOG Inc.) was installed to enable real-time high speed transfer of the I&Q data from the eDAQ (mounted behind the antenna, above the azimuth axis) to the remotely located signal processing computer. The rotary joint passes through the SCR-584 pedestal's slip-ring center shaft via the azimuthal axis into the elevation terminal block wiring chamber, seen in Figure 2.7. This center shaft was originally designed to pass waveguide from the pedestal base up to the antenna via waveguide rotary joints in the azimuth and elevation axes. A custom mounting plate and conduit assembly were fabricated, as seen in Figure 2.8. The Ethernet slip-ring must be mounted from underneath the pedestal, and thus required it be mounted onto a stand that allowed easy access during the assembly stages.

2.5 Calibration

Prior to collecting meteorological data with the CSU-X25P, it was necessary to obtain different measurements to characterize the transmitter, receiver gain and dynamic range, followed by a metallic sphere calibration. These tests were conducted at the CSU-CHILL Radar Facility.

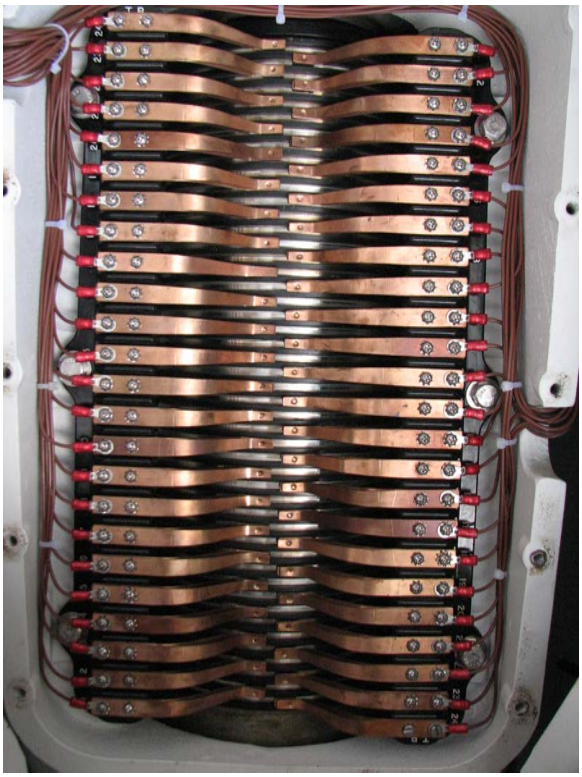

Figure 2.6: SCR-584 Slip Ring Assembly

2.5.1 Transmitter Calibration

The transmitter pulse peak power was measured for both horizontal (H) and vertical (V) ports using a power meter connected to the respective duplexer antenna port through a 40 dB coupler plus an additional 30 dB attenuator to prevent damage to the power sensor head. Because the transmit pulse power out of the magnetron is expected to be around 72 dBm, a high power dummy load was connected in series to the 40 dB coupler's through port. The measured H-polarization signal was found to be $P_{T_H} = 68.1$ dBm, whereas the corresponding value of the V-polarization signal was $P_{T_V} = 68.7$ dBm. To validate the measured values at the antenna ports, the duplexer losses are added to these values to obtain the magnetron output power, which was found to be as expected for both channels. The coupler, duplexer, and all other RF paths were characterized prior to final assembly. The transmitter results are summarized in Table 2.2.

A sample of the transmit pulse is recorded by the eDAQ, via the Tx sample path (40 dB

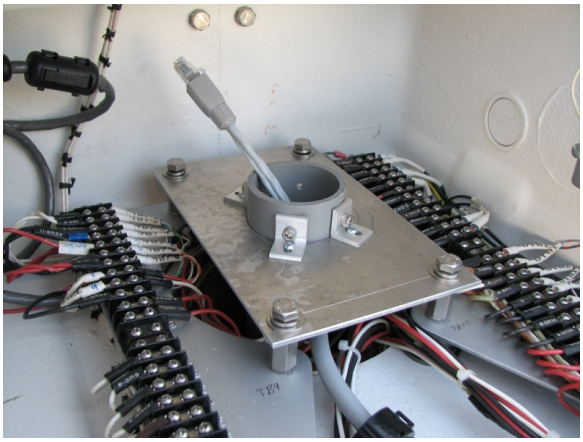

Figure 2.7: Gigabit Ethernet RJ-45 cable end via shaft in EL wiring chamber.

Table 2.2: CSU-X25P Transmitter Calibration Results

Channel	Power meter measurement	Attenuator and Coupler Loss	Transmitted Power	Duplexer Loss	Magnetron Power
Horizontal	-2.0 dBm	70.2 dB	68.2 dBm	4.0 dB	72.2 dB
Vertical	-1.1 dBm	69.7dB	68.6 dBm	4.0 dB	72.6 dB

coupler, 30dB attenuator, 20dB coupler, and high speed RF switch) into the LNA to verify its temporal and spectral characteristics. This sample is taken on a pulse-to-pulse basis, by controlling the high speed switch between the transmit and receive paths, then the signal proceeds to the downconversion stages. The transmit pulse was found to have a duration of $\tau = 450ns$ (Figure 2.9), and a corresponding transmit frequency spectrum with a 3 dB bandwidth of $B_{Tx} = 2.01MHz$, as seen in Figure 2.10.

2.5.2 Receiver Calibration

The gain and dynamic range of the CSU-X25P receiver were established using an external signal source connected at the receiver H and V antenna ports. A sinusoidal signal, set at the operating center frequency $f = 9.41GHz$, is swept in power from the receiver's noise floor to saturation, while the digital receiver's measured output power is recorded. Figure 2.11 shows the results. The dynamic range is obtained by determining the difference in power levels corresponding to the 1 dB compression point and noise floor. The RF-to-IF gain is

Figure 2.8: Gigabit Ethernet rotary joint, mounting plate and conduit assembly

established by subtracting the input and output power levels in the linear region.

The receiver bandwidth was established by injecting a sinusoidal signal of known frequency, $f = 9.41GHz$, into the receiver antenna ports. The receiver downconversion frequency was then swept, while the variation in power at the digital receiver output was recorded. This resulted in a 3 dB receiver bandwidth of $B_{3dB} = 1.01MHz$, in good agreement with expected theoretical values.

The previous measurements indicate a mismatch between the transmitted pulse bandwidth ($B_{Tx} = 2.01MHz$) and the receiver bandwidth ($B_{3dB} = 1.01MHz$), resulting in signal power loss due to the receiver finite bandwidth. To investigate this power loss, the following procedure was followed: the measured receiver transfer function was used to filter the transmitted pulse spectrum, and the signal power difference between the filter input and output yielded a signal loss $L_r = 3.7dB$.

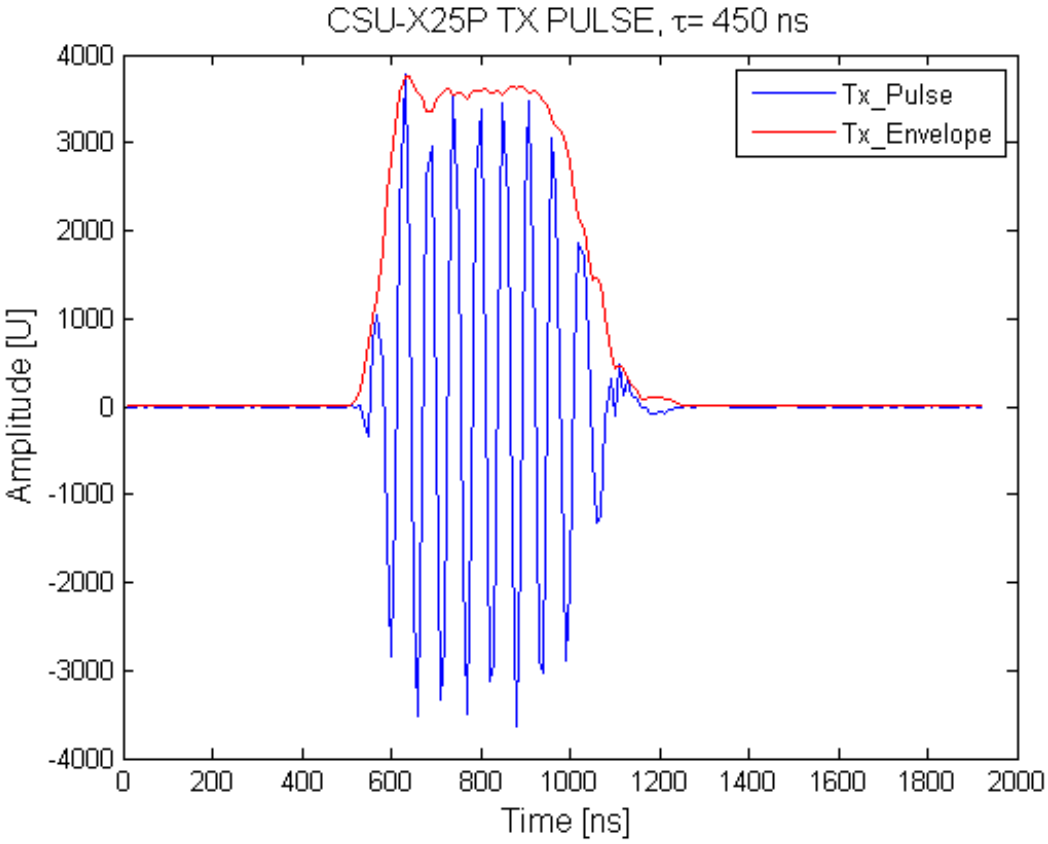

Figure 2.9: Transmit pulse time sample

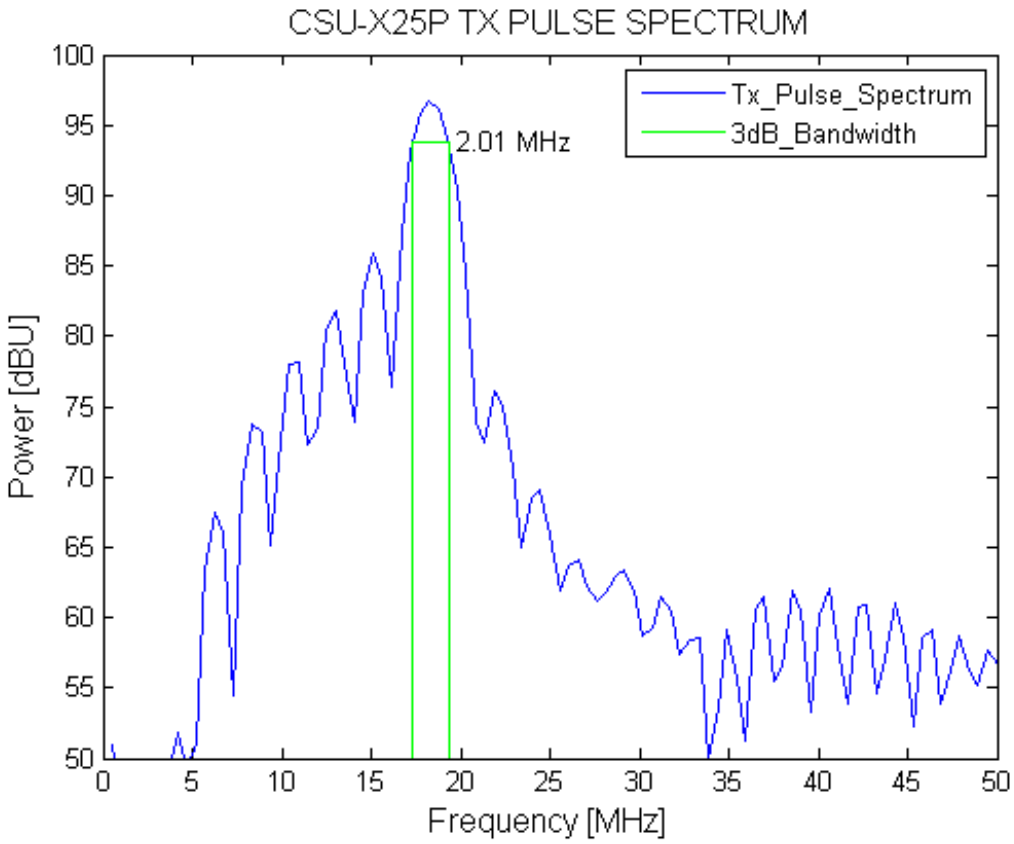

Figure 2.10: Transmit pulse frequency spectrum

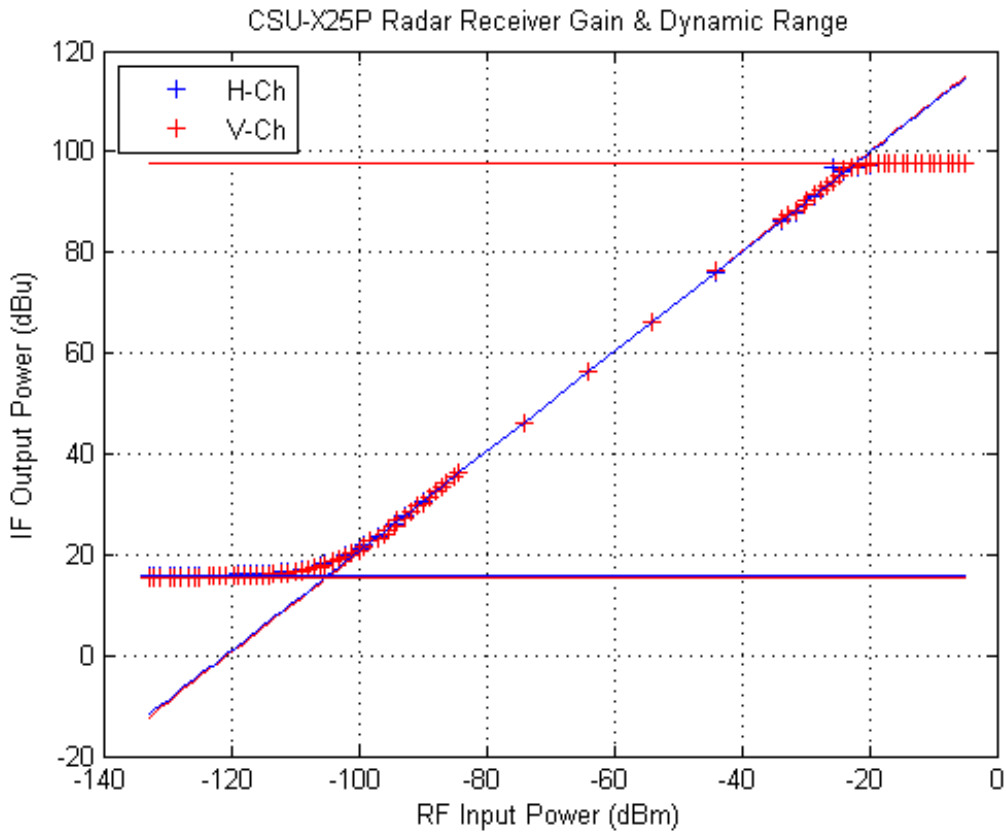

Figure 2.11: Receiver dynamic range at $f = 9.41GHz$

2.5.3 Metallic Sphere Calibration

A sphere calibration provides an end to end calibration of the radar system. This involves tethering, or free-flying, a metal sphere of known radius, to a 300 gram weather balloon, and use it as a target in the antenna far field. Figure 2.12 shows the battery-powered winch that was used to hold the balloon at a relatively fixed height of about 500 ft. above the ground. Figure 2.13 shows the balloon and metal sphere at approximately 1 km away from the CSU-X25P. Time series data was collected while scanning around the target and was used to obtain the backscattered signal power. The measured power was then compared to the expected theoretical power. The expected theoretical power at the digital receiver

output is obtained by the following:

$$P_r = P_t + 2G_a + 10log\left[\frac{\pi a^2 \lambda^2}{(4\pi)^3 r^4}\right] - L_r + G_{dBm2dBu} \tag{2.3}$$

where P_t is the transmitted power in dBm, G_a is the antenna gain in dB, a is the radius of the metal sphere in m, λ is the radar wavelength, r is the radial target range from the radar, L_r is the radar receiver finite bandwidth loss, and $G_{dBm2dBu}$ is the radar receiver analog plus digital gain. Table 2.3 summarizes the parameters used and the obtained results.

Table 2.3: Metal sphere theoretical backscatter power calculation

$P_r[dBu]$	$P_t[dBm]$	$G_a[dB]$	$a[in]$	$\lambda[m]$	$r[m]$	$L_r[dB]$	$G_{dBm2dBu}$
78.1	68	44	5	0.03	1020	3.7	122

The time series data collected during the experiment was processed to first obtain the target returns as the radar scanned in azimuth. Once a return signal was identified, a gaussian fit (corresponding to the two-way antenna pattern azimuth) was used to determine its power and position in azimuth. This was repeated for the adjacent range gates to obtain a gaussian fit in range. The maximum values were selected from the gaussian fit in range at multiple elevations to obtain a final gaussian fit in elevation from which to obtain the measured metal sphere target backscatter.

Figure 2.12: Launching balloon and tethered metal sphere using electric winch

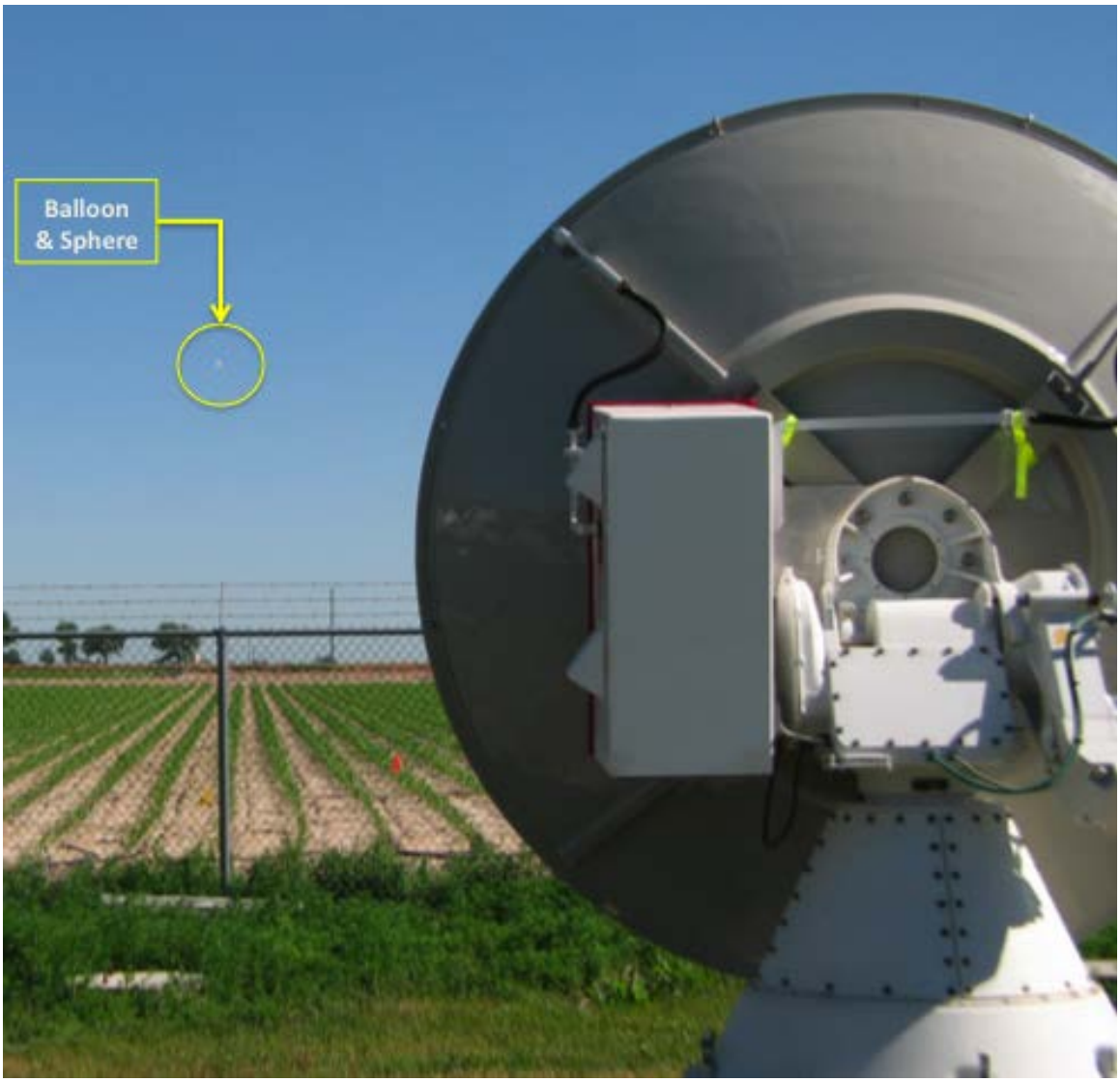

Figure 2.13: Balloon and metal sphere target down-range, 1 km from CSU-X25P

CHAPTER 3

Signal Processing

3.1 Overview

After the correct analog and digital downconversion stages of the IF signal are achieved, the decimated and band limited received echo signal is phase corrected relative to the transmit pulse phase. This is a standard coherent-on-receive technique used to obtain the wanted echo signal information, such as phase of the scattered wave, the complex signal amplitude, and Doppler shift relative to the radar. The received signal due to a single scatterer is a scaled replica of the transmitted waveform, $U_{tr}(t)$ shifted in time by its delay in range ($\tau_s = 2r/c$) and in frequency by the Doppler shift ($f_D = -2v/\lambda$). At the antenna port, the received voltage (i.e. complex envelope of received signal) for a spherical particle can be expressed as [8],

$$V_r(t) = \frac{\lambda G\sqrt{P_t}}{4\pi r^2}(S)e^{-j2k_0 r}U_{tr}(t-\tau_s). \tag{3.1}$$

where S is the scattering matrix of the particle, P_t is the transmitted power, G is the antenna gain, r is the particle's range, and the wave number $k_0 = 2\pi/\lambda = 2\pi f_0/c$.

In the case of scattering from precipitation, large numbers of hydrometeors will occupy a resolution volume defined by the range gate at $r+\Delta r_{min}$, and the minimum 3dB beamwidths of the antenna, in azimuth and elevation (ϕ_{3dB} and θ_{3dB}). The hydrometeors can extend over a large range with varying scattering amplitudes and moving at different velocities, where the received voltage is the resultant of contributions from the scatterers. The received voltage $V_r(t)$, at a particular range (r=$c\tau_s/2$), can be expressed as a discrete sum from the individual contributions in the resolution volume as,

$$V_r(t) = \sum_k A_k(\tau_k;t)e^{-j2f_0\tau_k}U_{tr}(t-\tau_k). \tag{3.2}$$

where A_k is the scattering amplitude of the kth hydrometeor. For a given t the receive voltage can be represented as the sum of these elemental phasors, and when considering $V_r(t + \Delta t)$, the particles are time-varying. This movement causes change in their location r_k and phase $\theta_k = (4\pi/\lambda)r_k$, where $-\pi \leq \theta_k \leq \pi$, and by estimating the received power and phase shift relative to the transmit pulse the various moments necessary for meteorological analysis are obtained. These moments are calculated from the I&Q components of the complex envelope, to include the effective reflectivity (Z) and Doppler velocity (v_d in m/s), differential reflectivity (Z_{dr}), differential propagation phase (ϕ_{DP}), and specific differential phase (K_{DP}).

Due to its transmitter configuration, the CSU-X25P radar test node only operates with simultaneous transmission of horizontal and vertical polarization states, but in addition to copolar return power, each receiver antenna port experiences cross-coupling from the other polarization (i.e., cross-polar power). This mode of operation is know as the "hybrid mode," and experiences perturbations in the retrieved copolar radar parameters previously mentioned. Care was taken to mitigate radar parameter biases, by limiting and addressing system polarization errors, like those due to antenna properties and orientation of hydrometeors, as presented in [9], [10], and [11]. The calculation of data products throughout this paper are made under the general assumption of a hybrid mode of operation.

3.2 Digital I & Q Detection

Digital detection of the in-phase and quadrature (I&Q) components of the sampled receiver echoes is the most important step in radar signal processing in order to calculate the Doppler spectral moments. At the output of the analog receiver, the radar signal can be represented by amplitude and phase modulation as follows,

$$x(t) = a(t)\cos(2\pi f_0 t + \theta(t)) \tag{3.3}$$

$$= a(t)\cos\theta(t)\cos 2\pi f_0 t - a(t)\sin\theta(t)\sin 2\pi f_0 t \tag{3.4}$$

$$= I(t)\cos 2\pi f_0 t - Q(t)\sin 2\pi f_0 t \tag{3.5}$$

where f_0 is the carrier frequency, θ is the phase modulation, and $a(t)$ is the amplitude modulation. The I&Q components are extracted from the complex signal $s(t)$ after downconversion to baseband, and as seen below, are the orthogonal basis components of the receiver voltage $V_r(t)$ as,

$$\begin{aligned} s(t) &= V_r(t)e^{j2\pi f_0 t} && (3.6)\\ &= a(t)e^{j\theta(t)}e^{j2\pi f_0 t} && (3.7)\\ &= [I(t) + jQ(t)]e^{j2\pi f_0 t} && (3.8) \end{aligned}$$

The CSU-X25P digital receiver converts the analog IF complex signal into a discrete sampled version which will finally be digitally downconverted to baseband with a numerically controlled oscillator (NCO). The discretized baseband complex signal is,

$$\begin{aligned} V_r[n] = s[n] &= I[n] + jQ[n] && (3.9)\\ &= a[n]e^{j\theta[n]} && (3.10) \end{aligned}$$

The received power is obtained from the complex signal as,

$$\begin{aligned} P_r[n] = V_r[n]V_r^*[n] &= |V_r[n]|^2 && (3.11)\\ &= I^2[n] + Q^2[n] && (3.12) \end{aligned}$$

and is typically represented as the mean power $\overline{P_r}[k]$ of N randomly distributed samples with random scattering amplitudes, at a particular range in the k-th range gate. For this random process, the mean power is simply the variance of $V_r(t)$.

The real and imaginary components, I and Q, carry information about the stochastic signal and have to satisfy the following properties as presented in [8]:

1. The I & Q components for the same time, are uncorrelated

$$cov\big[I(t), Q(t)\big] = 0 \qquad (3.13)$$

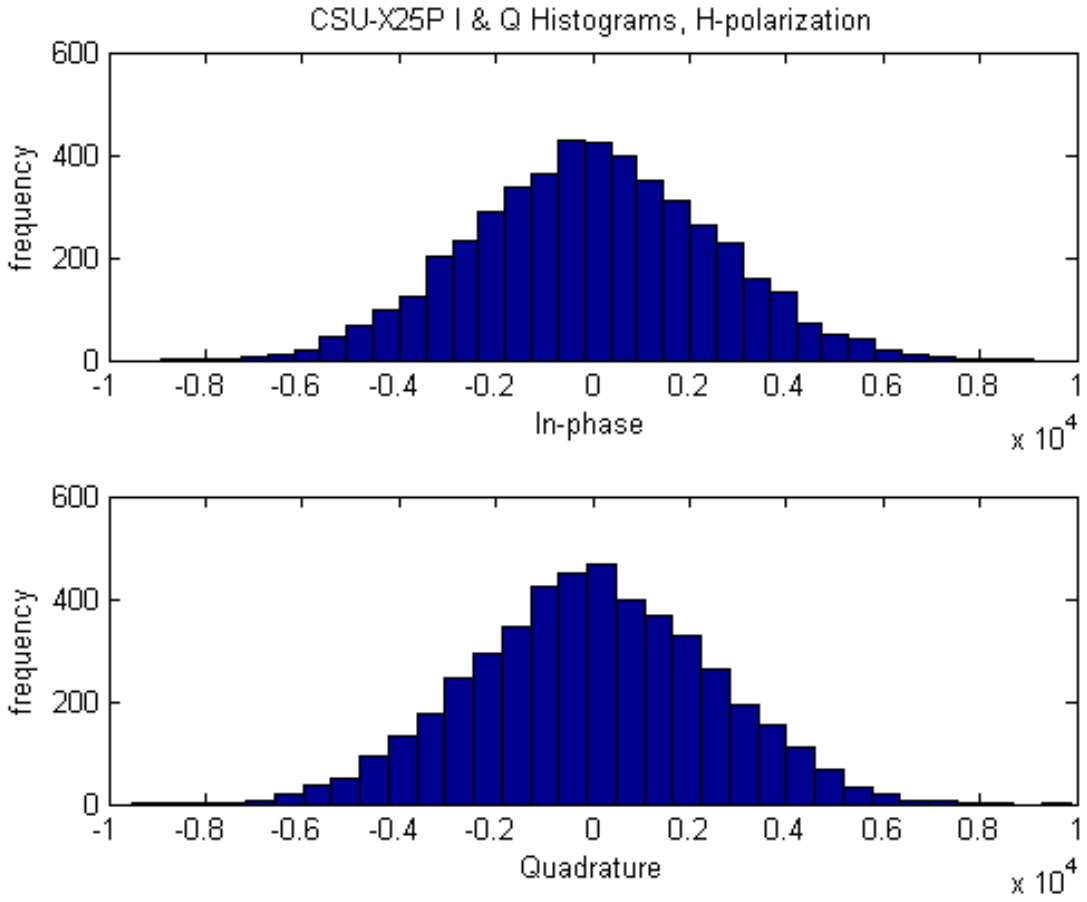

Figure 3.1: In-phase (I) and Quadrature phase (Q) components of the received signal. Note the Gaussian shape with zero mean.

2. The means of I & Q are zero,

$$E\big[I[(t)\big] = E\big[Q(t)\big] = 0 \tag{3.14}$$

3. The I & Q components have the same variance,

$$E\big[I^2(t)\big] = E\big[Q^2(t)\big] = \sigma^2 \tag{3.15}$$

4. The real and imaginary parts have the same autocorrelation function,

$$E\big[I(t_1)I(t_2)\big] = E\big[Q(t_1)Q(t_2)\big] = \sigma^2\rho_0(t_2 - t_1) \tag{3.16}$$

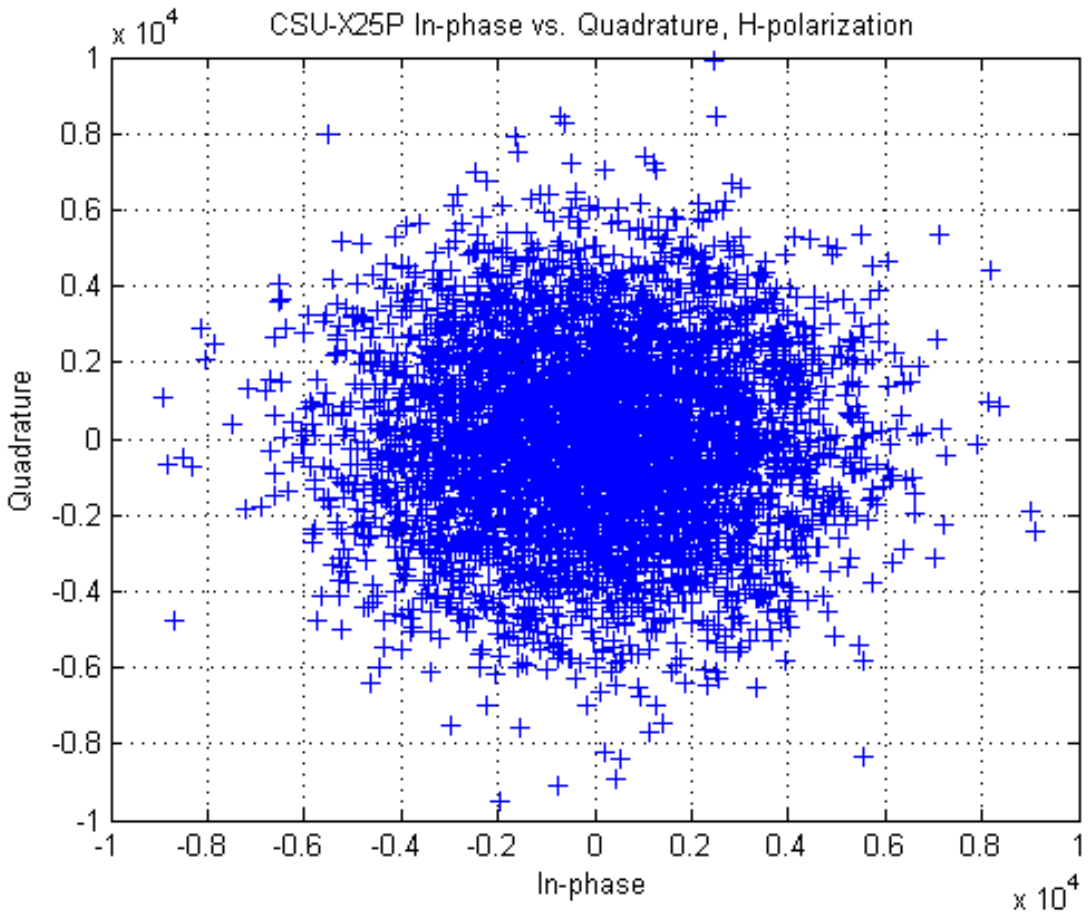

Figure 3.2: Scatter plot of I & Q components of the received signal. Note that I & Q are uncorrelated.

5. The I & Q components at two different times, are correlated

$$E\big[I(t_1)Q(t_2)\big] = -E\big[I(t_2)Q(t_1)\big] = \sigma^2\alpha_0(t_2 - t_1) \tag{3.17}$$

Time series data samples collected by the CSU-X25P radar in precipitation were analyzed to illustrate the properties of a stochastic process. Figure 3.1 shows the histograms of I and Q which are similar to Gaussian density functions, with zero mean. Also, the similarity in their distribution suggests they have the same variance. Figure 3.2 shows that the scattergram of I vs. Q is spread equally, without any preferential direction, indicating they are independent. Figure 3.3 shows the histogram of the power samples, $(I^2 + Q^2)$, having a near linearly

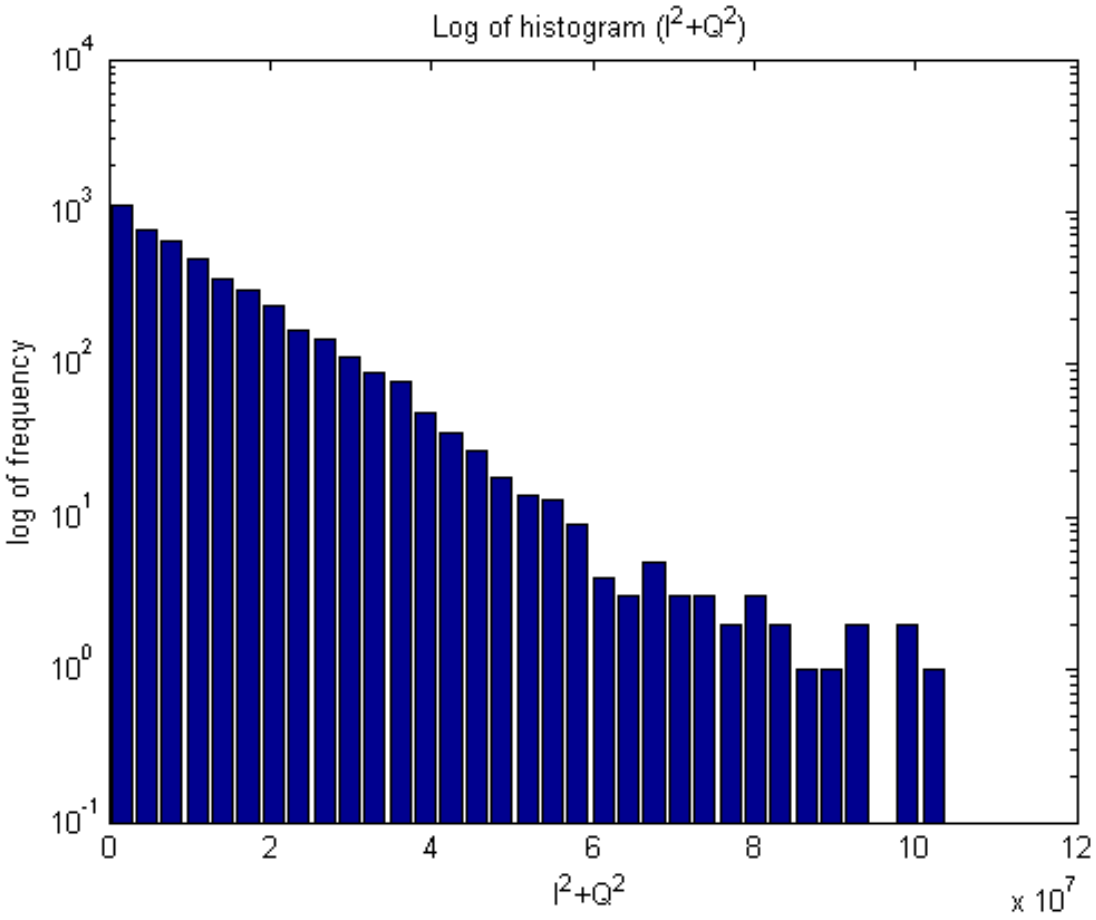

Figure 3.3: Log histogram of (I^2+Q^2). The linear decrease indicates I^2+Q^2 is exponentially distributed.

decreasing form indicating an exponential distribution, as expected for a probability density function of signal power given by,

$$f_P(P) = \frac{1}{2\sigma^2} e^{-P/2\sigma^2}, \qquad P > 0. \tag{3.18}$$

It is evident from the previous figures that the sampled In-phase and Quadradure phase components of a typical rain event satisfy the properties of a valid stochastic process. This validation will ensure accurate estimation of the Doppler data moments to be calculated.

3.3 Reflectivity (Z)

Reflectivity, η, is the general radar term describing the volumetric backscatter cross-section per unit volume, and is calculated from the received complex signal envelope, derived from the discrete I&Q components at the output of the digital receiver. The reflectivity from meteorological backscatterers can be written as, $\eta = (\pi^5/\lambda^4)|k_w|^2 Z_e$. The equivalent reflectivity factor Z_e can be estimated from the received power, P, using the weather radar equation [12], shown here in units commonly used by radar meteorologists,

$$P(mW) = \frac{\pi^5 10^{-17} P_t(W) G^2 G_r \tau(\mu s) \theta_{3dB}^2(deg) |k_w|^2 Z_e(mm^6/m^3)}{6.75\text{x}2^{14}\ \ln 2\ r^2(km)\lambda^2(cm) l^2 l_r} \tag{3.19}$$

Receive power at range r, $P(r)$ is measured in mW, transmit power P_t in Watts, antenna and receiver gains, G and G_r are dimensionless, transmit pulse width τ in micro seconds (μs), antenna 3dB-beamwidth (H and V) θ_{3dB} in degrees, the dielectric factor of water $|k_w|^2 = |(\epsilon_r - 1)/(\epsilon_r + 2)|^2$ where ϵ_r is the complex relative permittivity of water, the range r is in kilometers, wavelength λ is in centimeters, and attenuation and receiver losses, l and l_r are dimensionless. The equivalent reflectivity factor Z_e is simply referred to, by radar meteorologists, as reflectivity for H,V polarizations at a range r, $Z_{h,v}(r)$ measured as $mm^6 m^{-3}$ in dBZ.

By rearranging the weather radar equation the reflectivity, at range r, for a given power measured at the H and V channel outputs of the digital receiver, can be expressed as,

$$Z_{h,v}(r) = \left(\frac{6.75\text{x}2^{14}\ \ln 2}{\pi^5 10^{-17}}\right)\left(\frac{l_r\ G^2}{\tau\ \theta_{3dB}^2\ |k_w|^2}\right)\left(\frac{\lambda^2(f_{DDS}, f_{NCO})\ l^2}{P_t\ G_r(f_{DDS}, f_{NCO})}\right) r^2\ P_{h,v}(r) \tag{3.20}$$

where the quantities within the parentheses represent parts of the radar system constant $C = C_k C_s C_d$, C_k is a numerical constant, C_s is dependent on static system hardware parameters including the antenna and receiver gains, and C_d is dependent on dynamic hardware parameters such as sampled transmit frequency and associated automatic frequency control parameters (i.e., f_{DDS}, f_{NCO}) set during the coherent-on-receive step. For example, the transmitted wavelength perturbations are due to the random variations in frequency output

from the magnetron, and calculated as $\lambda(f_{DDS}, f_{NCO}) = c/(f_{DDS} + f_{NCO} + f_{STALO})$, where the STALO frequency is fixed at 8900 MHz, and the DDS and NCO frequencies vary depending on the estimated frequency of the sampled transmit pulse. It is widely accepted in the radar meteorology community to represent Z using a logarithmic scale and written as,

$$Z_{h,v}(r) = 10\log[\ C\ P_{h,v}(r)\ r^2] \qquad [\text{in } dBZ] \tag{3.21}$$

and will henceforth be referred to in dBZ.

3.4 Doppler Velocity (v_d)

Meteorological events include precipitation with varying phases including rain, hail, snow, ice, and everything in between which can be detected by its equivalent reflectivity factor. But, in order to better understand the event from initiation to extinction, and to provide reasonable forecasting, the Doppler velocity v_d is an essential observation. The CSU-X25P radar node employs the coherent-on-receive technique, by means of detecting the transmit pulse phase of the magnetron, which can later be removed thus only leaving Doppler shifts introduced by the weather echoes.

In a pulsed radar, the received voltage $V_r(t)$ is due to backscattering by particles in the resolution volume at a particular range-time $t = \tau_s = 2r/c$. Transmit pulses are separated in time by a period $PRT = T_s$, and thus for a particular range-time the voltage can be seen as a sequence of temporal samples at $V_r(\tau_s)$, $V_r(\tau_s + T_s)$,... $V_r(\tau_s + mT_s)$. Due to the random nature of the time-varying properties of the hydrometeors, sample-time fluctuations in the received voltages can be treated as a complex stochastic process. Assuming the average velocity $\overline{v_d}$ and spectral width σ_v define a Gaussian-shaped Doppler spectrum, the sample-time autocorrelation function is given by [8],

$$R[n] = S_0\ exp\bigg(-\frac{8\pi^2\sigma_v^2 n^2 T_s^2}{\lambda^2}\bigg) exp\bigg(-j\frac{4\pi\overline{v_d} n T_s}{\lambda}\bigg); \qquad n = 1, 2, ...N \tag{3.22}$$

where $S_0 = |R[0]|$ is the magnitude of the autocorrelation at lag 0, and the correlation

coefficient can be expressed as $\rho[n] = R[n]/R[0]$. From the above relationships, we can obtain the power spectral density (i.e., Doppler spectrum) from the autocorrelation function by,

$$S(\Omega) = \sum_{n=-\infty}^{\infty} R(n)e^{-j\Omega n}, \tag{3.23}$$

where $S(\Omega)$ is the discrete time Fourier transform of the autocorrelation function, with Doppler frequency components in the interval (-π, π). The Doppler velocity spectrum is thereby given as,

$$S(v) = \frac{S_0}{\sigma_v\sqrt{2\pi}} exp\bigg(- \frac{(v-\overline{v})^2}{2\sigma_v^2}\bigg) \tag{3.24}$$

where the mean velocity is $\overline{v} = -\frac{\lambda}{4\pi T_s}\overline{\Omega}$ and the standard deviation of velocity is $\sigma_v = \frac{\lambda}{4\pi T_s}\sigma_\Omega$.

The maximum radial velocity that can be observed without aliasing is $v_{max} = -\lambda f_{max}/2 = -\lambda/4T_s$, where $f_{max} = 1/2T_s$ and the maximum unambiguous range is defined as $r_{max} = cT_s/2$. Their product $v_{max}r_{max} = c\lambda/8$, fixed by the radar wavelength, shows that an increase in maximum range comes at the cost of a decrease in maximum unambiguous velocity, and vice versa. This is one of the fundamental relationships taken into account by radar engineers when designing a pulsed Doppler radar system.

In [13] and [14], the authors present a parametric estimation algorithm for X-band pulsed Doppler radars that provides improved performance in estimation of spectral moments in the presence of strong clutter signals, with a lower number of samples. With shorter dwell times, increased scan rates can be achieved without losing the ability to achieve higher Nyquist velocities up to 38 m/s, using dual-PRF waveforms. The authors also presented a table of optimal dual-PRF waveforms for various scan speeds (deg/s), PRF combinations (PRF_1 and PRF_2), 3/4 stagger ratio of pulse blocks (i.e., $N_1 = 40$, $N_2 = 54$), detectable Doppler velocities and Azimuthal resolution. In practice, the mean Doppler velocity for each block of pulses is computed and then combined for an extended unambiguous interval as, $\mp\lambda/4(T_{s1} - T_{s2})$. The waveforms thereby presented were used as a guideline to improve operation of the CSU-X25P radar node.

3.5 Differential Relectivity (Z_{dr})

The CSU-X25P radar node is a dual polarized radar system operating in a hybrid mode, with a transceiver that simultaneously transmits, then receives both Horizontally and Vertically oriented signal waveforms. There are many advantages polarimetric radars have, mainly their ability to obtain two different "looks" from the same resolution volume, in range. Because the transceiver has independent dual-linear channels, estimated powers for the H- and V-channels can be found as,

$$\hat{P}_{h,v} = \frac{1}{N}\sum_{n=1}^{N}\left|V_{h,v}[n]\right|^2, \tag{3.25}$$

for N samples. The average axis ratio of particles, such as precipitation in the resolution volume can be estimated based on the differential reflectivity $\hat{Z}_{dr}$, or estimated ratio of reflected power from the H- and V-polarizations as,

$$\hat{Z}_{dr} = 10log\left(\frac{\hat{P}_h}{\hat{P}_v}\right) \qquad \text{[in dB]}. \tag{3.26}$$

From the differential reflectivity estimate, radar meteorologists can measure rainfall and discriminate hydrometeor types as described in [8, 12]. As Z_{dr} increases, in the absence of severe attenuation, it can be inferred that the horizontal radar cross section of raindrops is greater than the vertical, which is indicative of larger raindrops reaching hydrostatic equilibrium. Once a raindrop reaches terminal velocity, the larger its fluid volume, the more it spreads horizontally, thus yielding values of $Z_{dr} > 2$ dB. For very small raindrops, with lower reflectivity values, this ratio will be closer to unity (or 0 dB). It must be noted though, that hail will also have differential reflectivity values near 0 dB, but will also have large reflectivity values, typically above 50 dBZ.

The differential reflectivity measurement is affected by imbalance in boresight antenna gains and orthomode transducer channel differences in orthogonal signal propagation via the feedhorn. To account for this, a procedure presented in [15] to calibrate Z_{dr} using properties of the rain medium was followed. They suggest collecting rain data with the antenna

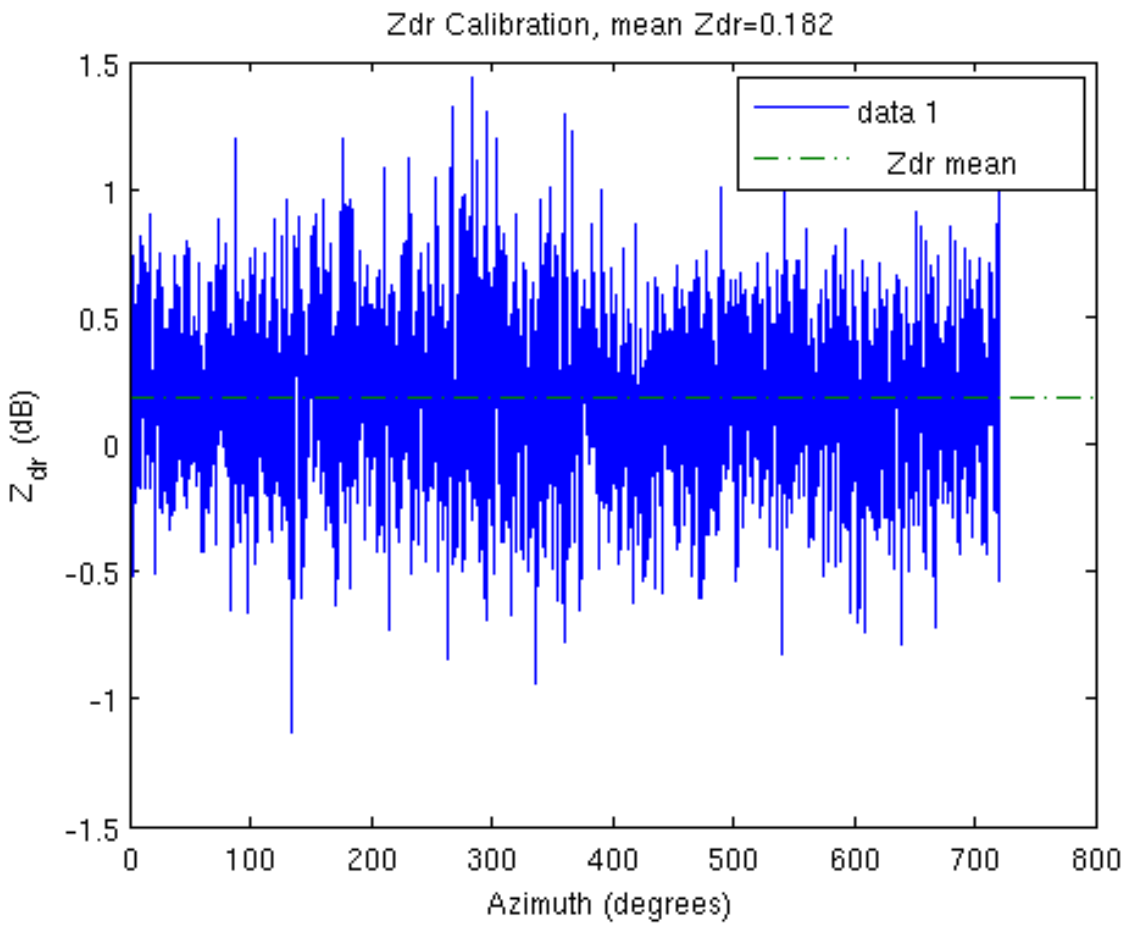

Figure 3.4: CSU-X25P Z_{dr} Calibration

pointed at an elevation of 90°, while rotating 360° in azimuth. When viewed at vertical incidence, raindrops are azimuthally symmetric with a Z_{dr}= 0 dB, and as the polarization basis rotates it is periodic with the azimuth angle. The measured Z_{dr} is also periodic, but independent of the scattering, and for data in the far field (i.e., range $\geq 2D^2/\lambda$ or ≥361 m), the mean differential reflectivity represents the gain imbalance in the two channels. The Z_{dr} correction factor for the CSU-X25P was found to be 0.18 dB as seen in Figure 3.4. It's important to note that when propagating through heavy rain the cumulative effects of differential attenuation will cause Z_{dr} to become negative, and will be apparent in the loss of horizontal reflectivity (Z_h) beyond the heaviest rain. Attenuation correction methods using the differential propagation phase (ϕ_{DP}) will be discussed later.

3.6 Differential Propagation Phase (ϕ_{DP}) and Specific Differential Phase (K_{DP})

The differential propagation phase measurement is obtained by taking the difference in phase between the horizontal and vertical polarizations, from simultaneous data profiles in the same range gate. The individual channel phase is obtained after phase-correction (i.e., removal of initial transmit pulse phase) to ensure it is due only to the received echoes. If we consider the simultaneous (i.e., lag 0) orthogonal received signal samples $V_h[n]$ and $V_v[n]$, in a hybrid transmission mode, the covariance is

$$\hat{R}_{h,v}[0] = \frac{1}{N}\sum_{n=1}^{N} V_v[n]{V_h}^*[n]. \tag{3.27}$$

From this the estimated correlation coefficient $\rho_{h,v}$ can be calculated as,

$$\hat{\rho}_{h,v} = \frac{\hat{R}_{h,v}[0]}{(\hat{P}_h\hat{P}_v)^{1/2}} \tag{3.28}$$

and subsequently its magnitude $|\hat{\rho}_{h,v}|$ and differential phase ϕ_{DP} as,

$$|\hat{\rho}_{h,v}| = \frac{|\hat{R}_{h,v}[0]|}{(\hat{P}_h\hat{P}_v)^{1/2}} \qquad \phi_{DP} = arg(\hat{R}_{v,h}[0]). \tag{3.29}$$

The differential propagation phase is always positive in rain and is a monotonically increasing function of range. Unlike reflictivity Z which is adversely affected by attenuation as the electric field propagates through rain, ϕ_{DP} does not experience extinction. An important property of differential phase is its independence from system gain calibration.

The magnitude of the correlation coefficient can be used to filter out unwanted reflectivity when displaying the weather echoes in a Planned Position Indicator (PPI) plot, where a typical value used is $|\rho_{h,v}| \geq 0.98$. A high correlation coefficient will also ensure a higher accuracy in the estimate of differential propagation phase.

Specific differential phase K_{DP} can be estimated as the range derivative of ϕ_{DP}, and is

valid between ranges r_1, r_2. The one-way finite difference estimate of K_{DP} is written as,

$$\hat{K}_{DP} = \frac{\phi_{DP}(r_2) - \phi_{DP}(r_1)}{2(r_2 - r_1)} \qquad \text{in } {}^{\circ}km^{-1} \tag{3.30}$$

while care should be taken in selecting the range interval to avoid sudden fluctuations in differential phase due to noise or other factors. Methods to improve the accuracy of the K_{DP} estimate by smoothing of, or applying a linear / non-linear regression fit to, the range profile of ϕ_{DP} can be found in [8].

A rain rate estimate based on K_{DP} can be written in the form presented by (Sachidananda and Zrnic, 1986) as,

$$R(K_{DP}) = aK_{DP}^{b} \qquad \text{in mm } hr^{-1} \tag{3.31}$$

where the values for coefficient a and exponent b are frequency dependent and found empirically. In [16] the authors found that for $R < 30$ mm hr^{-1}, with $\lambda = 3.2$ cm, assuming an oblate equilibrium drop shape aspect ratio, the lognormal distribution coefficient $a = 12.1$, with an exponent of $b = 0.85$. The rain rate estimate accuracy is also dependent on the range interval selected for K_{DP}, and should be taken from the lowest elevation angle possible.

3.7 Clutter Suppression

For any pulsed radar, the echoes will most likely contain strong returns from unwanted ground targets such as buildings, trees, or mountains. These returns, typically in the 40 to 60 dBZ range are backscatter from the main beam at boresight or from a sidelobe of the antenna, and are referred to as *ground clutter*. These non-meteorological targets bias the reflectivity and velocity estimates, and must be mitigated in order to extract the observed meteorological phenomena. The clutter contaminated weather echo can be modeled with a spectral density given by,

$$S_m(\boldsymbol{\mu}) = \frac{S_c}{\sqrt{2\pi\sigma_c^2}} exp\left(\frac{v_k^2}{2\sigma_c^2}\right) + \frac{S_0}{\sqrt{2\pi\sigma_v^2}} exp\left(-\frac{(v_k - v_m)^2}{2\sigma_v^2}\right) + N \tag{3.32}$$

where $\boldsymbol{\mu} = [S_c\ \sigma_c\ S_0\ v_m\ \sigma_v\ \mathrm{N}]^T$, subscript "c" refers to clutter parameters and N refers to the noise power density.

The CSU-X25P uses a real-time spectral fit clutter filter as implemented in [13, 14], where the zero-velocity clutter spectral coefficients are notched with a spectral clipper, using a Gaussian model for the clutter spectral density. A Gaussian weather spectral density is recursively fit to the remaining points and the notched spectral coefficients are interpolated with the model. The filtered signal will experience up to a 50 dB clutter suppresion ratio, but unfortunately may lose weather echoes with low radial velocity.

CHAPTER 4

System Validation with the CSU-CHILL Radar and Deployment on the Western Coast of Puerto Rico

4.1 Description of Validation with CSU-CHILL Radar

The CSU-X25P radar test node was assembled and tested on site at the CSU-CHILL Radar Facility in Greeley, CO, so it was natural that it would be validated with this firmly established research radar. During the validation period, the CSU-CHILL radar was a single frequency S-Band, high power, dual polarized, Doppler weather radar, and is well recognized among researchers in this community. It has since gone through major upgrades where it was recently modified to be a dual-frequency (S- and X-band) dual-polarization Doppler weather radar.

For the validation, CSU-X25P and CSU-CHILL simultaneously collected data during convective storms in the fall of 2010. Care was taken to coordinate RHI and PPI scans of the two radars during these events, to maximize the amount of data available for analysis. The CSU-X25P radar was secured to a concrete pad at ground level, and due to blockage from structures on the property, it only had 180° of unobstructed views to the North, between $270° \leq AZ \leq 90°$. Minor sectors available to the south were used for comparison in setting a benchmark.

A typical coordinated scanning effort occurred while the CHILL radar was collecting precipitation data for other research projects, typically focused over rain gauges in the Denver metro area, to the south. The X25P radar took advantage of the ongoing operations by requesting to be included in the scan strategies planned for the particular experiment, whenever available. It was during these operations that the author gained firsthand experience on effectively operating a dual polarization, Doppler weather radar. This knowledge proved to be invaluable during operational training provided to UPRM personnel.

4.2 Coordinated Observations

On August 9, 2010, a convective storm was observed near Greeley, CO and coordinated scans were performed between CSU-X25P and CSU-CHILL radars. The coordination was done manually, while operators were both in the CHILL radar user van, sharing scan strategies. For reference in Figure 4.1, the one degree beamwidths of the transmit signals, for X25P and CHILL, are plotted versus range for elevation scan angles of 2° and 0.8°, respectively. The difference in elevation scan angles is due the location of the X25P near the ground, which has increased ground clutter in the lowest angles near the radar. The CHILL reflector is mounted on a pedestal, about 10 m above the ground, and experiences less interference at the lowest scan angles. In Figure 4.2(a) & (b), the coordinated PPI scans show good agreement in the first 22 km of the X25P, but due to higher reflectivites beyond that range, as seen in the CHILL plot, severe attenuation is observed for X-band. Note that although the elevation angles and scan start times are not perfectly synchronized there is good agreement in increasing differential phase, Φ_{DP}, as a function of radial range, as seen in (c) & (d). This is further highlighted in (e) & (f) by the Φ_{DP} range profiles, at an azimuth of 51.5°. It is important to note that as the transmit pulse propagates through oriented hydrometeors, the differential propagation phase, between the H and V receive echo phases, is inversely proportional to wavelength. Therefore, the X-band accumulation between the ranges of 10 km to 20 km is about three times that seen by the CHILL S-band radar. The noisy Φ_{DP} seen in both figures is a result of inaccurate estimation of differential phase in regions with lower cross-correlation coefficient (i.e., $\rho_{h.v} \leq 0.7$). This is more prevalent for a 3 cm wavelength where signal extinction occurs in horizontal polarization, before affecting the vertically oriented return, in heavy rain with large oblate raindrops.

A comparison was made between attenuation correction algorithms for reflectivity and differential reflectivity as presented by [17], and an algorithm for estimation of specific differential attenuation presented in [18]. The X25P implements the former in real-time, while a C code implementing the latter algorithm, known as DROPS, was used to obtain plots of the corrected reflectivity (CdBZ) and corrected differential reflectivity (CZdr), shown here

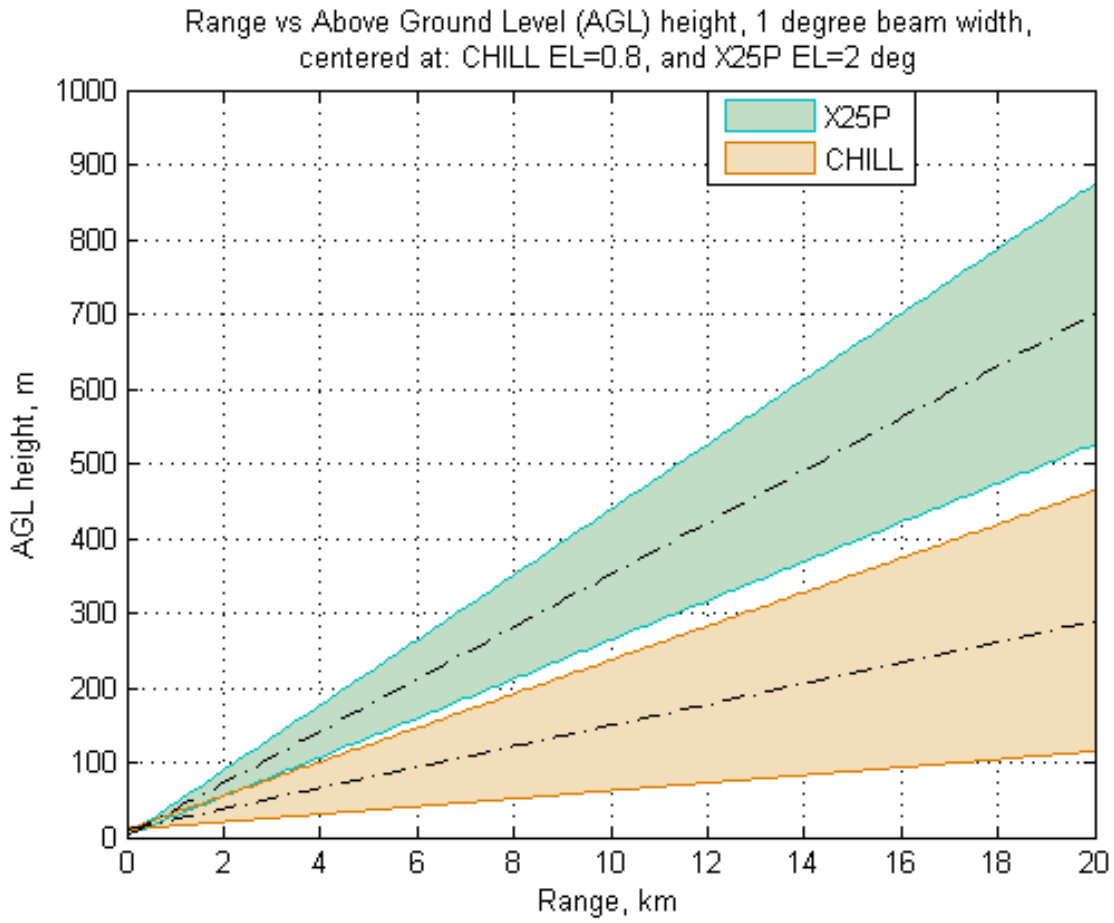

Figure 4.1: CSU-X25P vs. CHILL range profiles of 1° beamwidth. X25P centered at EL=2°, with starting height of 2 m. CHILL centered at EL=0.8° with starting height of about 10 m above ground level (AGL).

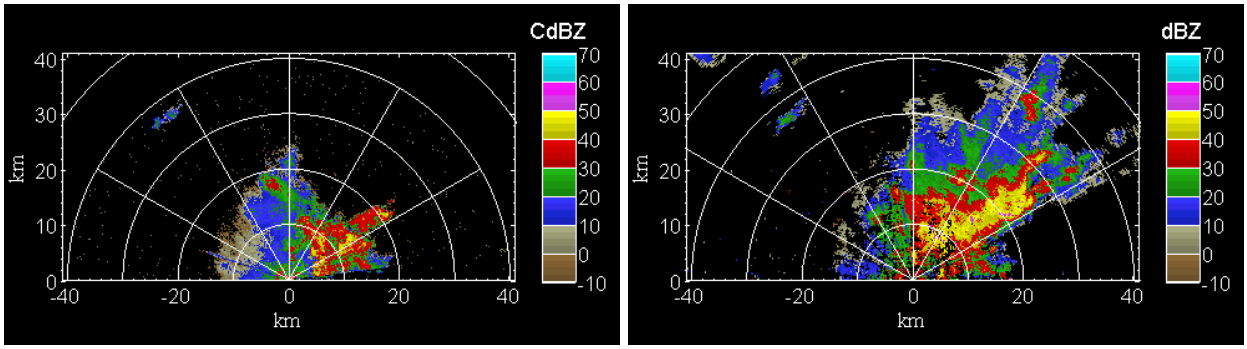

(a) X25P, CdBZ, 22:18:24 UTC

(b) CHILL, dBZ, 22:16:58 UTC

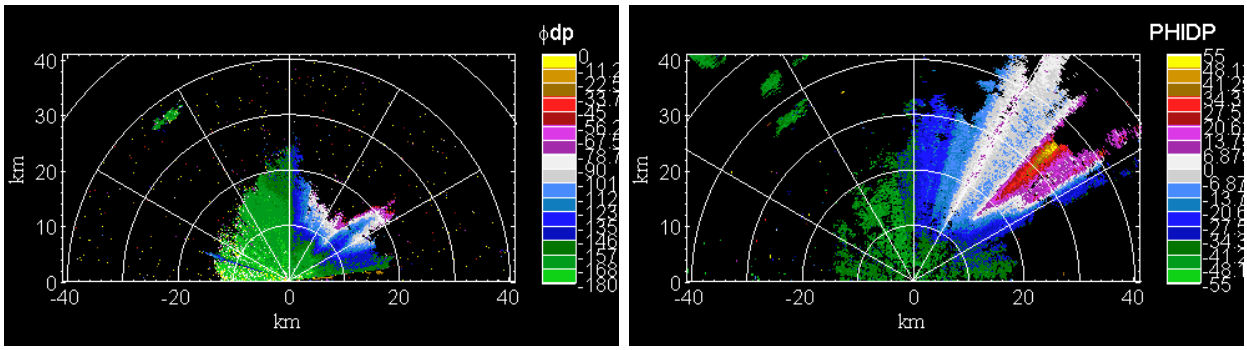

(c) X25P, Φ_{DP}, 22:18:24 UTC

(d) CHILL, Φ_{DP}, 22:16:58 UTC

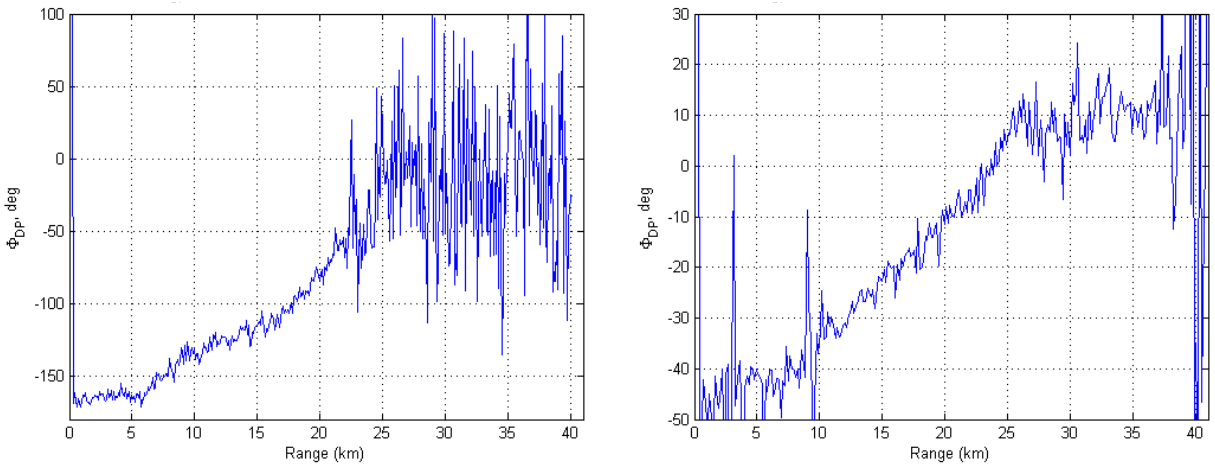

(e) X25P, $\Phi_{DP}, AZ = 51.5$, 22:18:24 UTC

(f) CHILL, $\Phi_{DP}, AZ = 51.5$, 22:16:58 UTC

Figure 4.2: X25P ($EL = 2°$) and CHILL ($EL = 0.8°$) PPI scans on 2010-08-09

in Figures 4.3(a)&(b). In both figures the measured and DROPS corrected range profiles were plotted together, as the best attenuation correction was obtained from the DROPS algorithm. The DROPS attenuation correction method was shown to provide up to 31.5 dB improvement for heavier rain, as seen at about 20 km range. The advantage of the Liu et al. algorithm is that it is implemented in real time, where DROPS is done in post processing. A direct result of attenuation correction, is a noticeable improvement (up to 3dB) in the negative bias in Zdr, becoming positive or near zero, due to the increase in horizontal reflectivity, Z_h after attenuation correction.

In Figure 4.4(a), the intensity plot of corrected Zdr vs. Z_h displays agreement with the expected relationship of drops with increasing oblate shape in heavier rainfall. The more oblate hydrometeors will have radar cross-sections with larger horizontal reflectivity, than for the vertical orientation. Here it is evident that in heavier rain ($Z_h \geq 20dB$), an almost linearly increasing differential reflectivity is obtained. For lighter rain ($Z_h \leq 20dB$), differential reflectivity is near zero, indicating more spherical hydrometeors with more similar Z_h and Z_v reflectivities. The intensity plot for specific differential phase, K_{DP}, versus corrected reflectivity in Figure 4.4(b), shows good agreement with the theoretical, and validated, $K_{DP} - Z_h$ relationship [19, 20].

4.3 Selected Observations

In Figure 4.5, the RHI scan at an azimuth of 217° shows good agreement between CSU-X25P and CSU-CHILL reflectivities and Doppler velocity. Due to ground clutter spectral filtering, the CSU-X25P inadvertently removes some meteorological data at the zero-velocity transition. There is good agreement in both radars, with respect to the location of the bright band at an altitude of 3 km, where the cross-correlation coefficient, ρ_{hv}, shows a band of lower values due to the decorrelation effect of the melting layer. However, the lower ρ_{hv} values of X25P at farther ranges are attributed to limited signal-to-noise ratio.

Figure 4.6 shows an RHI scan through a tropical rain event in June 2011, during the X25P deployment in Mayaguez, Puerto Rico, with a visible melting layer at about 4 km

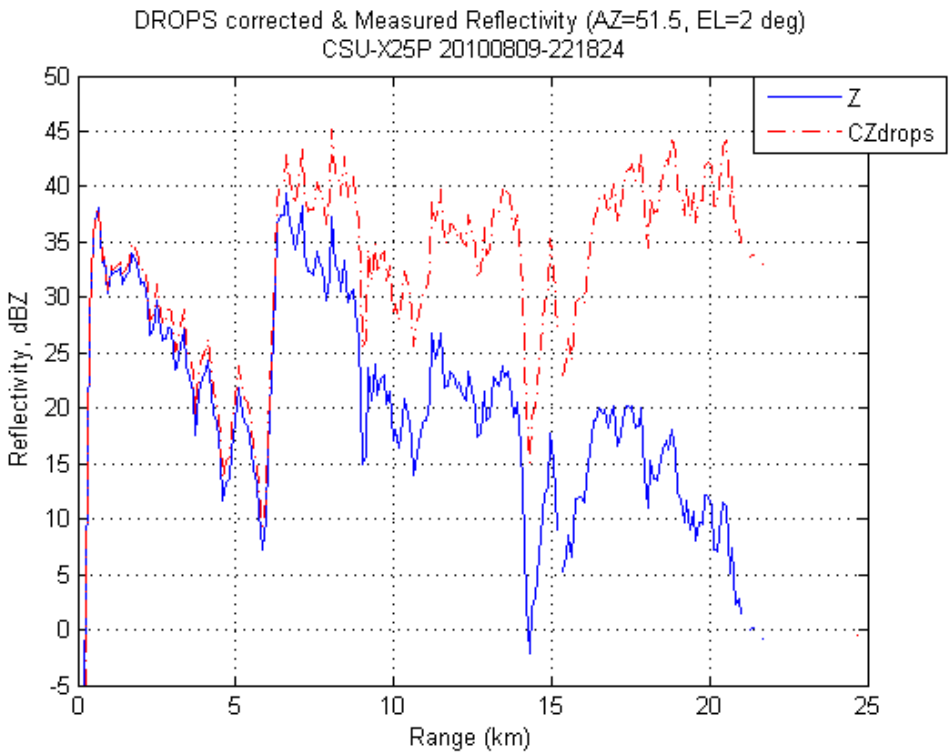

(a) Reflectivity and Corrected Reflectivity (dBZ)

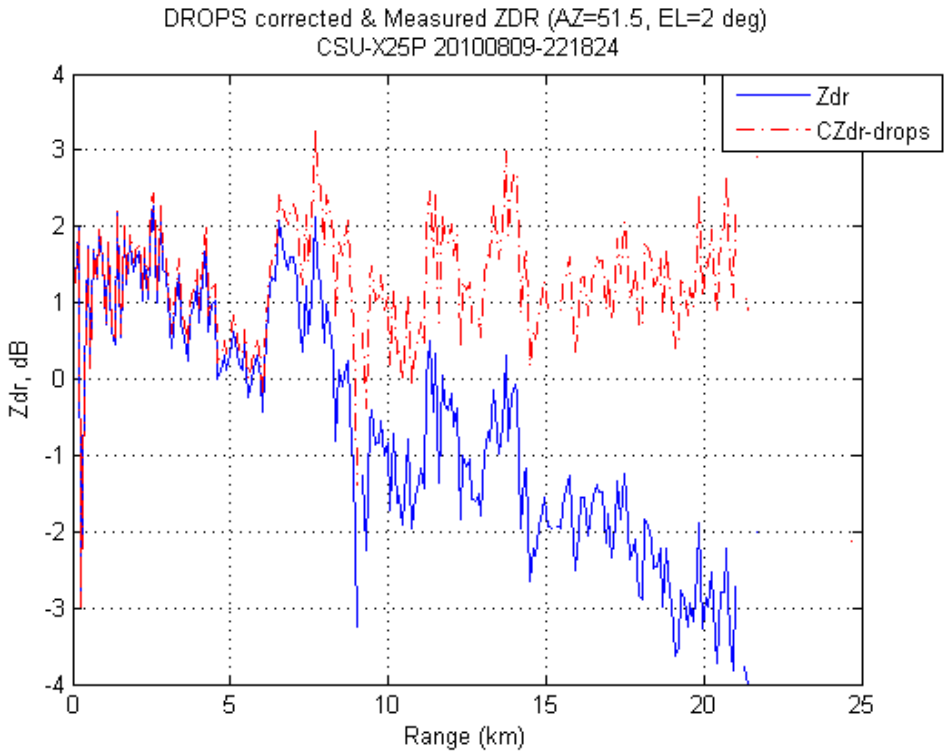

(b) Differential Reflectivity and Corrected Differential Reflectivity (dB)

Figure 4.3: X25P Measured vs. DROPS-Corrected Z_h and Zdr Range Profiles

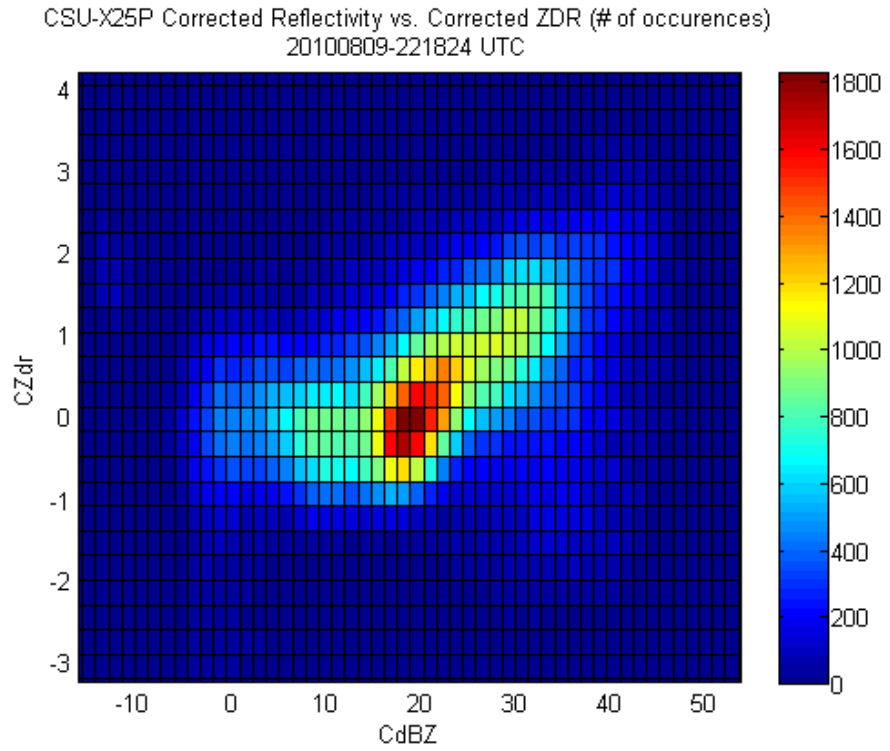

(a) Corrected Z vs Zdr

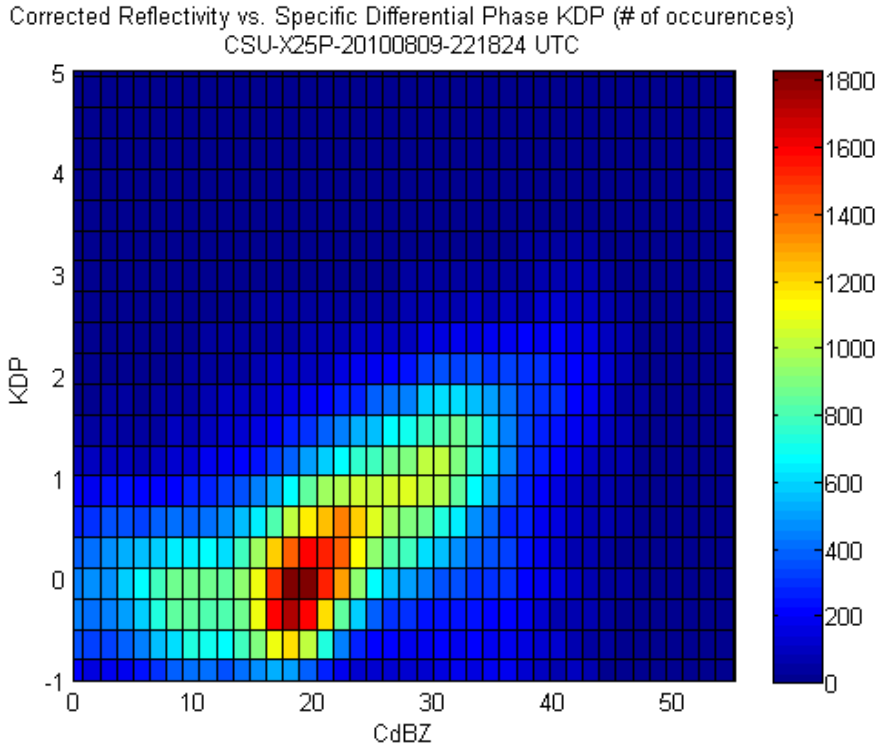

(b) Corrected Z vs K_{DP}

Figure 4.4: CSU-X25P Corrected Reflectivity vs. (a) CZdr and (b) K_{DP}.

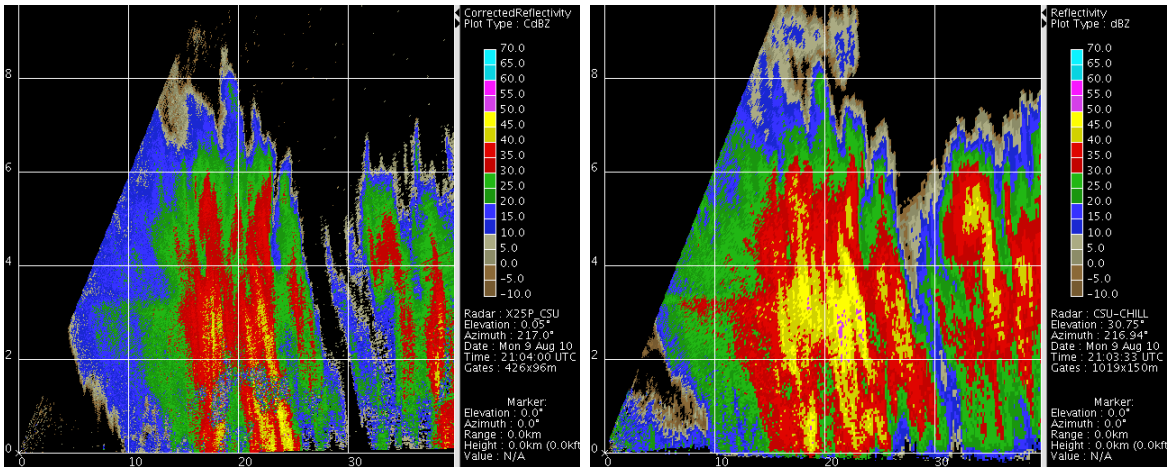

(a) X25P, Corrected dBZ, 21:04:00 UTC

(b) CHILL, dBZ, 21:03:33 UTC

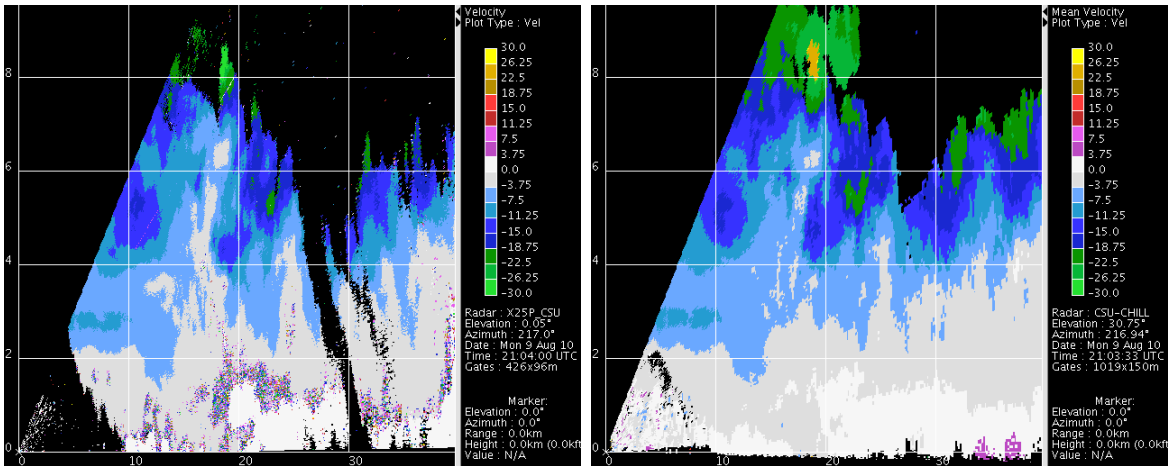

(c) X25P, Velocity, 21:04:00 UTC

(d) CHILL, Velocity, 21:03:33 UTC

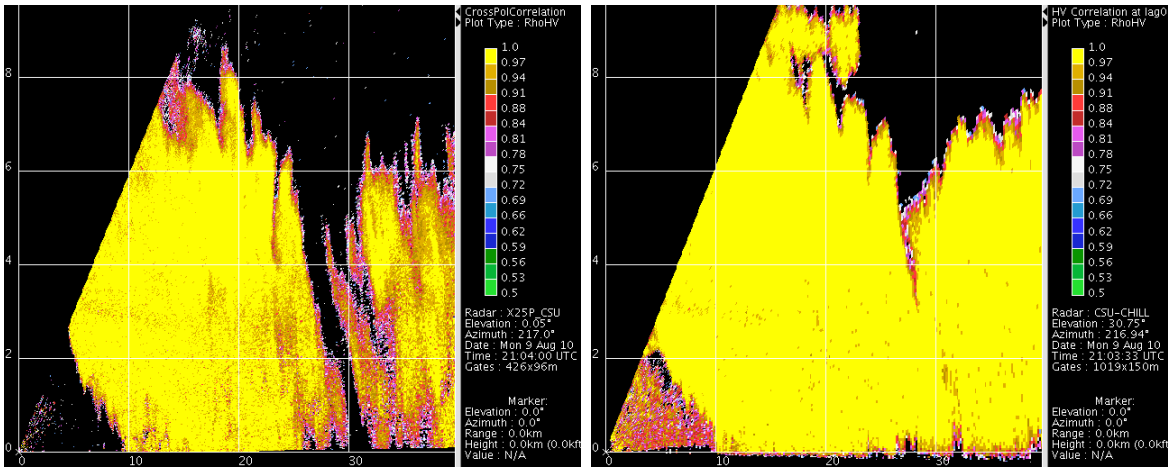

(e) X25P, ρ_{hv}, 21:04:00 UTC

(f) CHILL, ρ_{hv}, 21:03:33 UTC

Figure 4.5: CSU-X25P and CHILL RHI scans at AZ=217° on 2010-08-09 (UTC). Images created using CSU VCHILL.

above ground level (AGL). In (a) & (b) uncorrected reflectivity and differential reflectivity show signs of attenuation, highlighted by the negative bias in Z_{DR}. This is confirmed in (c) with a phase accumulation in Φ_{DP} of about 50°, through the region down range from from the heavier precipitation (at 15 km away from the radar and 4 km AGL). Considering the copolar cross-correlation coefficient in (d), we can see the decreasing ρ_{hv} due to the de-correlating effect of the melting layer, and also negative effect due to low SNR with increasing range. Using the reflectivity and differential reflectivity correction algorithms presented by Liu et al., we can obtain a more accurate estimate of these meteorological parameters, as seen in (e) & (f). Notice the improvement of the negative bias in Z_{DR}. An interesting observation regarding the location of the melting layer on the western coast of Puerto Rico is its height above ground level, with respect to that seen in Greeley, Colorado. The bright band was typically observed to be about 4.5 km AGL in this Tropical region, where a 2-3 km AGL height is typical in Colorado during the same season. Further investigation of the melting layer, and specific attenuation is needed to better understand this tropical environment and its effect on radar operations at X-band frequencies.

4.4 Deployment of CSU-X25P Radar to the Western Coast of Puerto Rico

Upon the agreement and validation with the CSU-CHILL radar, the CSU-X25P node was now ready for its first deployment. Through a collaborative effort between CSU and UPRM, the design of a three radar network, known as TropiNet [4], was underway with potential site locations and infrastructure being identified. The site selected to host Puerto Rico's first polarimetric X-band Doppler weather radar test node was the top of the R & D Building on the UPRM campus, geographically located at lat 18.2112°, lon −67.1368°, as seen in Figure 4.7.

The UPRM personnel procured and installed the twenty foot tower (Figure 4.8) and ensured the availability of adequate infrastructure such as power and network connectivity. Once the tower and infrastructure were in place, in the fall of 2010, the radar system was

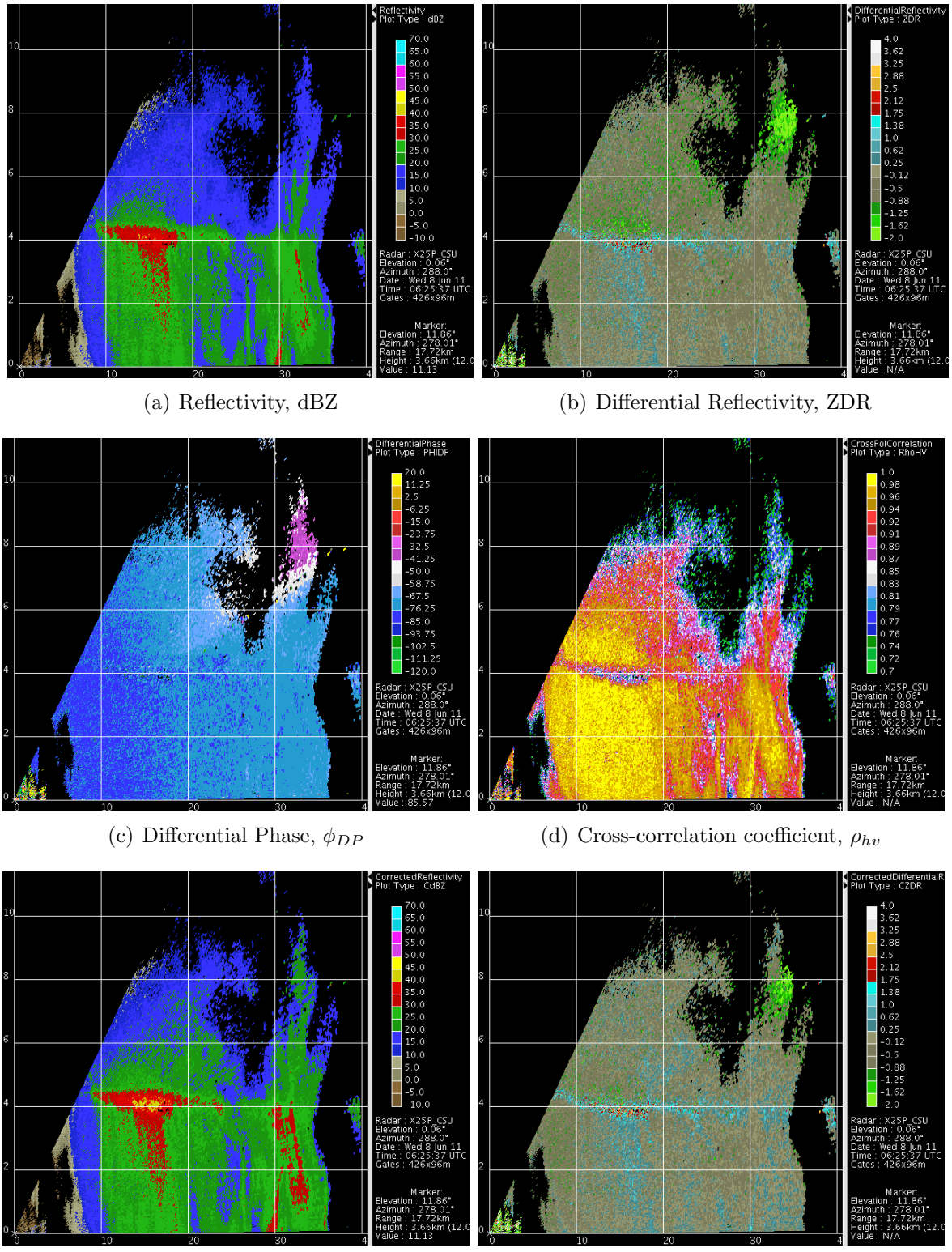

(a) Reflectivity, dBZ

(b) Differential Reflectivity, ZDR

(c) Differential Phase, ϕ_{DP}

(d) Cross-correlation coefficient, ρ_{hv}

(e) Corrected Reflectivity,CdBZ

(f) Corrected Differential Reflectivity, CZDR

Figure 4.6: Tropical rain event observed by X25P. RHI scan on June 8, 2011 06:25:37 (UTC), AZ= 288°. Images created using CSU VCHILL.

Figure 4.7: CSU-X25P 40 km range ring, centered at (18.2112, -67.1368). Image created using Google Earth and [1]

disassembled at the CSU-CHILL Radar facility and prepared for shipment to Mayaguez, Puerto Rico, as seen in Figures 4.9. The shipping of the radar system was coordinated such that its departure from Colorado avoided the harshest of winter conditions, as well as its arrival coinciding with Puerto Rico's dry season.

In mid January of 2011, the radar system was delivered to the R & D building on the UPRM campus. The author played a key role in disassembly and the assembly, which is an important aspect of the radar, that it should hold its system integrity in disassembly and assembly. Figure 4.10 captures the installation of the antenna control server, motors,

(a) Tower on R&D Building (b) Tower Structure

Figure 4.8: 20 ft. Tower Structure atop R&D Building, UPRM campus

pedestal, and 8 ft. parabolic antenna. Once the antenna and pedestal were secured to the tower, the azimuth and elevation motors, servo drives, and their associated cabling were installed. With this task completed, line power, control signaling, and Gigabit Ethernet cabling were also connected to the antenna control server enclosure and to the pedestal base riser.

With the radar transceiver, antenna, pedestal, motors, and antenna control server installed on the tower, the signal processing computer and mass storage device were housed in an environmentally controlled room inside the R & D building. A fiber optic link was made, between this computer and a gigabit Ethernet switch in the antenna control enclosure. An external gateway to the internet was established on the processing computer's Eth0 port. A solar calibration was done to account for any errors in the pedestal position control.

The collaboration between CSU and UPRM also served as a training opportunity that would enable the staff and students to locally operate and maintain the radar node. The

(a) Loading 8 ft. Antenna (b) Inside of Shipping Container

Figure 4.9: (a) 8 ft. antenna ready for shipment; (b) Loaded shipping container

author supervised and trained several UPRM graduate students about installation of a X-band dual polarization Doppler radar system, as seen in Figure 4.11. Additional support from CSU, via email and cellphone, was made possible by remote internet access to the radar node servers to assess system status, to restart processes, or identify potential root cause hardware failures. A key feature of this radar node is that it can be remotely operated, and as such, most of the collected data to be presented later in this chapter was obtained by the author, operating the radar from Colorado.

To assist in remote operations, a web camera was installed to provide a real-time visualization of the antenna. Having this view allows for safe remote operations, ensuring the tower platform is void of personnel and any obstructions. A radar control GUI is used to operate the radar (and can also be operated using scripts), while the GTK-based CSU-CHILL Real-time Display was adapted to display the CSU-X25P moment data, overlaid on a map of Puerto Rico. A web-based weather radar data visualization tool was developed by UPRM to simultaneously display moment data from NEXRAD (TJUA), CSU-X25P, and the Off-the-Grid radar nodes. Figure 4.12 shows a typical screen from the remote radar control server, with the Radar Control GUI, CSU-CHILL Real-time displays, a live feed from the video camera, and the web-based visualization tool.

It's been the author's experience that during CSU-X25P operations, it is beneficial to

(a) Raising servers, motors, etc.

(b) Raising Pedestal

(c) Raising Antenna

(d) Mounting Antenna onto Pedestal

Figure 4.10: Raising and mounting the pedestal, antenna, equipment onto building

(a) Inspecting Elevation wiring panel (b) Wiring Pedestal line power, etc.

Figure 4.11: UPRM graduate students: radar installation training

have access to NEXRAD or Terminal Doppler Weather Radar (TDWR) data. The advantage of having the longer (radial) range reflectivity and Doppler velocity PPIs (NEXRAD= 230 km; TDWR= 90 km) from these radars provides the operator ample time to plan future scans in the lowest altitudes of incoming weather, using the faster scanning, shorter range, but higher resolution X-band radar. For example, based on the reflectivity from the TJUA radar in Figure 4.12b, and assuming easterly winds, a sector volumetric scan pattern can be planned between $90° < AZ < 215°$.

4.5 First Observations in a Tropical Environment

One of the first interesting weather events captured occurred on April 26, 2011 when low velocity circulation ($\pm 8 m/s$) was observed just off the northwest coast, near Rincon, PR, as presented in [21]. In Figure 4.13, a velocity couplet indicating counterclockwise circulation was detected at approximately 25 km from the radar node, centered around azimuth 336°, shown here at an elevation of 3°. Waterspouts, having similar signatures, are commonly seen along the West coast of Puerto Rico and have been known to make landfall, damaging property and causing injuries, in the immediate vicinity. The NWS Weather Forecast Office website (http://www.crh.noaa.gov/apx/science/waterspouts/waterspouts.php) defines two waterspout types: tornadic and fair weather. Tornadic waterspouts develop downward from a thunderstorm like tornadoes, and can form over water, or move from land onto water.

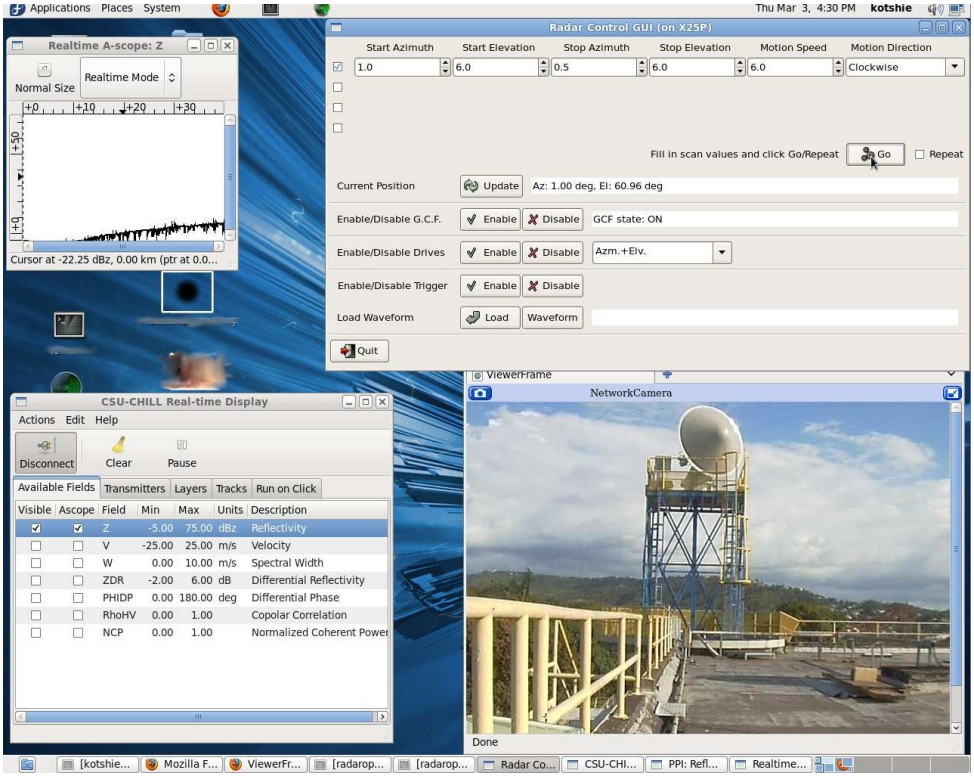

(a) Control GUI, Real-time Display Control, and Live Video

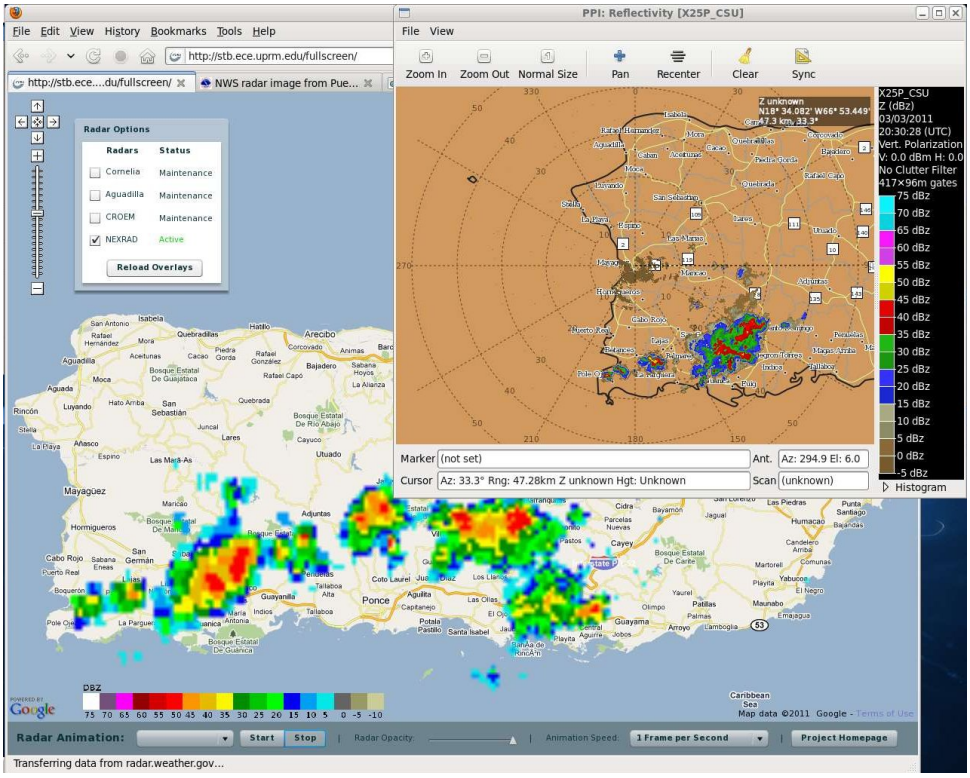

(b) Real-time Display, UPRM web tool displaying NEXRAD data (background)

Figure 4.12: CSU-X25P Radar Control and Visualization Tools

Fair weather waterspouts form in light wind conditions and develop on the warm water surface and work their way up toward the much colder flat base of developing cumulus clouds. Figure 4.14 shows a waterspout that formed off the coast of Mayaguez, in September of 2005. For the event of April 26^{th}, ground validation of a water spout was not available probably because the circulation was observed several kilometers offshore, where the altitude at this range was approximately 1.3 km above sea level. The significance of capturing this event demonstrates the need for a network of shorter-range, higher resolution, and faster scanning of the lowest altitudes along the West coast of Puerto Rico, like that proposed by the TropiNET radar network.

4.5.1 Tropical Storm Emily

During its first year of deployment, the CSU-X25P radar was operated both locally and remotely from Colorado, during tropical storms and hurricanes. Depending on the time of year, the time difference between Puerto Rico and Colorado is +2 or +3 hours and thus operational duties are shared to maximize data collection of entire events. In early August of 2011, Tropical Storm Emily formed in the Caribbean Sea and was tracked over 200 km south of Puerto Rico. But as seen from the night time infrared satellite and NEXRAD reflectivity WunderMap images (www.wunderground.com) in Figure 4.15, Emily reached out well north of Puerto Rico bringing several north-westbound rain bands across the island, due to the counterclockwise rotation of the storm. The direction of the rain bands is further highlighted by the relative storm tracks present in the TJUA reflectivity image. The UPRM team and the author shared operational duties in the data collection of Tropical Storm Emily.

Most rain events observed by CSU-X25P, while deployed in Puerto Rico, have easterly to southeasterly winds, either dissipating over land or continuing westward toward the Dominican Republic. But as seen in the selected images from CSU-X25P during TS Emily (Figure 4.16), this was not the case. Due to its vortex centered in the Caribbean Sea and its counterclockwise rotation, the rain bands observed had southerly or southeasterly winds with velocities in the $\pm 25 m/s$ range. Figures 4.17(a-d) further show RHI scans where the relative

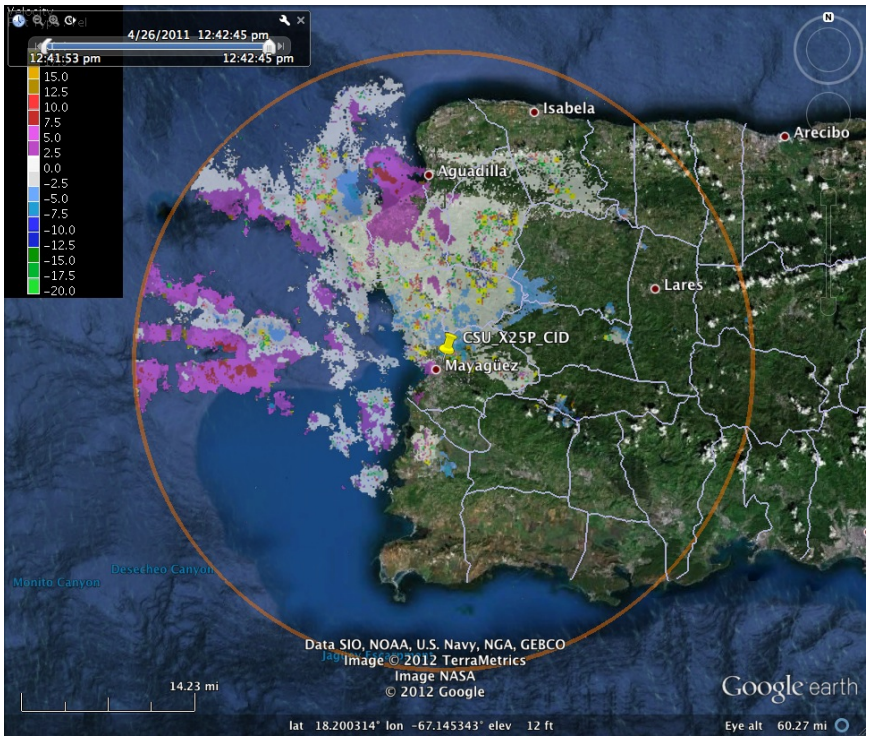

(a) Doppler Velocity PPI from CSU-X25P, EL=3°

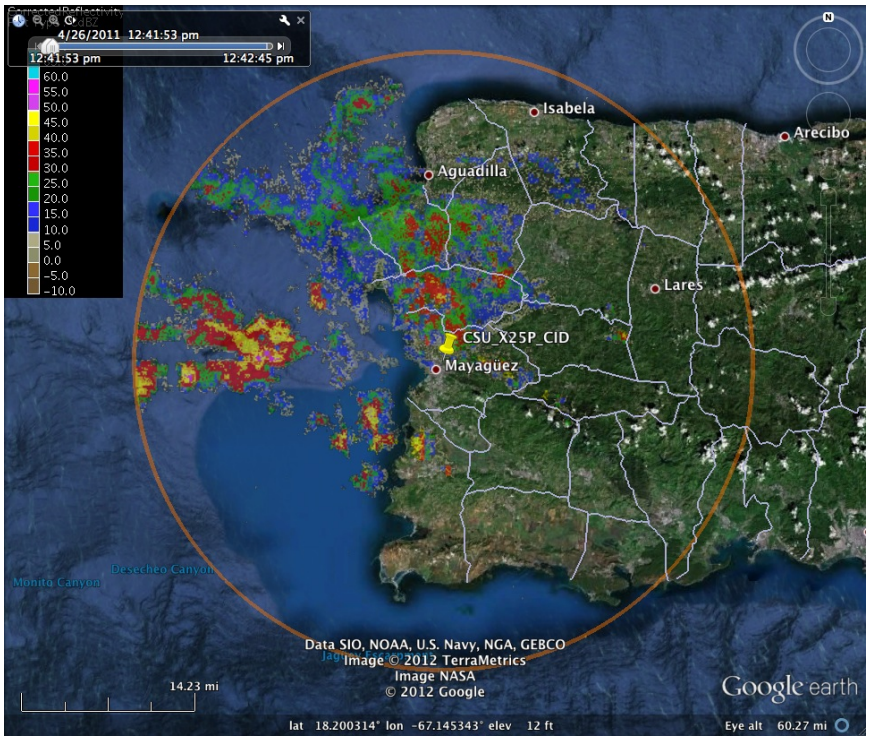

(b) Corrected Reflectivity PPI from CSU-X25P, EL=3°

Figure 4.13: Circulation off coast of Rincon, PR on 26 April 2011 18:42:45 UTC. Images created using CSU VCHILL and Google Earth

Figure 4.14: Waterspout off coast of Mayaguez, PR in September 2005 (photo courtesy of UPRM CLiMMATE Lab)

storm movement of the entire vertical column clearly indicates tropical storm strength inbound velocities from $AZ = 118°$, and outbound velocities through the $AZ = 303°$ direction. A more typical RHI scan through a thunderstorm would indicate inbound velocities in the lower altitudes below 2 km, with perhaps outbound movement of the cloud tops. Due to the size and relative location of the tropical storm, one rain band crosses the entire island and covers most of the PPI scan range.

4.5.2 Hurricane Irene

Twenty days later, from August 20-29, Hurricane Irene was first tracked as a tropical storm, with unusually high sustained winds, east of the Lesser Antilles, then gradually peaking as a Category 3 hurricane with 120 mph winds, while over the Bahamas. Irene was the first and largest hurricane of the 2011 Atlantic hurricane season, eventually making landfall over New York, then moving over northern New England as seen in the storm track of Figure 4.18. Hurricane Irene caused hundreds of millions of dollars in damage, especially in Puerto Rico

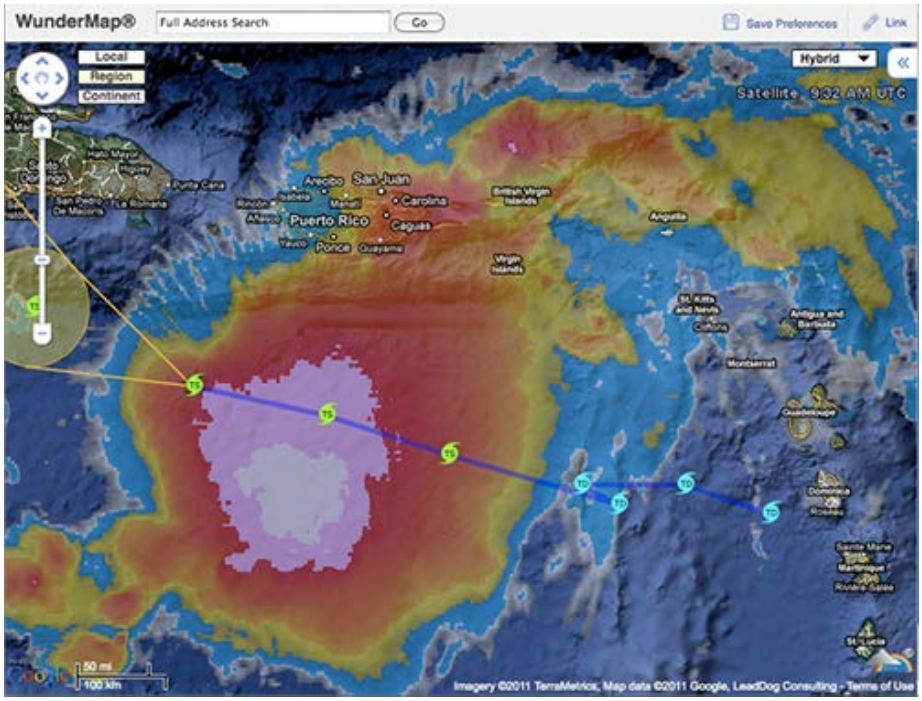

(a) Infrared Satellite image, 09:32 UTC

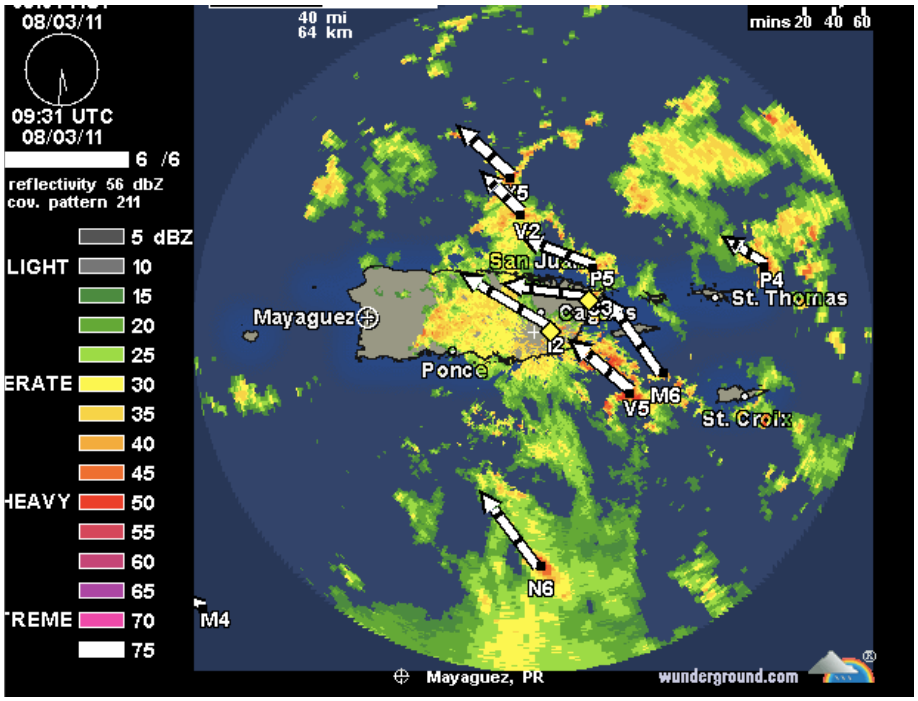

(b) TJUA NEXRAD Reflectivity, 09:31 UTC

Figure 4.15: Tropical Storm Emily on 3 August 2011: (a) Infrared satellite storm track, and (b) TJUA reflectivity with relative storm tracking enabled (images created using Weather Underground's WunderMap web application)

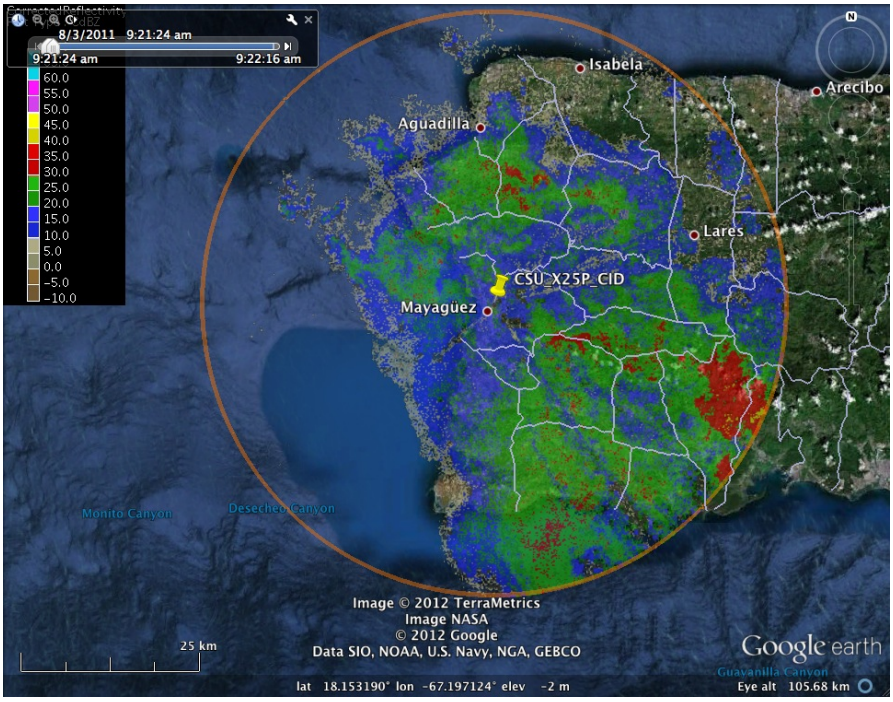

(a) Corrected dBZ (scale -10 to 70)

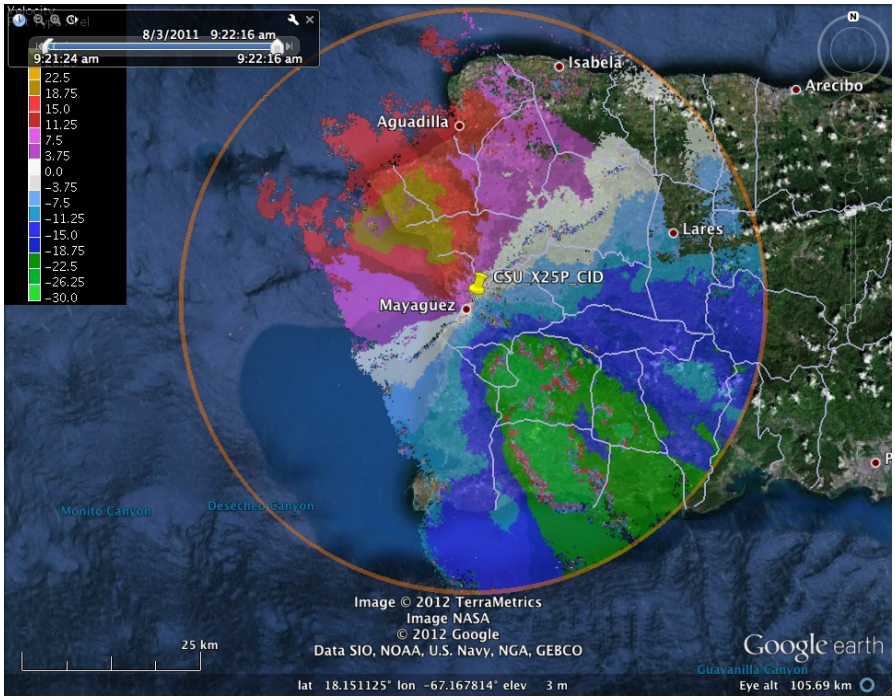

(b) Doppler Velocity (scale -30 to 30 m/s)

Figure 4.16: CSU-X25P PPI images (15:21 UTC) of Tropical Storm Emily. Note storm approach from SE to NW due to CCW rotation of Emily from south. Images created using CSU VCHILL and Google Earth

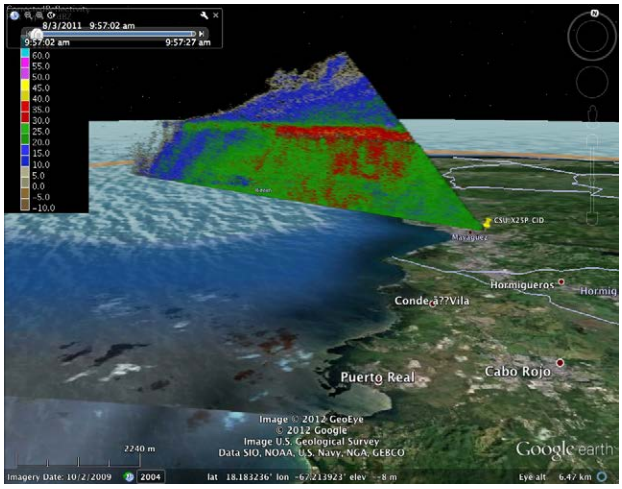

(a) CdBZ, RHI at AZ=303°

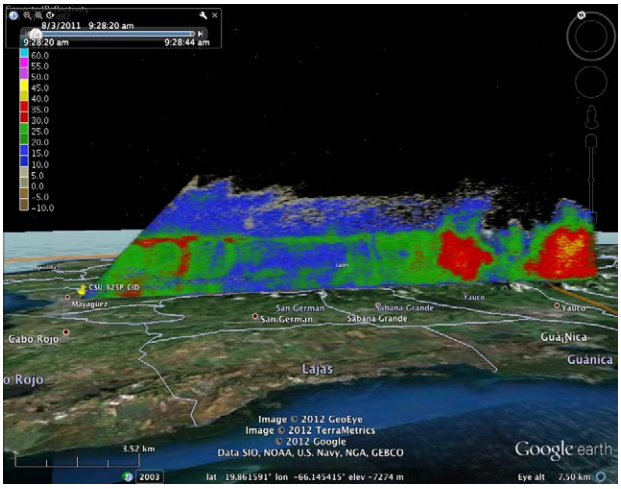

(b) CdBZ, RHI at AZ=118°

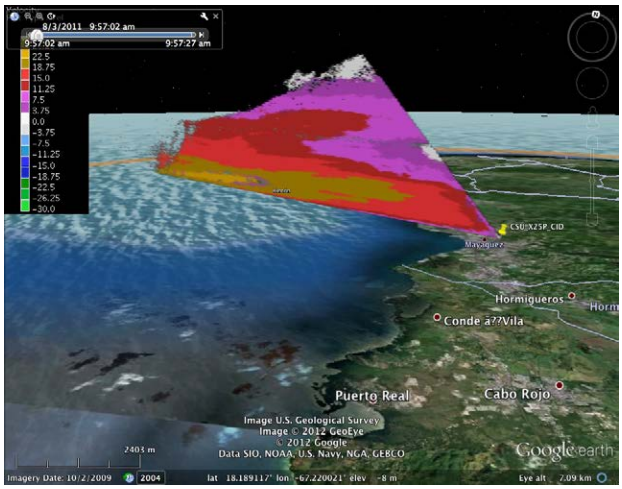

(c) Max. Outbound Velocity= 24 m/s

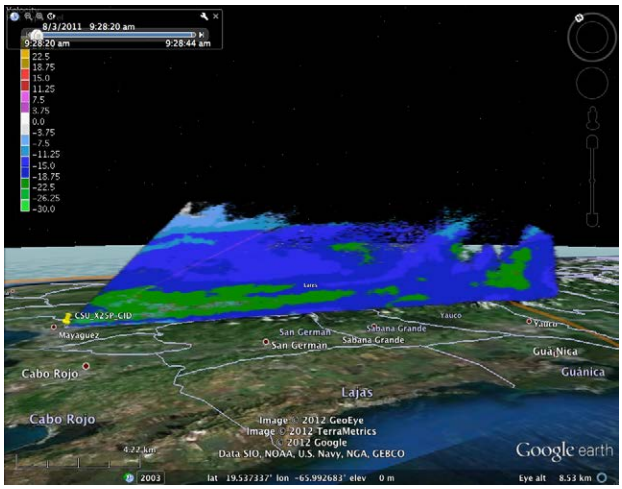

(d) Max. Inbound Velocity= -26 m/s

Figure 4.17: Tropical Storm Emily, RHI scans through Inbound and Outbound rain band on 2011-08-03 at 15:57 UTC (a & c) and 15:28 UTC (b & d). For reference, cloud tops at 8-10 km; melting layer at 4.5-5 km. Images created using CSU VCHILL and Google Earth

and the many east coast cities affected by the strong winds and heavy rain.

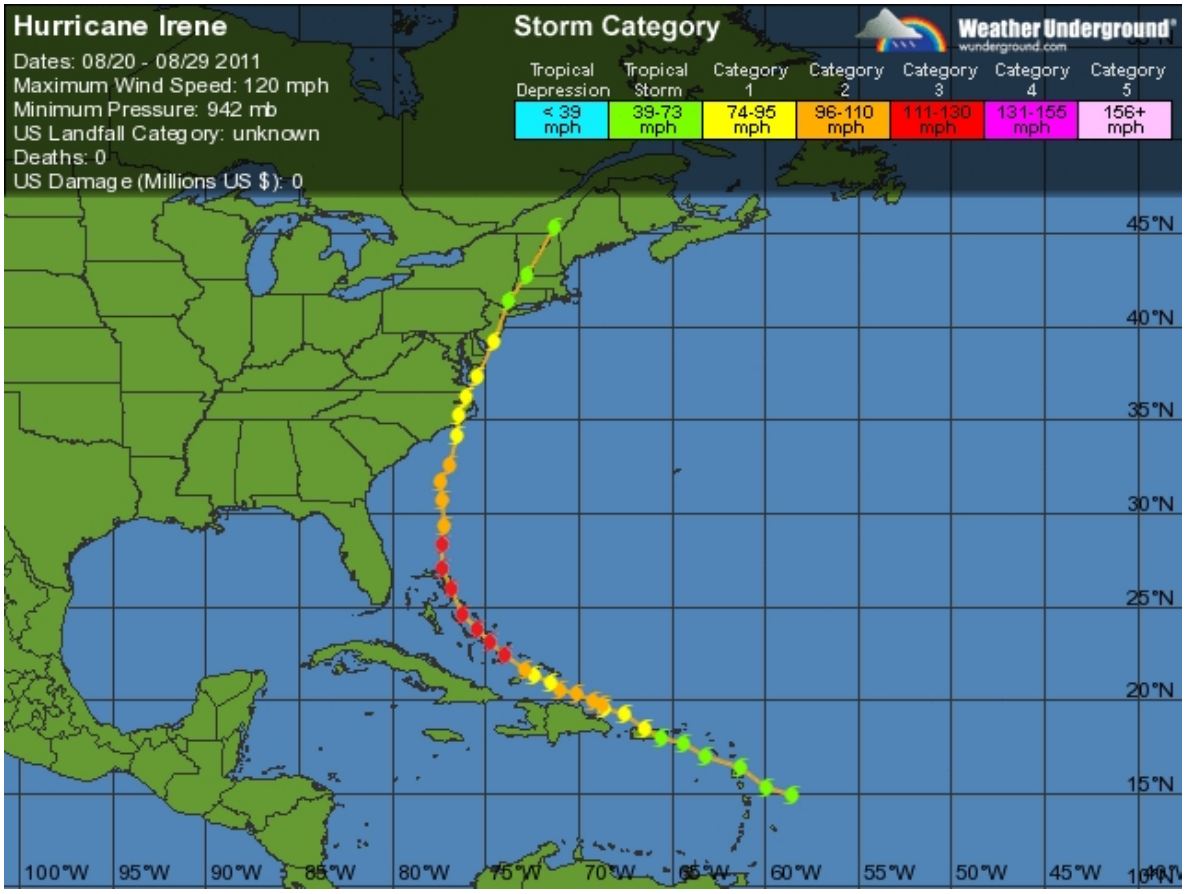

Figure 4.18: Hurricane Irene storm track (using Weather Underground)

Early on August 22, Tropical Storm Irene made landfall on the southeastern coast of Puerto Rico where it continued to track northwest across the island, all while strengthening to hurricane force winds as it returned to water. At approximately 09:00 UTC, Irene was classified as a category 1 hurricane. Figure 4.19, shows satellite, TJUA, TDWR, and CSU-X25P radar reflectivity and velocity images depicting the evolution of Irene. In the MODIS satellite image, the organization of the storm is evident as it tracks towards Puerto Rico on 20110821-1745 UTC. About 8 hours later, TJUA radar captured reflectivities in the 35-45 dBZ range as Irene was on its final approach toward the island. In this and subsequent figures, corrected reflectivity and Doppler velocity PPI scans from CSU-X25P, at Elevations of 4°, are presented at hourly intervals starting at 20110822-07:09 UTC through 20110823-

02:08 UTC. This particular PPI scan angle was selected based on minimal ground clutter that might otherwise block large sectors in the southeastern quadrant.

At approximately 20110822-03:30 UTC, the TJUA radar went offline for the next nine hours, due to power losses experienced by over 800,000 households to the eastern half of the island. With the NEXRAD radar down, the TDWR radar located in San Juan was then used to track Irene during CSU-X25P operations. Around the time of the power outages, remote operations from within the island were no longer possible, and thus the author assumed remote operations from his home in Colorado. This was possible due to proper planning of the infrastructure, ensuring ample backup power and internet access to the R&D building, on the UPRM campus.

During this evolution observed by CSU-X25P, we can see that during the first four hours, from 07:09-10:08 UTC, light rain bands came from the northeast and gradually shifted to northwesterly winds. An assumption of the general storm direction can be made based on the zero-Doppler transition region (white color), where the relative velocity here is orthogonal to the radial direction of the radar, resulting in near zero velocites. Looking at the orthogonal direction to the zero-Doppler transition, the general direction of the rain bands can be determined based on the inbound to outbound velocities from the observed PPIs.

In Figure 4.20, the transition in the direction of light rain bands shifts from northwesterly to southwesterly, from 11:05-14:10 UTC. During this time, Irene's eye was tracking westward, almost parallel the northern coast of the island. Measured Doppler velocities were in the 18 m/s (40 mph) range, but the eye was still over 80 km away from the radar. As the eye travelled past the west coast, the measured velocities saw an increase to the 24 m/s (54 mph) range, as seen in Figure 4.21. A notable shift from southwesterly to near southerly, in the relative wind velocities of the rain band direction can be seen over the next eight hours from 15:04-22:11 UTC, in Figures 4.21 and 4.22. In Figure 4.23, we continue to see the rain band direction shift from southerly to slightly southeasterly as the eye of Hurricane Irene traveled north of the Dominican Republic, while moisture was continually pulled toward its vortex.

The CSU-X25P radar node proved to be robust and operated under high sustained wind

velocities during several heavy precipitation events, to include Tropical Storm Emily and Hurricane Irene. It was also demonstrated that the hardware and software designs met the challenge of operating in the tropical environment on the western coast of Puerto Rico. It was the author's experience that the CSU-UPRM collaboration was successful with respect to preparedness for future deployment and operations of the TropiNet radar network.

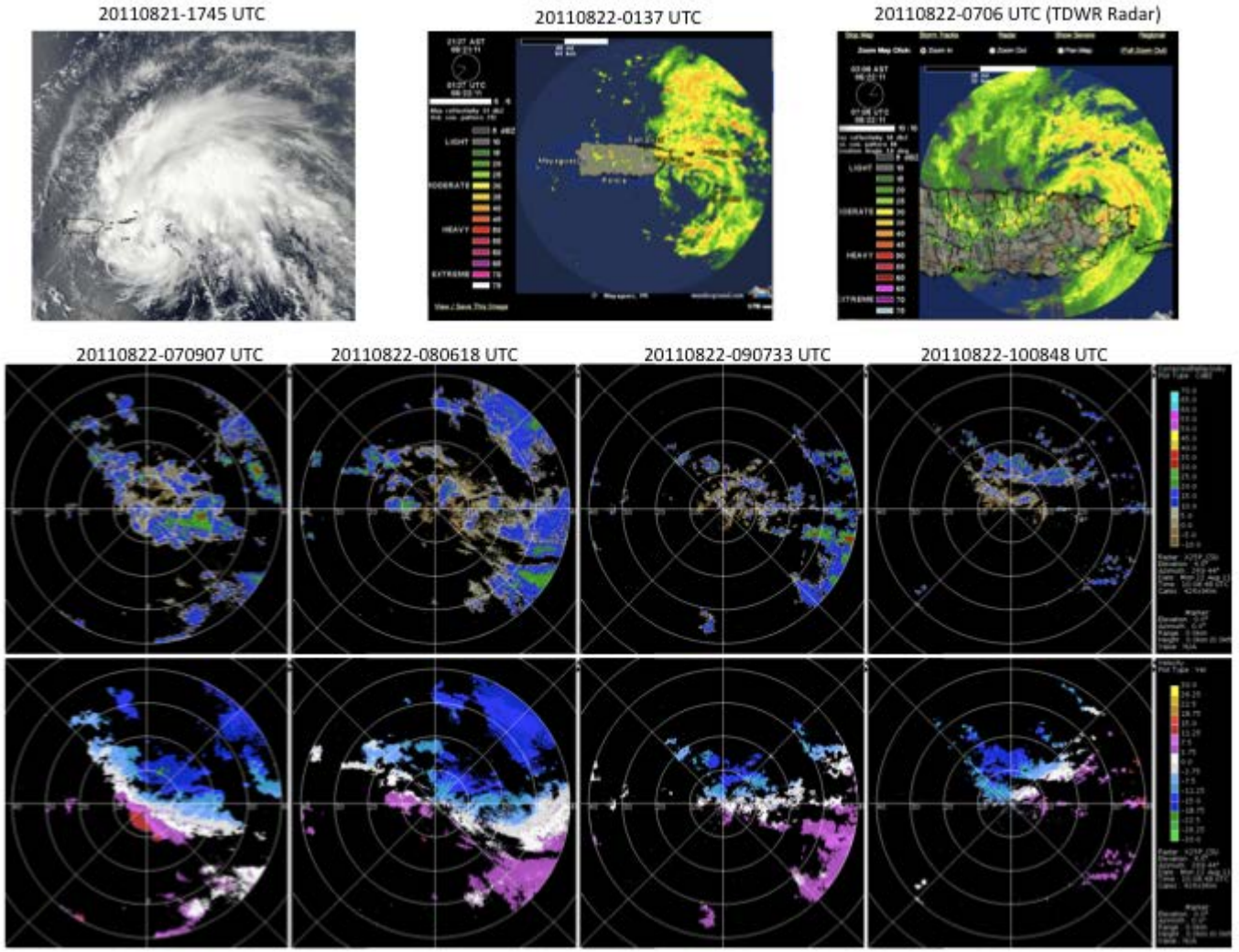

Figure 4.19: MODIS, TJUA, & CSU-X25P CdBZ & v_D PPI images of Hurricane Irene. Note shift from northeasterly to northwesterly direction in rain bands. MODIS image source: NASA/GSFC, MODIS Rapid Response. TJUA image source: Weather Underground. CSU-X25P images created with CSU VCHILL.

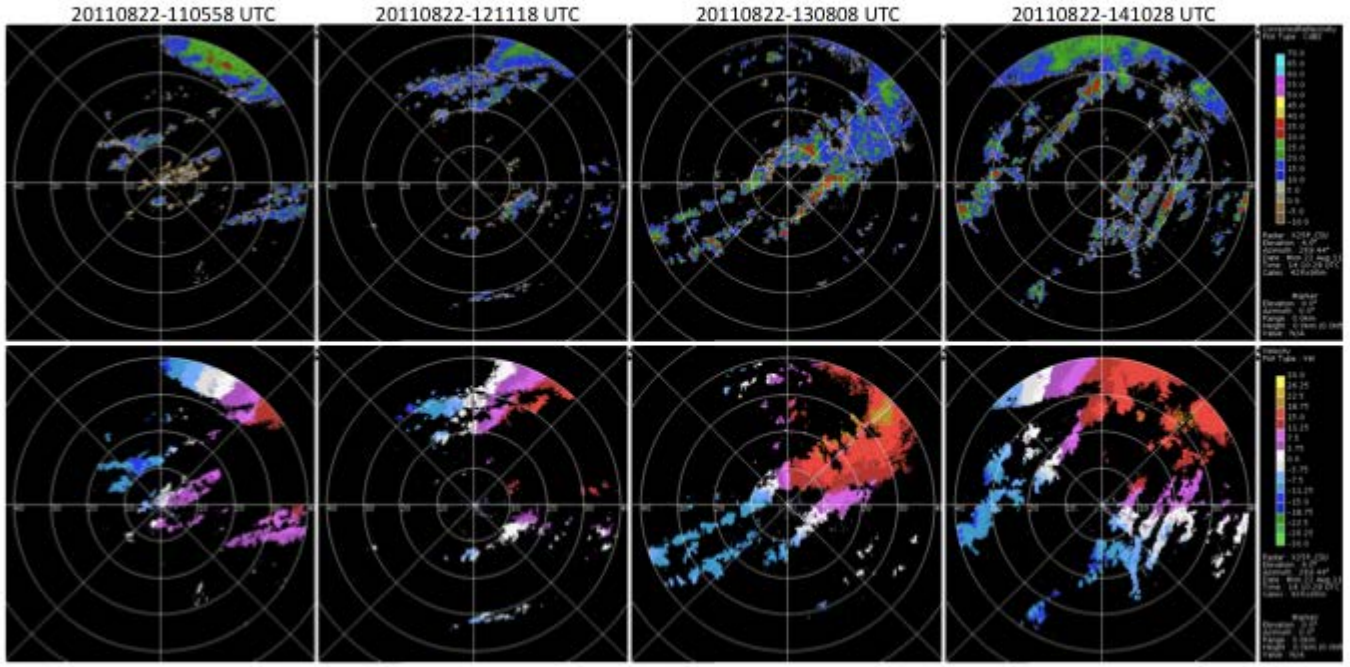

Figure 4.20: CSU-X25P CdBZ & v_D PPI images of Hurricane Irene (created with CSU VCHILL). Note shift from northwesterly to southwesterly direction in rain bands.

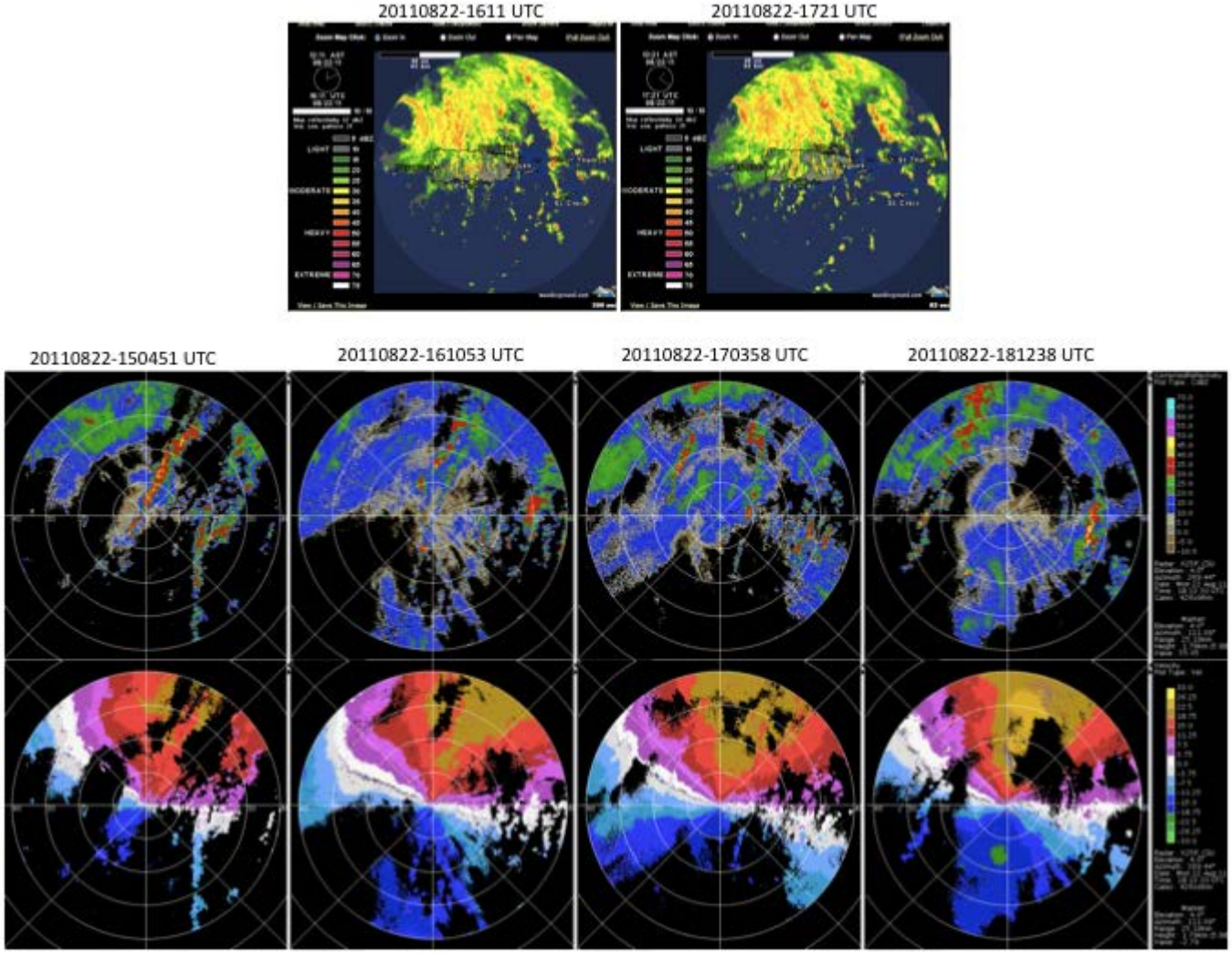

Figure 4.21: TJUA (dBZ) & CSU-X25P (CdBZ & v_D) images of Hurricane Irene. Note eye located NW of island, the southwesterly direction in rain bands and the significant increase in velocities to 18-25 m/s. TJUA image source: Weather Underground. CSU-X25P images created with CSU VCHILL

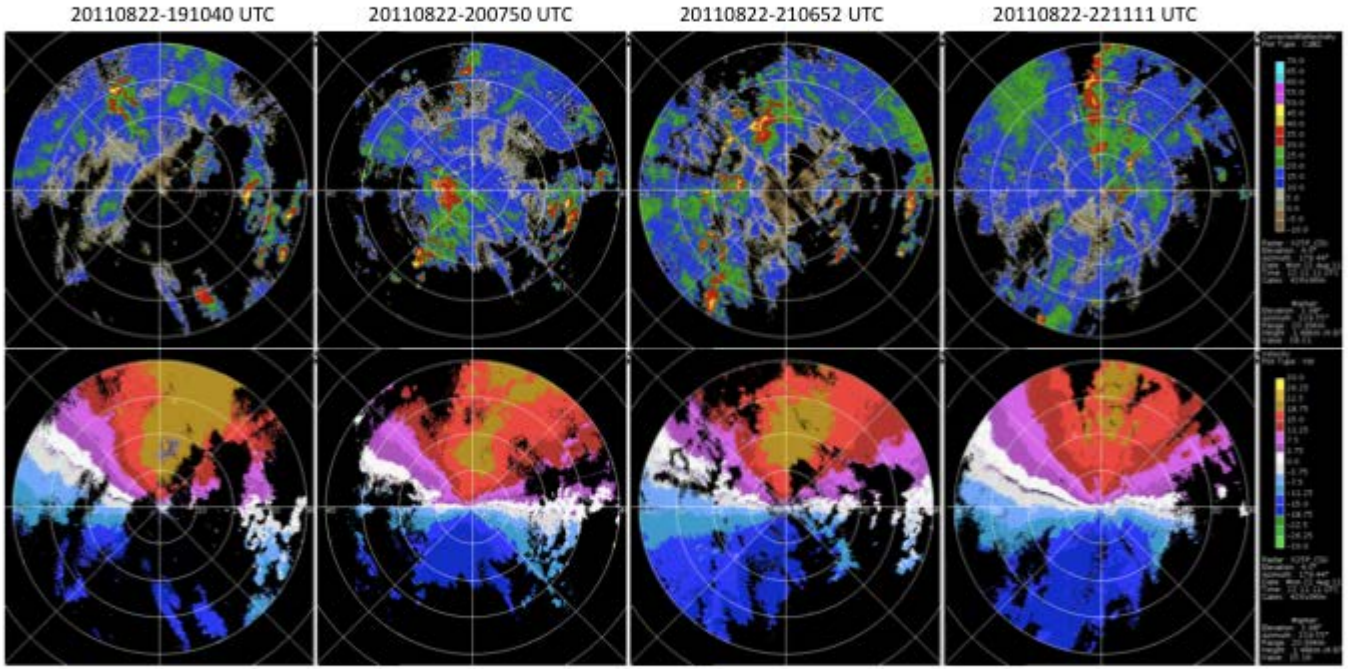

Figure 4.22: CSU-X25P CdBZ & v_D PPI images of Hurricane Irene (created with CSU VCHILL). Note the southwesterly to southerly shift in direction, and sustained velocities in the 18-22 m/s range.

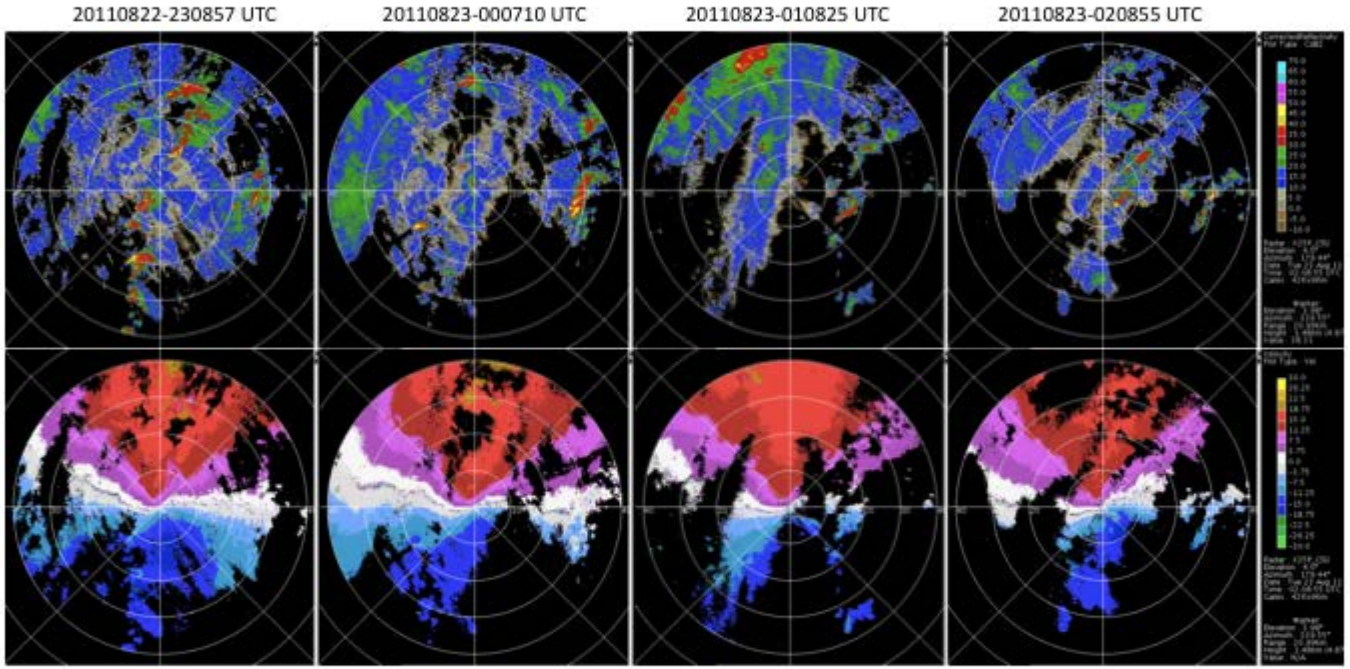

Figure 4.23: CSU-X25P CdBZ & v_D PPI images of Hurricane Irene (created with CSU VCHILL). Note the southerly to southeasterly shift in direction, and sustained velocities in the 15-18 m/s range.

CHAPTER 5

Summary and Conclusions

This Thesis has described the development and validation of an X-band polarimetric Doppler weather radar, that was the first dual polarization radar to be deployed in Puerto Rico, to observe the lower troposphere in a tropical environment. The overall radar system was described, providing detailed descriptions of the major functional blocks to include: the transceiver, data acquisition system, antenna, and antenna positioner. Key modifications made to upgrade a SCR-584 pedestal with modern motors, position control, and a gigabit Ethernet rotary joint were presented and documented. Calibration procedures were separately performed on the transmitter, analog receiver, and digital receiver, while a metallic sphere calibration provided an end to end radar system calibration.

An overview of the signal processing techniques used to calculate the Doppler spectral moments from an incoherent magnetron transmitter was presented. The calculated radar parameters include the Doppler velocity, effective reflectivity, differential reflectivity, differential propagation phase, and specific differential phase. In addition, a description of the real-time clutter filtering procedure used to mitigate unwanted return echoes from ground targets was included.

Results from the system validation of the CSU-X25P with the CSU-CHILL S-band radar provided good agreement in the calculated radar parameters. The deployment of CSU-X25P, the initial test node for the TropiNet radar network, to the western coast of Puerto Rico is documented. This deployment served as a platform to strengthen the collaboration between CSU and UPRM, and equally important, to test the robustness of the TropiNet infrastructure.

Having successfully operated during Hurricane Irene and Tropical Storm Emily in 2011, the CSU-X25P has proven it can function, as designed, under adverse environmental conditions in the tropics. These and other cases were presented with example PPI and RHI

scan images that testify to the capabilities of this X-band polarimetric Doppler weather radar.

REFERENCES

[1] D. Bikel, "Circle Plot KML File Generator, Federal Communications Commission webpage," September 2011. ix, 47

[2] F. Junyent, V. Chandrasekaran, D. J. McLaughlin, E. Insanic, and N. Bharadwaj, "The CASA Integrated Project 1 Networked Radar System," *Journal of Atmospheric and Oceanic Technology*, vol. 27, pp. 61–78, January 2010. 1

[3] F. Junyent, *Networked Weather Radar System Using Coherent on Receive Technology*. Dissertation, University of Massachusetts Amherst, May 2007. 1

[4] M. B. Galvez, J. G. Colom, V. Chandrasekaran, F. Junyent, S. Cruz-Pol, and R. Rodriguez, "Salient Features of Radar Nodes in the Puerto Rico Tropical Weather Testbed," in *Proc. IGARSS*, IEEE, 2009. 1, 45

[5] F. Junyent, V. Chandrasekaran, D. McLaughlin, S. Frasier, E. Insanic, R. Ahmed, N. Bharadwaj, E. Knapp, L. Krnan, and R. Tessier, "Salient Features of Radar Nodes of The First Generation NetRad System," in *Proc. IGARSS '05*, pp. 420–423, IEEE, 2005. 6

[6] R. Khasgiwale, L. Krnan, A. Perinkulam, and R. Tessier, "Reconfigurable Data Acquisition System for Weather Radar Applications," in *Proc. of International Midwest Symposium on Circuits and Systems, Cincinnati, Ohio*, 2005. 10

[7] D. Fink, "The SCR-584 Radar," *Electronics magazine*, November 1945 and February 1946. 11

[8] V. Bringi and V. Chandrasekaran, *Polarimetric Doppler Weather Radar: Principles and Applications*. Cambridge University Press., 2001. 23, 25, 30, 32, 35

[9] Y. Wang and V. Chandrasekar, "Performance of Dual-polarization Radar Measurement in Hybrid Mode for Precipitation," in *IEEE Transactions on Geoscience and Remote Sensing*, vol. 7, pp. 5084–5087, IEEE, July 2005. 24

[10] Y. Wang, V. Chandrasekar, and V. Bringi, "Characterization and Evaluation of Hybrid Polarization Observation of Precipitation," in *J. Atmos. Oceanic Technol.*, vol. 23, pp. 552–572, April 2006. 24

[11] Y. Wang and V. Chandrasekar, "Polarization Isolation Requirements for Linear Dual-Polarization Weather Radar in Simultaneous Transmission Mode of Operation," in *IEEE Transactions on Geoscience and Remote Sensing*, vol. 44, pp. 2019–2028, IEEE, August 2006. 24

[12] R. J. Doviak and D. S. Zrnic, *Doppler Radar and Weather Observations*. Academic Press Inc., 2nd ed., 1993. 29, 32

[13] N. Bharadwaj and V. Chandrasekaran, "Waveform Design for CASA X-Band Radars," in *AMS 32nd Conference on Radar Meteorology*, 2005. 31, 36

[14] N. Bharadwaj and V. Chandrasekaran, "Waveform Design Considerations for CASA Radar Network," in *ERAD*, 2006. 31, 36

[15] E. Gorgucci, G. Scarchilli, and V. Chandrasekar, "A procedure to calibrate multiparameter weather radar using properties of the rain medium," in *IEEE Transactions of Geoscience and Remote Sensing*, vol. 37, pp. 269–276, 1999. 32

[16] S. Y. Matrosov, R. A. Kropfli, R. F. Reinking, and B. E. Martner, "Prospects for Measuring Rainfall Using Propagation Differential Phase in X- and Ka-Radar Bands," in *Journal of Applied Meteorology*, vol. 38, pp. 766–776, 1999. 35

[17] Y. Liu, V. Bringi, and M. Maki, "Improved Rain Attenuation Correction Algorithms for Radar Reflectivity and Differential Reflectivity with Adaptation to Drop Shape Model Variation," in *IEEE Transactions of Geoscience and Remote Sensing*, pp. 1910–1913, 2006. 38

[18] Y. Wang and V. Chandrasekar, "Algorithm for Estimation of the Specific Differential Phase," in *J. Atmos. Oceanic Technol.*, vol. 26, pp. 2565–2578, 2009. 38

[19] S.-G. Park, M. Maki, K. Iwanami, V. Bringi, and V. Chandrasekar, "Correction of Radar Reflectivity and Differential Reflectivity for Rain Attenuation at X Band. Part II: Evaluation and Application," in *J. Atmos. Oceanic Technol.*, vol. 22, pp. 1633–1655, 2005. 41

[20] S.-G. Park, V. Bringi, V. Chandrasekar, M. Maki, and K. Iwanami, "Correction of Radar Reflectivity and Differential Reflectivity for Rain Attenuation at X Band. Part I: Theoretical and Empirical Basis," in *J. Atmos. Oceanic Technol.*, vol. 22, pp. 1621–1632, 2005. 41

[21] M. B. Galvez, J. G. Colom, V. Chandrasekaran, F. Junyent, S. Cruz-Pol, R. A. R. Solis, and K.-R. Kwon, "First Observations of an X-Band Dual Polarization Doppler Weather Radar on the Western Coast of Puerto Rico," in *Proc. IGARSS*, IEEE, 2011. 51

APPENDIX A

Antenna Positioner Assemblies

Revision History

0.1 - Initial pre-release
0.2 - Checked by DAB, FJ, JG. Fixed minor mistakes.
0.3 - Removed optic fiber components due to lack of space on the board, added UMAC variant to build list, filled in refdes for build variants

1.0 - Board rev 1. Includes microwave switch assembly components, DAC SHDN pin tied to +5V instead of GND

1.1 - Change FB8-11 to use component MZA3216Y102B instead of DLP31

Build Variants

UMAC chassis compatible

NOUMAC - No UMAC compatibility

Do not populate:
P1

UMAC - Draw power from UMAC

Do not populate:
FL1, F13, D28, U27, C46

The default configuration is NOUMAC, NOPAR

Parallel I/O

NOPAR - No Parallel I/O

Do not populate:
U18-21, C39-42, J13, J14

PARIO - With Parallel I/O

Do not populate:

Title: ***Pedestal Interface - Revision History***		*CSU-CHILL* *30750 Weld County Road 45* *Greeley, CO 80631* Colorado State University	Engineer: JG
Size: Letter	Number: wibex_pi_1	Revision: 1.1	Drawn By: JG
Date: 5/28/2009	Time: 9:25:34 AM	Sheet 1 of 8	
File: C:\Documents and Settings\jgeorge\My Documents\pcb\angleconvert\ac_revision.SchDoc			

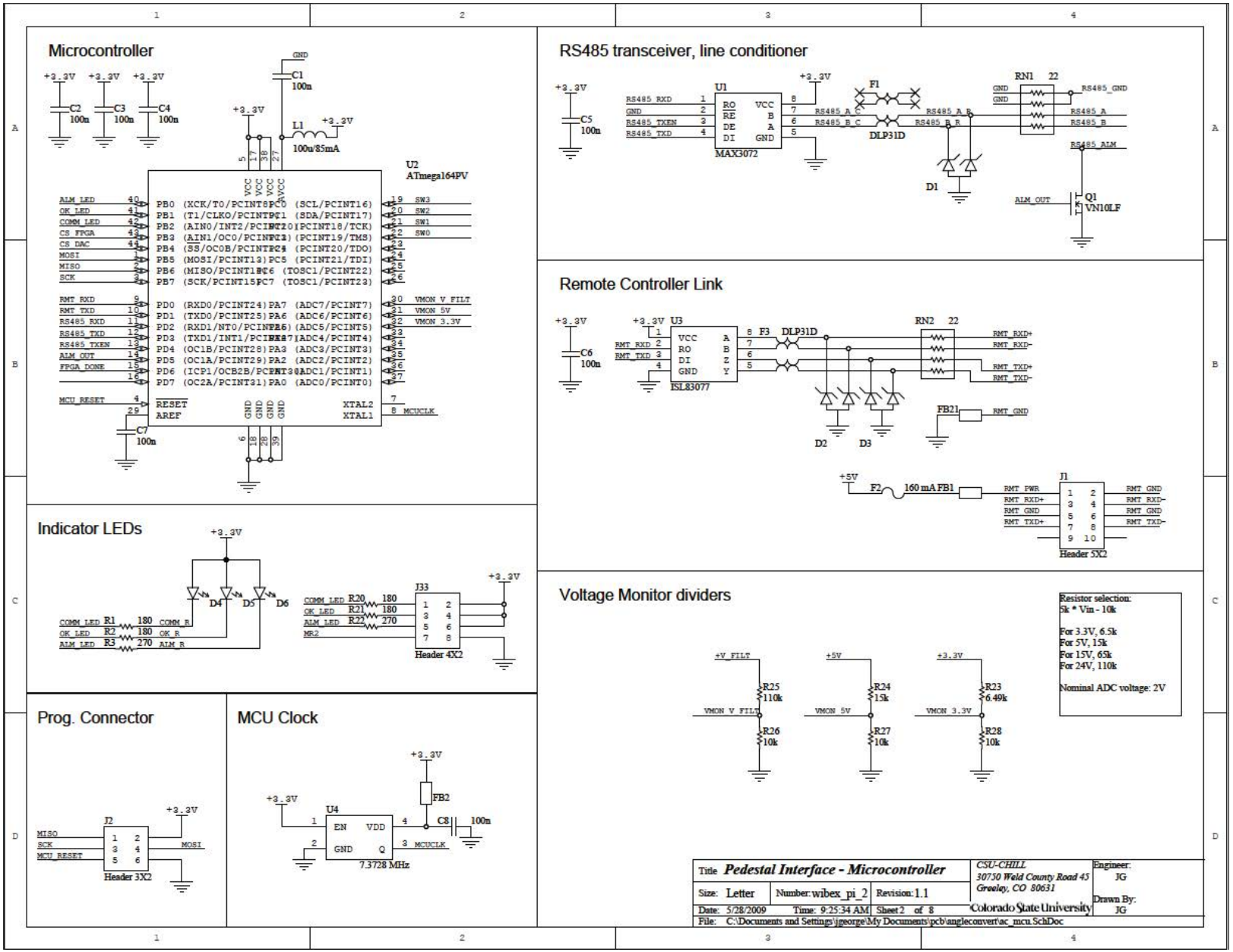
Microcontroller
U2
ATmega164PV
RESET
AREF
XTAL2
XTAL1
MCUCLK
RS485 transceiver, line conditioner
U1
MAX3072
DLP31D
F1
D1
Q1
VN10LF
RS485_GND
RS485_A
RS485_B
RS485_ALM
Remote Controller Link
U3
ISL83077
DLP31D
F3
D2
D3
FB21
RMT_GND
F2
160 mA FB1
J1
Header 5X2
Indicator LEDs
D4
D5
D6
J33
Header 4X2
Voltage Monitor dividers
Resistor selection:
5k * Vin - 10k
For 3.3V, 6.5k
For 5V, 15k
For 15V, 65k
For 24V, 110k
Nominal ADC voltage: 2V
Prog. Connector
J2
Header 3X2
MCU Clock
U4
FB2
7.3728 MHz
Title Pedestal Interface - Microcontroller
CSU-CHILL
30750 Weld County Road 45
Greeley, CO 80631
Colorado State University
Size: Letter
Number: wibex_pi_2
Revision: 1.1
Date: 5/28/2009
Time: 9:25:34 AM
Sheet 2 of 8
File: C:\Documents and Settings\jgeorge\My Documents\pcb\angleconvert\ac_mcu.SchDoc
Engineer: JG
Drawn By: JG

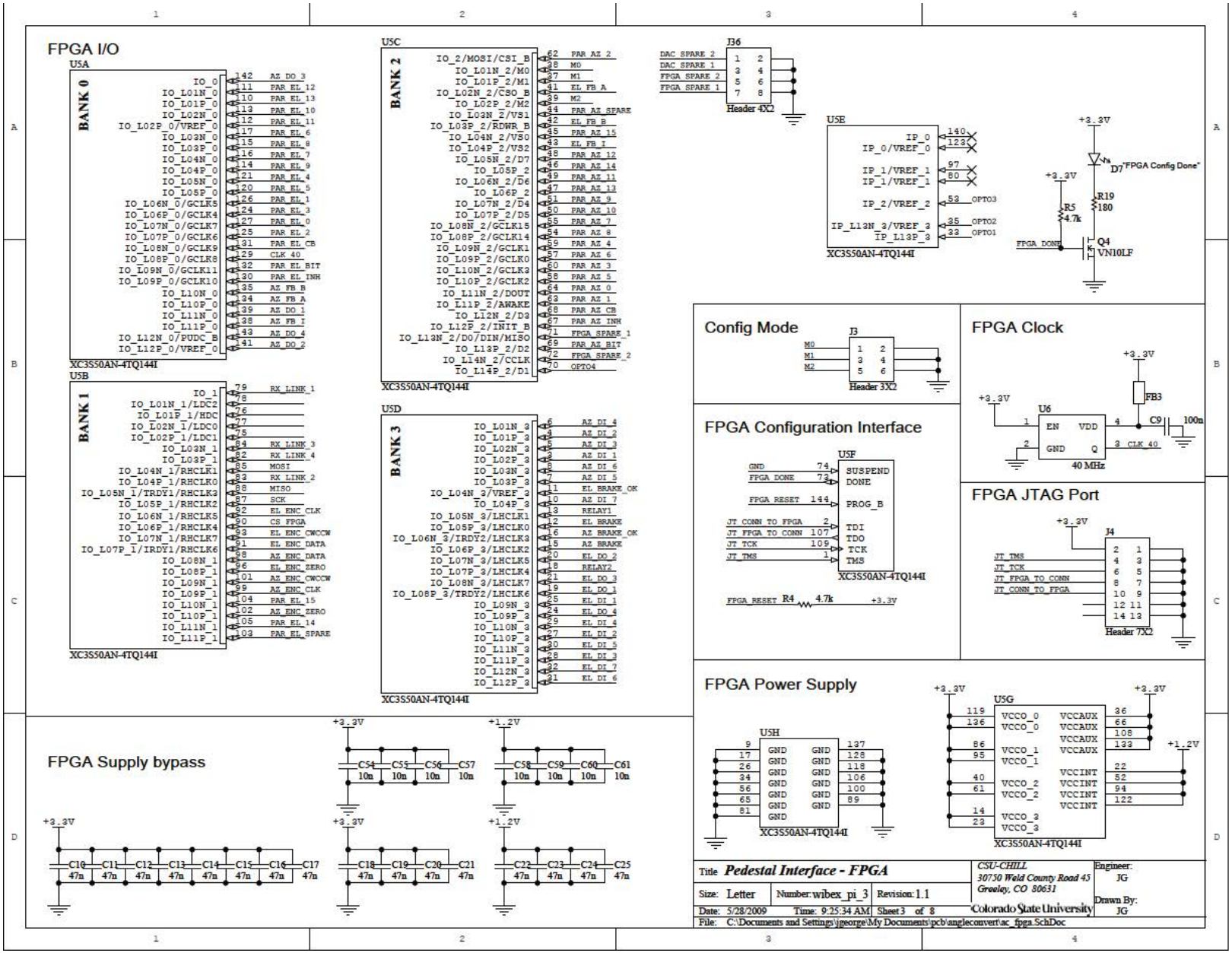
FPGA I/O
U5A
BANK 0
XC3S50AN-4TQ144I
U5B
BANK 1
XC3S50AN-4TQ144I
U5C
BANK 2
XC3S50AN-4TQ144I
U5D
BANK 3
XC3S50AN-4TQ144I
J36
Header 4X2
U5E
XC3S50AN-4TQ144I
D7 "FPGA Config Done"
Q4 VN10LF
Config Mode
J3
Header 3X2
FPGA Clock
U6
40 MHz
FPGA Configuration Interface
U5F
XC3S50AN-4TQ144I
FPGA JTAG Port
J4
Header 7X2
FPGA Power Supply
U5H
XC3S50AN-4TQ144I
U5G
XC3S50AN-4TQ144I
FPGA Supply bypass
Title Pedestal Interface - FPGA
Size: Letter
Number: wibex_pi_3
Revision: 1.1
Date: 5/28/2009
Time: 9:25:34 AM
Sheet 3 of 8
File: C:\Documents and Settings\jgeorge\My Documents\pcb\angleconvert\ac_fpga.SchDoc
CSU-CHILL
30750 Weld County Road 45
Greeley, CO 80631
Colorado State University
Engineer: JG
Drawn By: JG

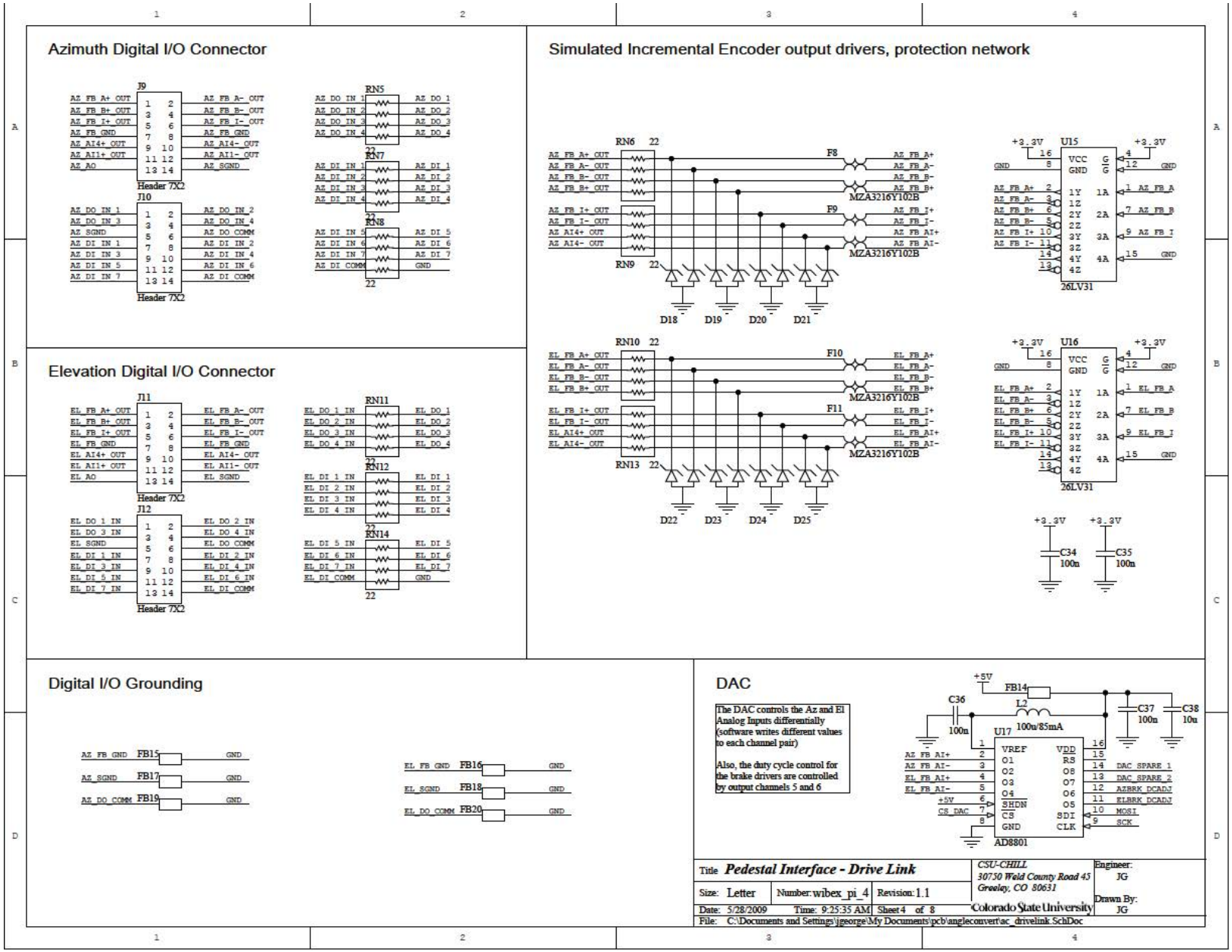
Azimuth Digital I/O Connector
Simulated Incremental Encoder output drivers, protection network
Elevation Digital I/O Connector
Digital I/O Grounding
DAC
The DAC controls the Az and El Analog Inputs differentially (software writes different values to each channel pair)
Also, the duty cycle control for the brake drivers are controlled by output channels 5 and 6
Title Pedestal Interface - Drive Link
CSU-CHILL
30750 Weld County Road 45
Greeley, CO 80631
Colorado State University
Engineer: JG
Drawn By: JG
Size: Letter
Number: wibex_pi_4
Revision: 1.1
Date: 5/28/2009
Time: 9:25:35 AM
Sheet 4 of 8
File: C:\Documents and Settings\jgeorge\My Documents\pcb\angleconvert\ac_drivelink.SchDoc

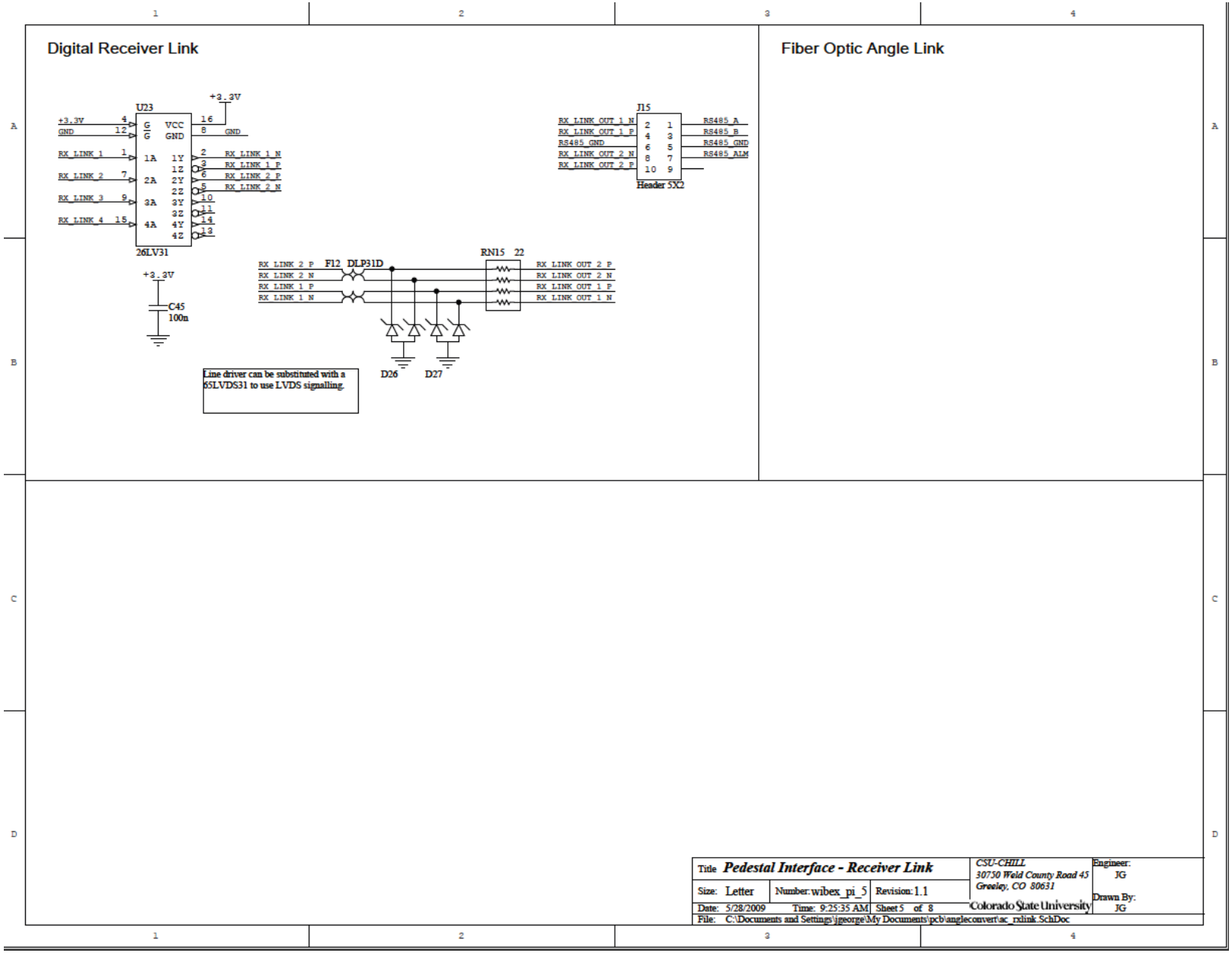
Digital Receiver Link
Fiber Optic Angle Link
U23
26LV31
+3.3V
GND
RX_LINK_1
RX_LINK_2
RX_LINK_3
RX_LINK_4
RX_LINK_1_N
RX_LINK_1_P
RX_LINK_2_P
RX_LINK_2_N
C45
100n
F12 DLP31D
D26
D27
RN15 22
J15
Header 5X2
RS485_A
RS485_B
RS485_GND
RS485_ALM
Line driver can be substituted with a 65LVDS31 to use LVDS signalling.
Title Pedestal Interface - Receiver Link
Size: Letter
Number: wibex_pi_5
Revision: 1.1
Date: 5/28/2009
Time: 9:25:35 AM
Sheet 5 of 8
File: C:\Documents and Settings\jgeorge\My Documents\pcb\angleconvert\ac_rxlink.SchDoc
CSU-CHILL
30750 Weld County Road 45
Greeley, CO 80631
Colorado State University
Engineer: JG
Drawn By: JG

Parallel Angle Input - Azimuth

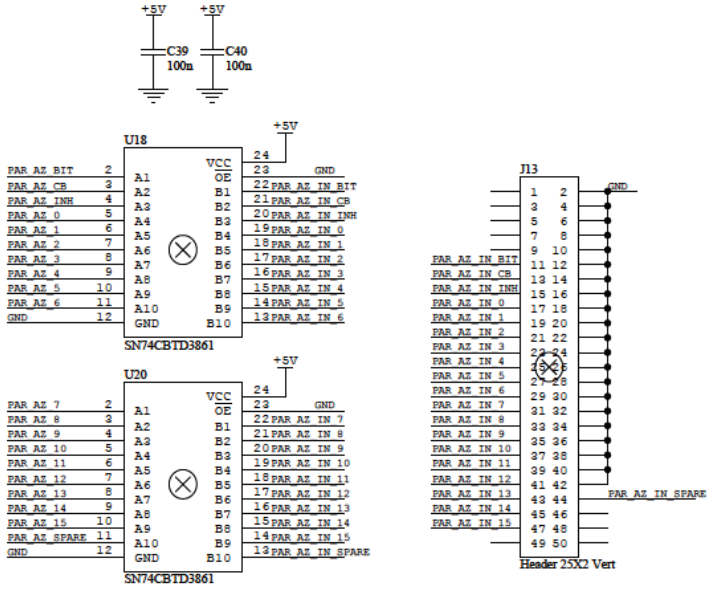

Parallel Angle Input - Elevation

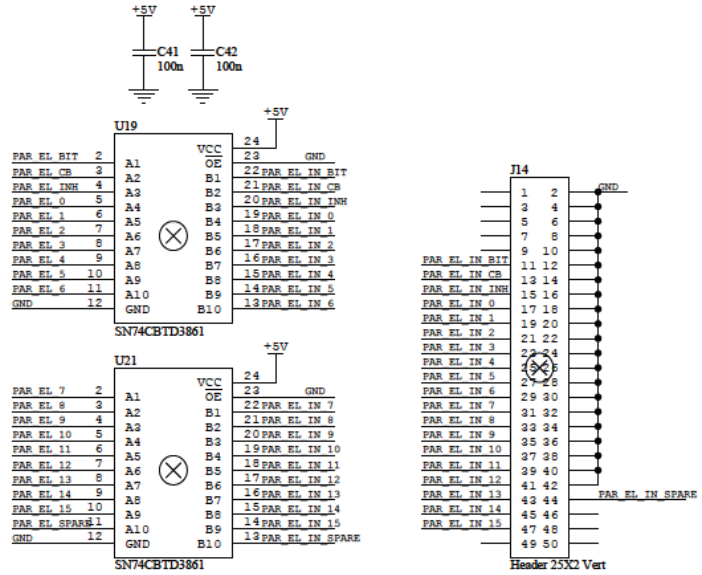

Title: ***Pedestal Interface - Parallel Interface***		*CSU-CHILL* *30750 Weld County Road 45* *Greeley, CO 80631*	Engineer: JG
Size: Letter	Number: wibex_pi_6	Revision: 1.1	Drawn By: JG
Date: 5/28/2009	Time: 9:25:35 AM	Sheet 6 of 8	Colorado State University
File: C:\Documents and Settings\jgeorge\My Documents\pcb\angleconvert\ac_parenc.SchDoc			

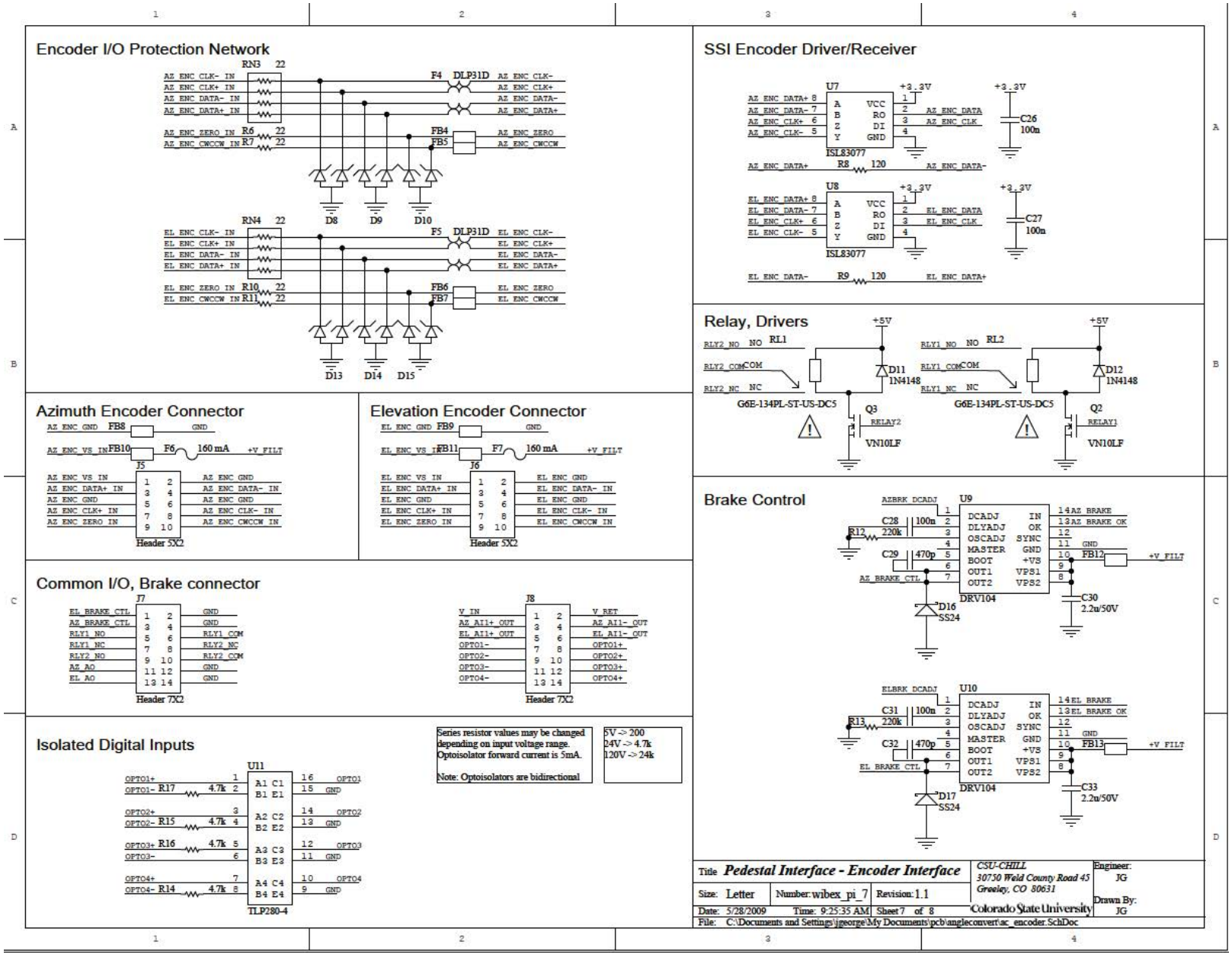
Encoder I/O Protection Network
RN3 22
AZ_ENC_CLK- IN
AZ_ENC_CLK+ IN
AZ_ENC_DATA- IN
AZ_ENC_DATA+ IN
AZ_ENC_ZERO_IN R6 22
AZ_ENC_CWCCW_IN R7 22
F4 DLP31D
FB4
FB5
AZ_ENC_CLK-
AZ_ENC_CLK+
AZ_ENC_DATA-
AZ_ENC_DATA+
AZ_ENC_ZERO
AZ_ENC_CWCCW
D8 D9 D10
RN4 22
EL_ENC_CLK- IN
EL_ENC_CLK+ IN
EL_ENC_DATA- IN
EL_ENC_DATA+ IN
EL_ENC_ZERO_IN R10 22
EL_ENC_CWCCW_IN R11 22
F5 DLP31D
FB6
FB7
EL_ENC_CLK-
EL_ENC_CLK+
EL_ENC_DATA-
EL_ENC_DATA+
EL_ENC_ZERO
EL_ENC_CWCCW
D13 D14 D15
SSI Encoder Driver/Receiver
U7
AZ_ENC_DATA+ 8
AZ_ENC_DATA- 7
AZ_ENC_CLK+ 6
AZ_ENC_CLK- 5
A B Z Y
VCC RO DI GND
1 2 3 4
AZ_ENC_DATA
AZ_ENC_CLK
ISL83077
+3.3V
C26 100n
AZ_ENC_DATA+ R8 120 AZ_ENC_DATA-
U8
EL_ENC_DATA+ 8
EL_ENC_DATA- 7
EL_ENC_CLK+ 6
EL_ENC_CLK- 5
EL_ENC_DATA
EL_ENC_CLK
ISL83077
C27 100n
EL_ENC_DATA- R9 120 EL_ENC_DATA+
Relay, Drivers
+5V
RLY2_NO NO RL1
RLY2_COM COM
RLY2_NC NC
D11 1N4148
G6E-134PL-ST-US-DC5
Q3 RELAY2 VN10LF
RLY1_NO NO RL2
RLY1_COM COM
RLY1_NC NC
D12 1N4148
G6E-134PL-ST-US-DC5
Q2 RELAY1 VN10LF
Azimuth Encoder Connector
AZ_ENC_GND FB8 GND
AZ_ENC_VS_IN FB10 F6 160 mA +V_FILT
J5
AZ_ENC_VS_IN
AZ_ENC_DATA+ IN
AZ_ENC_GND
AZ_ENC_CLK+ IN
AZ_ENC_ZERO_IN
AZ_ENC_GND
AZ_ENC_DATA- IN
AZ_ENC_GND
AZ_ENC_CLK- IN
AZ_ENC_CWCCW_IN
Header 5X2
Elevation Encoder Connector
EL_ENC_GND FB9 GND
EL_ENC_VS_IN FB11 F7 160 mA +V_FILT
J6
EL_ENC_VS_IN
EL_ENC_DATA+ IN
EL_ENC_GND
EL_ENC_CLK+ IN
EL_ENC_ZERO_IN
EL_ENC_GND
EL_ENC_DATA- IN
EL_ENC_GND
EL_ENC_CLK- IN
EL_ENC_CWCCW_IN
Header 5X2
Common I/O, Brake connector
J7
EL_BRAKE_CTL
AZ_BRAKE_CTL
RLY1_NO
RLY1_NC
RLY2_NO
AZ_AO
EL_AO
GND
GND
RLY1_COM
RLY2_NC
RLY2_COM
GND
GND
Header 7X2
J8
V_IN
AZ_AI1+_OUT
EL_AI1+_OUT
OPTO1-
OPTO2-
OPTO3-
OPTO4-
V_RET
AZ_AI1-_OUT
EL_AI1-_OUT
OPTO1+
OPTO2+
OPTO3+
OPTO4+
Header 7X2
Isolated Digital Inputs
U11
OPTO1+ 1
OPTO1- R17 4.7k 2
OPTO2+ 3
OPTO2- R15 4.7k 4
OPTO3+ R16 4.7k 5
OPTO3- 6
OPTO4+ 7
OPTO4- R14 4.7k 8
A1 C1 B1 E1
A2 C2 B2 E2
A3 C3 B3 E3
A4 C4 B4 E4
16 OPTO1
15 GND
14 OPTO2
13 GND
12 OPTO3
11 GND
10 OPTO4
9 GND
TLP280-4
Series resistor values may be changed depending on input voltage range. Optoisolator forward current is 5mA.
Note: Optoisolators are bidirectional
5V -> 200
24V -> 4.7k
120V -> 24k
Brake Control
AZBRK_DCADJ
U9
C28 100n
R12 220k
C29 470p
AZ_BRAKE_CTL
DCADJ IN
DLYADJ OK
OSCADJ SYNC
MASTER GND
BOOT +VS
OUT1 VPS1
OUT2 VPS2
DRV104
AZ_BRAKE
AZ_BRAKE_OK
GND
FB12
+V_FILT
C30 2.2u/50V
D16 SS24
ELBRK_DCADJ
U10
C31 100n
R13 220k
C32 470p
EL_BRAKE_CTL
DRV104
EL_BRAKE
EL_BRAKE_OK
GND
FB13
+V_FILT
C33 2.2u/50V
D17 SS24
Title Pedestal Interface - Encoder Interface
Size: Letter
Number: wibex_pi_7
Revision: 1.1
Date: 5/28/2009
Time: 9:25:35 AM
Sheet 7 of 8
File: C:\Documents and Settings\jgeorge\My Documents\pcb\angleconvert\ac_encoder.SchDoc
CSU-CHILL
30750 Weld County Road 45
Greeley, CO 80631
Colorado State University
Engineer: JG
Drawn By: JG

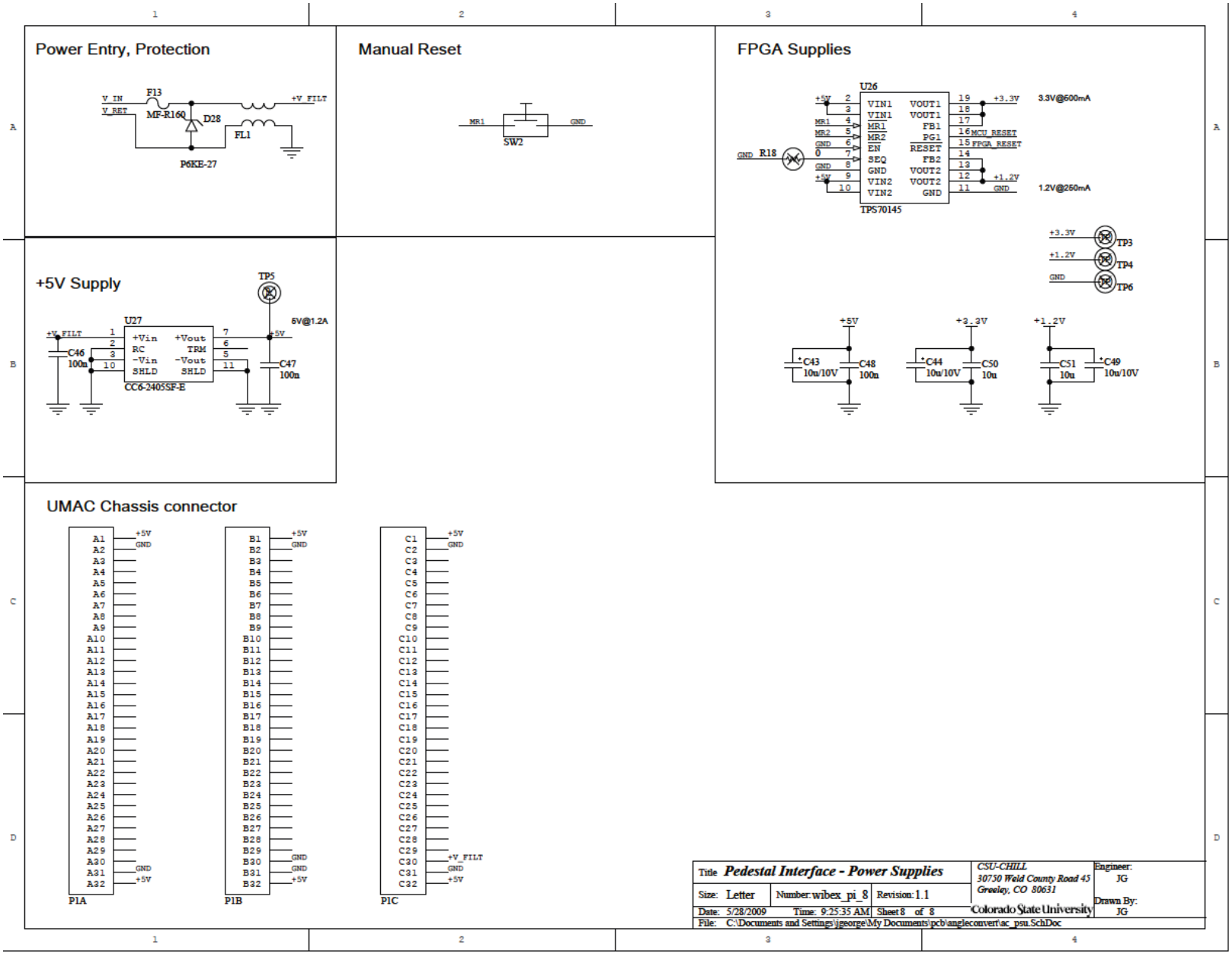
Power Entry, Protection
V_IN
V_RET
F13
MF-R160
D28
P6KE-27
FL1
+V_FILT
Manual Reset
MR1
GND
SW2
FPGA Supplies
U26
VIN1
VIN1
MR1
MR2
EN
SEQ
GND
VIN2
VIN2
VOUT1
VOUT1
FB1
PG1
RESET
FB2
VOUT2
VOUT2
GND
TPS70145
+3.3V
+1.2V
MCU_RESET
FPGA_RESET
3.3V@600mA
1.2V@250mA
R18
TP3
TP4
TP6
C43
10u/10V
C48
100n
C44
10u/10V
C50
10u
C51
10u
C49
10u/10V
+5V Supply
TP5
U27
+Vin
RC
-Vin
SHLD
+Vout
TRM
-Vout
SHLD
CC6-2405SF-E
C46
100n
C47
100n
5V@1.2A
UMAC Chassis connector
P1A
P1B
P1C
Title Pedestal Interface - Power Supplies
Size: Letter
Number: wibex_pi_8
Revision: 1.1
Date: 5/28/2009
Time: 9:25:35 AM
Sheet 8 of 8
File: C:\Documents and Settings\jgeorge\My Documents\pcb\angleconvert\ac_psu.SchDoc
CSU-CHILL
30750 Weld County Road 45
Greeley, CO 80631
Colorado State University
Engineer: JG
Drawn By: JG

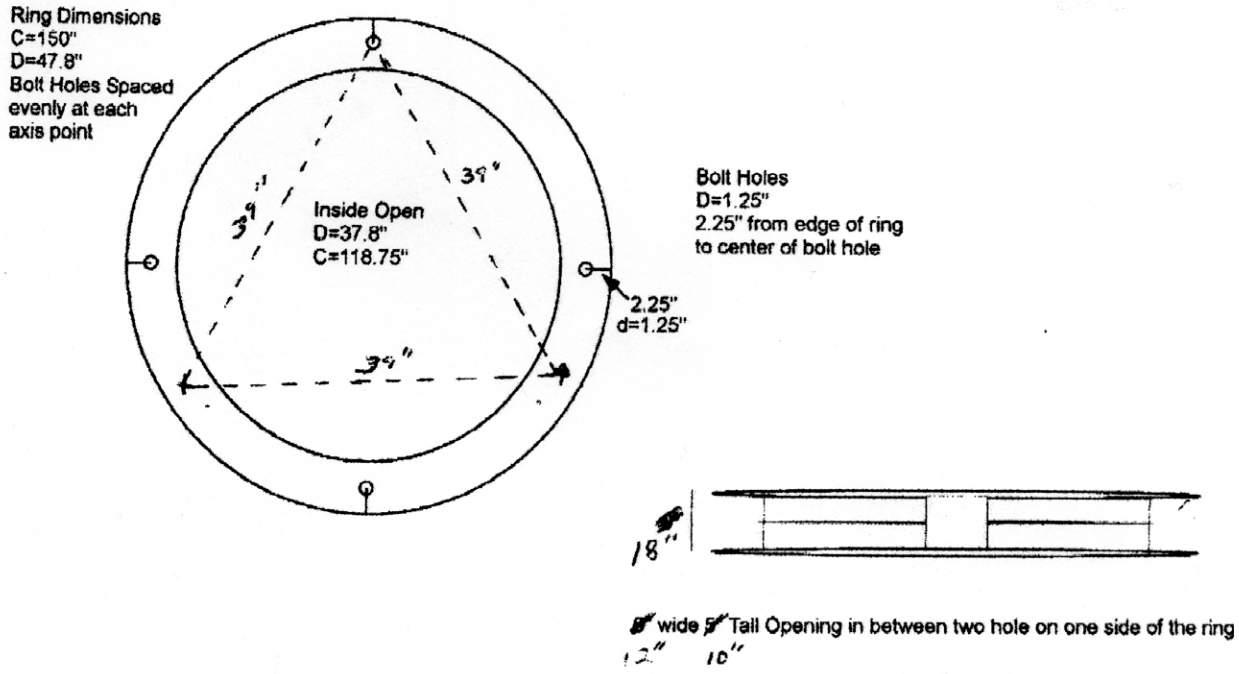

Figure A.1: SCR-584 Pedestal Riser Dimensions

SLIP RING WIRING LIST FOR BARCELONA X-BAND DUAL-POLARIZATION RADAR (Rev. 3) SEPT. 14, 2009										
	M23-12	**WIRE**	**Signal**	**Pedestal Upper Terminal**		**Slip Ring**		**Pedestal Base Terminal**		**TERMINATION**
EL ENCODER	8	BLU/WHT	power Supply		TB7-1	SR-3		TB3-1	BLU/WHT	CP1-1
	1	WHT/BLU	ground		TB7-2	SR-1		TB3-2	WHT/BLU	CP1-2
	2	GRN/WHT	Data+		TB7-3	SR-35		TB3-3	GRN/WHT	CP1-3
	9	BRN/WHT	Set Zero		TB7-8	SR-27		TB3-8	BRN/WHT	CP1-4
	3	ORN/WHT	Clock+		TB7-6	SR-17		TB3-6	ORN/WHT	CP1-5
	10	WHT/GRN	Data-		TB7-4	SR-37		TB3-4	WHT/GRN	CP1-6
	5	WHT/BRN	CW/CCW		TB7-5	SR-21		TB3-5	WHT/BRN	CP1-7
	11	WHT/ORN	Clock-		TB7-7	SR-19		TB3-7	WHT/ORN	CP1-8
	SHLD	SHLD	Shield		TB7-9	SR-10		TB3-9	SHLD	N/C
SPARES					TB7-10	SR-33		TB3-10		
					TB7-11	SR-29		TB3-11		
					TB7-12	SR-25		TB3-12		
EL FEEDBACK	**M23-17**	**WIRE**	**SIGNAL**						**WIRE**	**HD-22 (15)**
	14	RED/BLU	EL Ref out +		TB10-1	SR-4		TB6-1	RED/BLU	4
	17	GRY/PNK	EL Ref out -		TB10-2	SR-5		TB6-2	GRY/PNK	5
	2	YLW/BRN	El sin+		TB10-3	S4-6		TB6-3	YLW/BRN	6
	1	WHT/YLW	El sin-		TB10-4	SR-7		TB6-4	WHT/YLW	7
	11	BRN	El cos +		TB10-5	SR-40		TB6-5	BRN	8
	12	WHT	El cos -		TB10-6	SR-39		TB6-6	WHT	9
	13	PNK	El +5V out		TB10-7	SR-38		TB6-7	PNK	13
	9	GRY	EL PAI-3		TB10-8	SR-36		TB6-8	GRY	14
	SHLD	SHLD	SHLD		TB10-9	SR-20		TB6-9	SHLD	SHLD TO SHELL
STOW & RUN/SAFE SWITCHES			EL STOW SW		TB10-10	SR-22		TB6-10		
			EL STOW SW		TB10-11	SR-24		TB6-11		
			EL STOW SW		TB10-12	SR-26		TB6-12		
			RUN/SAFE AZ SSW					TB6-13		
			RUN/SAFE AZ SSW					TB6-14		
EL MOTOR	**M23-6**	**WIRE**	**SIGNAL**						**WIRE**	**PAGODA TB**
	1	1	PHASE A		TB8-2	SR-48		TB4-2	1	TB6-7
	2	2	PHASE B		TB8-3	SR-46		TB4-3	2	TB6-9
	6	3	PHASE C		TB8-4	SR-45		TB4-4	3	TB6-8
	3	GRN/YLW	GROUND		TB8-1	SR-47		TB4-1	GRN/YLW	GROUND
	4	BR1	BRAKE +		TB8-11	SR-14		TB4-11	BR1	TB6-3
	5	BR2	BRAKE -		TB8-12	SR-12		TB4-12	BR2	TB6-4
	SHLD	SHLD	SHIELD		TB8-5	SR-44		TB4-5	SHLD	GROUND
TX/RX 120V			Line		TB8-6	SR-28		TB4-6		
			Neutral		TB8-7	SR-30		TB4-7		
			Ground		TB8-8	SR-32		TB4-8		
SPARES					TB8-9	SR-18		TB4-9		
					TB8-10	SR-16		TB4-10		
					TB9-1	SR-8		TB5-1		
					TB9-2	SR-9		TB5-2		
					TB9-3	SR-11		TB5-3		
					TB9-4	SR-13		TB5-4		
					TB9-5	SR-15		TB5-5		
					TB9-6	SR-2		TB5-6		
					TB9-7	SR-34		TB5-7		
					TB9-8	SR-31		TB5-8		
					TB9-9	SR-23		TB5-9		
			EL LIMIT SW COMMON		TB9-10	SR-43		TB5-10		
			EL LOWER LIMIT SWITCH -NC		TB9-11	SR-42		TB5-11		
			EL UPPER LIMIT SWITCH -NC		TB9-12	SR-41		TB5-12		

BARCELONA X-BAND SERVO AMP FIXTURE WIRE LIST			
Servo Amp TERMINAL #	SIGNAL	Wire	Comment
TB-1-1	+24V DC In		
TB-1-2	+24V DC In		
TB-1-3	+24V DC In		
TB-1-4	+24V DC Return		
TB-1-5	+24V DC Return		
TB-1-6	+24V DC Return		
TB-2-1	N/C		
TB-2-2	N/C		
TB-2-3	N/C		
TB-2-4	N/C		
TB-2-5	N/C		
TB-2-6	N/C		
TB-3-1	L1, Servo Amp Power		
TB-3-2	L1, Servo Amp Power		
TB-3-3	L2, Servo Amp Power		
TB-3-4	L2, Servo Amp Power		
TB-3-5	L2, Servo Amp Power		
TB-3-6	L2, Servo Amp Power		
TB-4-1	AZ Analog In +		
TB-4-2	AZ Analog In -		
TB-4-3	AZ Brake +		AZ Motor Brake + (BR 1)
TB-4-4	AZ Brake -		AZ Motor Brake + (BR 2)
TB-4-5	AZ Drive, Analog Out +		
TB-4-6	AZ Drive, Analog Out -		
TB-4-7	AZ Motor Power C	16 AWG wire	AZ Motor Phase A
TB-4-8	AZ Motor Power B	16 AWG wire	AZ Motor Phase C
TB-4-9	AZ Motor Power A	16 AWG wire	AZ Motor Phase B
TB-4-10	Relay 1, Normally Open		
TB-4-11	Relay 1, Common		
TB-4-12	Relay 1, Normally Closed		
TB-5-1	Opto 1+		Upper Limit switch
TB-5-2	Opto 1-		jumper to 24Vdc Return
TB-5-3	Opto 2+		Lower Limit Switch
TB-5-4	Opto 2-		jumper to 24Vdc Return
TB-5-5	Opto 3+		Run/Safe & AZ Stow
TB-5-6	Opto 3-		jumper to 24Vdc Return
TB-5-7	Opto 4+		Not Connected
TB-5-8	Opto 4-		jumper to 24Vdc Return
TB-5-9	24Vdc Return	22 AWG wire	jumper to Opto (x)-
TB-5-10	+24V DC In	22 AWG wire	24Vdc for Opto + signals
TB-5-11	+24V DC In	jumpered 24Vdc	via limit switches & run/safe
TB-5-12	+24V DC In	jumpered 24Vdc	switch
TB-6-1	EL Analog In +		
TB-6-2	EL Analog In -		
TB-6-3	EL Brake +		EL Motor Brake + (BR 1)
TB-6-4	EL Brake -		EL Motor Brake + (BR 2)
TB-6-5	EL Drive, Analog Out +		
TB-6-6	EL Drive, Analog Out -		
TB-6-7	EL Motor Power C	16 AWG wire	EL Motor Phase A
TB-6-8	EL Motor Power B	16 AWG wire	EL Motor Phase C
TB-6-9	EL Motor Power A	16 AWG wire	EL Motor Phase B
TB-6-10	Relay 2, Normally Open		
TB-6-11	Relay 2, Common		
TB-6-12	Relay 2, Normally Closed		

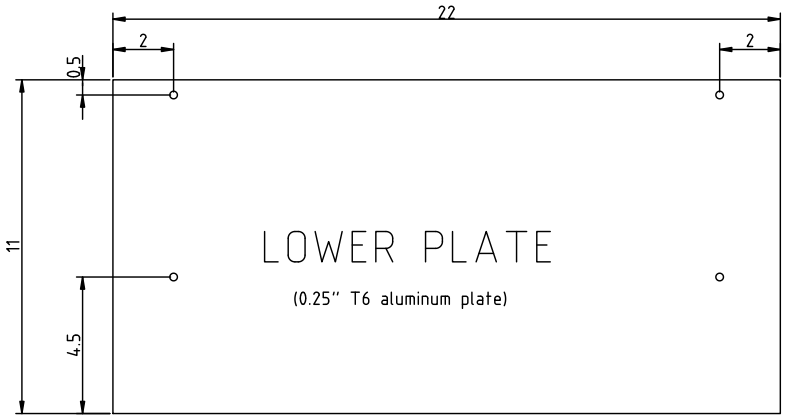
22
2
2
0.5
11
4.5
LOWER PLATE
(0.25" T6 aluminum plate)

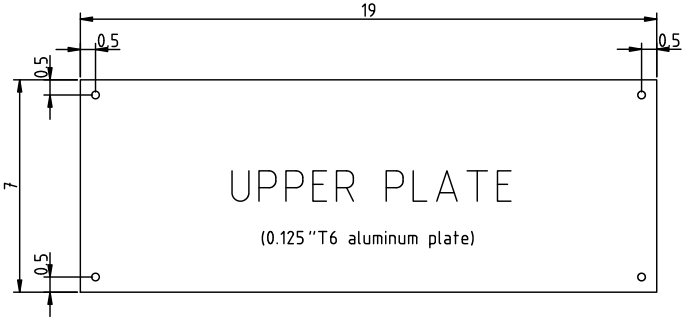
19
0.5
0.5
0.5
0.5
7
UPPER PLATE
(0.125"T6 aluminum plate)